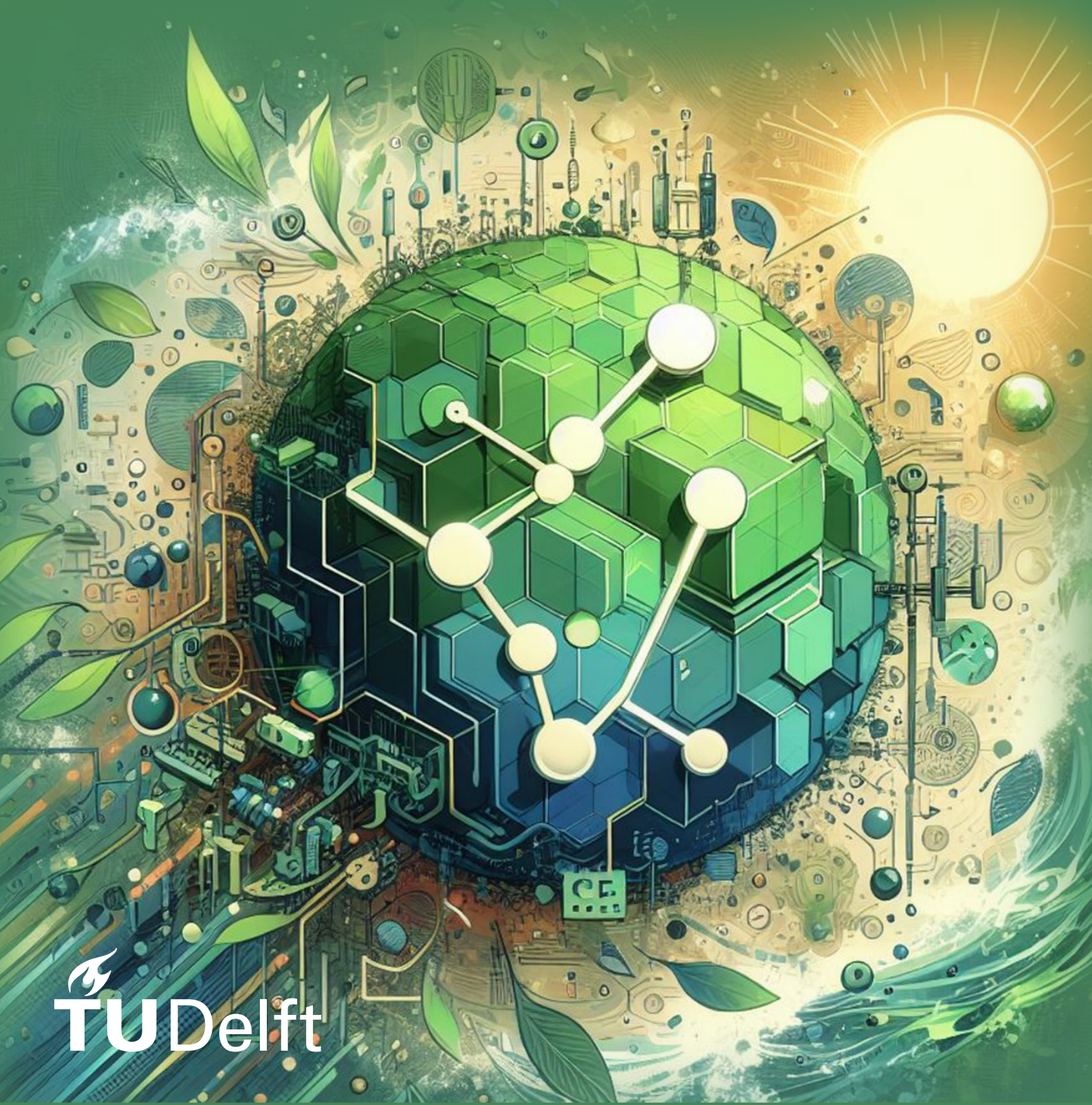


Ab initio and machine learning studies of solid electrolyte Li_3InCl_6 disorder and high entropy effects

Rita Villar Parajó
MSc Applied Physics - Master Thesis



Ab initio and machine learning studies of solid electrolyte Li_3InCl_6 disorder and high entropy effects

by

Rita Villar Parajó

to obtain the degree of Master of Science

at the Delft University of Technology,

to be defended publicly on Monday June 17th, 2024 at 14:30 h.

Student number: 5501148

Project duration: September 18th, 2023 – May 31st, 2024

Thesis committee: Prof. dr. ir. M. Wagemaker, TU Delft, supervisor

Dr. A. Vasileiadis, TU Delft, daily supervisor

Dr. A. K. Lavrinenko, TU Delft, daily supervisor

Dr. M. Rana, TU Delft

This thesis is confidential and cannot be made public until December 17th, 2024.

Cover: Image generated with the assistance of AI (modified)

Style: TU Delft Report Style, with modifications by Daan Zwaneveld

An electronic version of this thesis will be made available at <http://repository.tudelft.nl/>.

Abstract

As is already known, large- and medium-scale energy storage solutions are required for the much needed energy transition. Batteries become their most relevant in this circumstance, and specifically solid state batteries may have the key to solve the biggest drawbacks of current battery technologies. At their best, they offer safety and lightness while increasing storage capacity. Nonetheless, there are still hurdles to overcome, namely the complex ion kinetics in solids. Herein we present a computational study of the diffusion properties of Li_3InCl_6 , a member of the emerging family of halide-based solid electrolytes. We also investigate two prominent approaches to enhancing ionic conductivity: cation-site disorder and high entropy. Additionally, we embark on the machine learning venture for molecular dynamics with the implementation of machine learning trained potentials in our simulations.

Acknowledgements

Thanks to Alexandros for giving such an amazing lecture on computational research of battery materials that I am presenting this thesis one year later. To Anastasiia, for receiving most of my silly questions and guiding me out of them.

To everybody at the SEE group for sharing lunch and coffee breaks in the middle of my laptop-staring sessions. To Jouke for being so patient with me when I have tried to optimize my jobs beyond my possibilities.

To my friends and housemates for not getting angry when I have checked my simulations from my phone during dinner, and to my mother for trusting that I will do a good job but throwing in a prayer just for an extra push
To Christina for sustaining me.

Contents

Nomenclature	v
1 Introduction	1
1.1 The quest for advanced energy storage devices: solid-state batteries	1
1.2 Challenges in solid-state batteries and Li_3InCl_6 as a proposed solid electrolyte	2
1.3 Computational modeling for optimizing electrolyte materials	6
1.4 Goals of this work and outline	6
2 Theoretical Background	8
2.1 Principles of (solid-state) batteries	8
2.2 Principles of diffusion in solids	9
2.3 The crystal Li_3InCl_6	12
2.3.1 High entropy: origin and interest.	14
2.4 Density functional theory as an atomistic microscope	15
2.4.1 DFT in practice: structure optimization and molecular dynamics	16
2.5 Principles of molecular dynamics simulations	17
2.5.1 Study of conductivity from molecular dynamics simulations	19
2.6 Brief introduction to machine learning	21
2.6.1 Principles of machine learning	22
2.6.2 Principles of artificial neural networks.	25
2.6.3 Machine learning trained potentials.	27
3 Methods	29
3.1 Bringing disorder and high entropy to Li_3InCl_6	29
3.2 Computational specifications.	32
3.2.1 Fine tuning of a machine-learning trained potential	33
4 Results and discussion	35
4.1 Characterization of the diffusivity of Li_3InCl_6 and effects of disorder	35
4.1.1 Structure stability	36
4.1.2 Bulk diffusivity and activation energy	37
4.1.3 Dimensionality of diffusion	39
4.1.4 Effect of cationic-site disorder	41

4.2	Effects of high entropy: multicationic substitution	43
4.3	Implementing machine learning trained potentials for solid electrolyte analysis	46
4.3.1	To fine tune or not to fine tune	46
4.3.2	Reproducibility of ab initio results	48
4.3.3	Beyond the limits of ab initio	50
5	Conclusions	52
	References	54
A	Appendix: supporting information	64
B	Appendix: Python tools	68

Nomenclature

Listed in order of first appearance.

Term	Definition	Explanation
LIC	Li_3InCl_6	-
In layer	indium layer	Layer in Li_3InCl_6 along the c axis where In exclusively resides, comprised of sites 2b and 4g. Lithium atoms can also access this layer via 4g sites, but In is never found outside it.
Li layer	lithium layer	Layer in Li_3InCl_6 along the c axis only visited by Li ions, comprised of sites 2c and 4h.
ordered	ordered structure	Li_3InCl_6 structure where In exclusively sits at 2b sites in the indium layer.
disordered	disordered structure	Li_3InCl_6 structure where an indium atom per $2 \times 1 \times 2$ supercell (1/8 atoms) is displaced from site 2b to site 4g.
O	ordered structure	
ELC	even, low clustering	disordered structure where the In dislocation with low clustering of indium polyhedra and same number of In atoms in all layers (4).
EHC	even, high clustering	disordered structure where the In dislocation with higher clustering of indium polyhedra and same number of In atoms in all layers (4).
OHC	odd, high clustering	disordered structure where the In dislocation with higher clustering of indium polyhedra and different number of In atoms in every two layers (3 vs. 5).
OLC	odd, low clustering	disordered structure where the In dislocation with low clustering of indium polyhedra and different number of In atoms in every two layers (3/5).
within-layer	-	Hops in the crystal structure between two sites that belong to the same layer. Not to be confused with "In layer", referring to the indium layer.
cross-layer	-	Hops in the crystal structure between two sites that belong to different layers.

Term	Definition	Explanation
pristine	-	Li_3InCl_6 . Structure where the cationic lattice is composed only of In atoms.
HE	High entropy	Structure where the cationic lattice from the original Li_3InCl_6 is substituted by a mixture of several elements.
HE5	High entropy 5	Structure where the cationic lattice is composed of five elements: In, Sc, Yb, Zr and Lu
HE4	High entropy 4	Structure where the cationic lattice is composed of four elements: Sc, Yb, Zr and Lu
PT	Pretrained	The pretrained CHGNet MLTP before fine tuning, as trained by the 2022 Materials Project database
FT	Fine tuned	The in-house fine tuned CHGNet MLTP

1

Introduction

Energy has been the driver of human development since its dawn, from the Middle Paleolithic—marked by the *Homo erectus* harnessing fire—to the Neolithic Revolution—shaped by the advent of agriculture—all the way until the development of steam engine technologies in the Industrial Revolution^[1].

While the exploitation of energy seems to drive this timeline, its storage has always been crucial: for example, the very act of wearing clothes emerged in an effort to preserve our own energy and permitted the geographical expansion of the species. In a more contemporary fashion, the issue of energy storage was already a concern in 1917, when it was written that it had "long been recognized that [hu]mankind must, in the near future, be faced by a shortage of power unless some means were devised for storing power from the intermittent sources of nature."^[2] The extent to which that future was indeed near remains a subject of discussion, but it is unequivocally the present now. Perhaps we are facing the next stage in the energetic timeline of humanity.

1.1. The quest for advanced energy storage devices: solid-state batteries

The relentless accumulation of CO₂ in the atmosphere, coupled with the consequential global warming, is leading to drier ecosystems with escalating consequences. This includes an increase in water evaporation outpacing that of precipitation, and a surge of extreme weather events, for example^[3]. Oceans, responsible for about 70% of the total oxygen production, are susceptible to unexpected shifts from which ecosystems might not recover^[4]. The thawing of the no-longer-permanent permafrost, which houses more than twice as much carbon as the atmosphere, silently amplifies the issue and may entail more serious and unforeseeable consequences. Amidst these challenges, it is evident the current energy system, reliant anyway on finite resources, is unsustainable. Great efforts across all of society are striving for change.

However, this push towards decarbonization and the pursuit of sustainable energy sources often means the implementation of renewable energy sources such as solar or wind, which are intermittent and unreliable to a certain degree. Consequently, there arises a need for this energy to be stored. Studies throughout the past decade show that to power Europe with fully renewable energies, storage capacity must be at least 300 TWh. This is approximately equivalent to the batteries of 3 billion electric cars^[5, 6, 7, 8], almost 12-fold the number of passenger cars in the continent^[9]. The electrification of mobility is another key factor in the energy transition, as 23% of global emissions are produced by the transportation sector^[10]. Hence, also medium-scale, mobile energy storage devices are indispensable.

The demand for electrochemical energy storage for transportation, grid storage and residential power-backup applications emphasizes safety as a pivotal aspect of these technologies. In light of this, safety standards must now be acceptable for large, energy-dense components close to each other and humans^[11]. While traditional liquid lithium-ion batteries have significantly influenced energy storage and electronics since the 1990s, they grapple with limitations in energy density, safety, and sustainability^[12]. Therefore, ongoing research explores advanced energy storage solutions, primarily categorized into two branches: advanced Li-ion, focused on improving the properties of already established traditional Li-ion batteries, and post Li-ion. The latter reaches for improved devices that use different cations, metallic anodes, or solid electrolytes (SEs)^[13]. This will be the focus of the presented work.

Solid-state batteries (SSBs) represent an enticing alternative since they completely avoid the flammable (liquid) electrolytes from traditional Li-ion batteries and offer the potential for higher energy density. Their improved capacity would result from the realization of metallic anodes, if proven feasible, larger voltage windows^[12], the necessity of less packing, and the implementation of bipolar stacking setups. Furthermore, by substituting liquid electrolytes for their solid counterparts—more stable, rigid, and at no risk of freezing or boiling—SSBs are expected to have longer cycling lives, no bulk polarization and wider working temperature ranges, respectively, as well as better prospects for recyclability^[12, 13]. Yet, the realization of solid-state batteries hinges on discovering suitable solid electrolyte materials and a deeper understanding of how these materials behave at the atomic level and their interface behavior.

1.2. Challenges in solid-state batteries and Li_3InCl_6 as a proposed solid electrolyte

In the pursuit of realizing the potential benefits of solid-state batteries (SSBs) at a practical scale, inherent challenges arise owing to their solid nature. The transition to solid state introduces high ionic resistance, which hinders ion transport kinetics, and brittleness, which limits applications with high current and capacity. Thus, special care must be taken to prevent or minimize broken physical contact, increased resistivity, uneven current distribution and shortened cycle life^[12, 13]. Besides mechanical considerations, narrow electrochemical windows also significantly curtail storage capacity and reduce cycle life, as they cause degradation of the active materials of the cell. Chemical degradation of the materials is also possible during fabrication, since active materials are often highly sensitive to oxygen and moisture. Besides reducing the cycle life, this also complicates manufacturing, which is a challenge in itself: achieving cost-effective processes is vital to advance SSB technology. Finally, another key point for improvement is interfaces: uneven metal deposition, causing dendrite growth, has become a focus of investigation in SSBs, originally unexpected due to their rigidity^[13]. Interface stability is crucial since decomposition products are likely to increase resistance to ion transport,

enabling electronic conductivity, or threatening cycling stability^[11, 12, 13].

Solid-state electrolytes are generally divided into families depending on the nature of their anions. Until recently, two main electrolyte families were prevalent, namely oxide-based and sulfide-based. While oxide-based options offer favorable air stability and wide electrochemical windows, they are often limited to conductivities below 1 mS/cm^[14]. This value falls significantly behind the estimated 10 mS/cm necessary for the comparable performance of SEs and LEs (liquid electrolytes), and their stiffness and processability difficulty also remain significant drawbacks^[15]. On the other hand, sulfide-based SEs are attractive due to their ultra-high ionic conductivity and mechanical softness. Still, instability towards ambient air, oxide cathodes and external voltages, as well as the release of toxic H_2S when exposed to ambient atmosphere, renders them less favorable for market implementation. Their high cost and difficult integration with cathode components further contribute to these challenges. Below, Figure 1.1 serves as a visual summary of the average main properties of these two families and introduces a promising new contender, which will be the focus of this work: halide-based SEs.

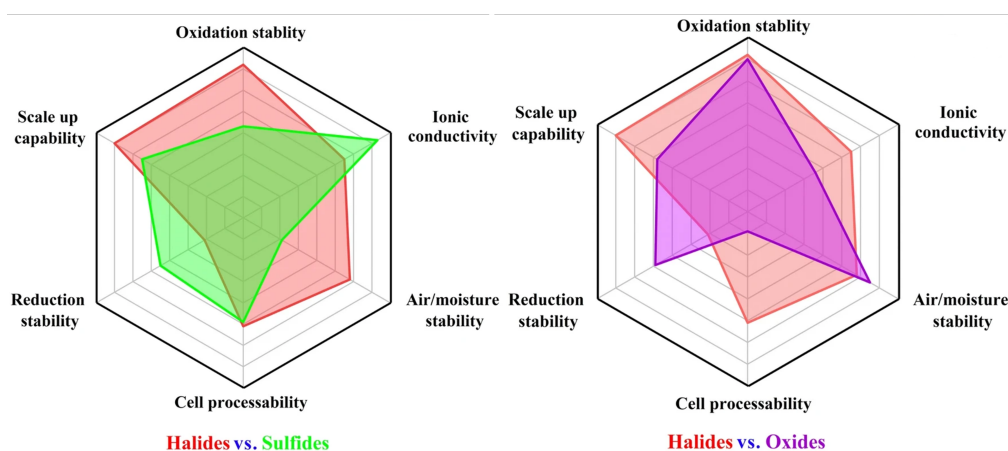


Figure 1.1: Comparison of the main families of SEs (sulfides and oxides) against upcoming halides. Adapted from ref. [16]. Licensed under CC by 4.0.

Halide electrolytes contain halogen atoms (F, Cl, Br, I or At) as their anions and have recently emerged as significant contenders in the realm of solid electrolytes. Despite their longstanding presence— LiAlCl_4 was first reported in 1923^[17] with applications in solid electrolytes dating back to the 1930s^[18]—, their unimpressive room-temperature conductivities ($\sim 10^{-7}\text{S/cm}$) hindered their application. It was not until 2018 when Asano *et al.* presented highly conductive and stable Li_3YBr_6 and Li_3YCl_6 ^[19] that the halide family gained relevance. Since then, many halide SEs with conductivity over 1 mS/cm at room temperature have been discovered, and broad research has been carried out to study enhancement techniques such as doping. Let Figure 1.2, collected in 2022, be testament to the recent surge in interest on halides.

It is now known that halides offer the potential for good ionic conductivities due to Li^+ interacting more weakly with the monovalent halide atoms than with divalent sulfur or oxygen anions^[19]. Moreover, they exhibit favorable mechanical softness, as well as high oxidation stability ($>4\text{V}$) and good chemical stability against many cathode materials in absence of protective coating^[14, 21, 22]. Strikingly good cyclability performance for SE standards can be observed from Figure 1.3 (left), where the halide SE Li_3YCl_6 shows remarkably stable capacity in the absence of protective coating, especially in contrast with the sulfide-based SE $\text{Li}_6\text{PS}_5\text{X}$ or typical liquid electrolytes. To the right, a similar study on Li_3InCl_6 from 2019^[23] again favors the halide SSE vs sulfide SSE in a cell against

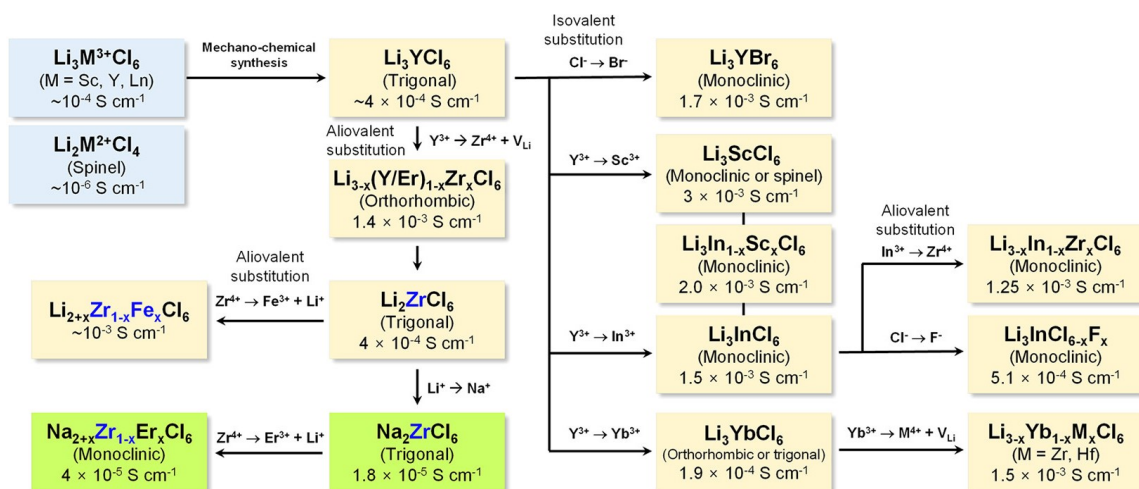


Figure 1.2: Map of halide SEs recently developed, where different geometries and enhancement techniques are explored. Reprinted with permission from reference [20] (Copyright 2022 American Chemical Society)

LCO. Another advantage from halide-based electrolytes is shown in Figure 1.4, where it can be seen that halides (fluorides and chlorides) are the only ones to reach the 4V line, where current cathode materials sit.

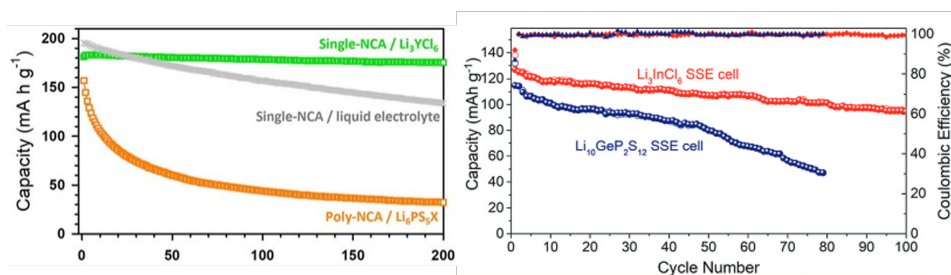


Figure 1.3: Outstanding stability of halide SSEs vs. sulfide SSEs is shown in these figures. **Left:** Li_3YCl_6 remains stable after 200 cycles while standard liquid electrolyte and argyrodite electrolyte counterparts lose capacity. Reprinted with permission from reference [20] (Copyright 2022 American Chemical Society), modified from original source [22] (Copyright 2021, Wiley-VCH). **Right:** Performance of Li_3InCl_6 SSE outperforming sulfide SSE. Reprinted with permission from ref. [23]. Copyright 2019 Royal Society of Chemistry.

However, halide SEs are not without shortcomings. They are still away from conquering the whole voltage window available, since they are unstable against metal Li anodes (one of the ambitions of SSBs) or common graphite or silica alternatives. Moreover, only a few of them present sufficiently high conductivities for applicability, and they are generally vulnerable to moisture and dry oxygen exposure^[14, 19]. The renovated interest in halides does not arise only from enhanced conductivities but also from reported air- and moisture-stable halides. Such is the case of the focus of this study, Li_3InCl_6 ^[23, 24].

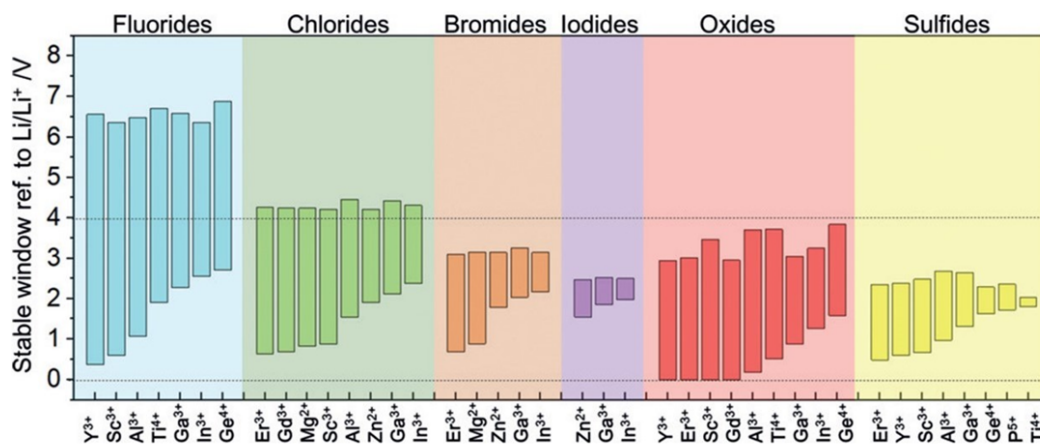


Figure 1.4: Overview of the chemical stability of different electrolyte families. Reproduced with permission from ref [25] Copyright 2019, Wiley-VCH

In the following work, Li_3InCl_6 (LIC) will be studied as a solid electrolyte candidate, as it has been recently reported by Li and colleagues to have especially favorable properties for the role^[23]. The material, as presented, solves many of the issues of halide-based electrolytes. Noteworthy as one of the few of halides with experimental conductivity surpassing 10^{-3} S/cm at room temperature^[12], LIC excellently withstands ambient conditions. After humidity exposure, Li *et al* showed that this superionic conductor can recover its original properties. Other reported attributes include thermal stability ($-25^\circ\text{C} - 75^\circ\text{C}$), good electronic insulation and electrochemical stability against high-voltage cathodes such as LiCoO_2 ^[23]. Moreover, specific synthesis techniques seem to passivize side reactions between the SE and the cathode in absence of interfacial treatment. Overall, these qualities make Li_3InCl_6 a species worth thorough investigation to take its kinetics further

Additional to research on specific materials, it is interesting to investigate how structural properties affect their performance in hopes to unlock a set of general favorable design principles. In particular, different synthesis methods have impacted the conductivity in halide materials giving rise to questions about how order/disorder in the ionic lattices might affect it^[19, 23, 26, 27, 28]. Similarly, high-entropy mixes have been shown to also improve conductivity and stability of electrolytes and electrodes by creating percolation pathways and showing larger tolerance to lattice distortions, for example^[29, 30, 31, 32, 33]. In this work, besides characterizing the diffusion properties of Li_3InCl_6 we will also explore if and how disorder and high entropy change its performance.

As a final remark, it is important to recognize that lithium and cobalt are broadly studied and accepted as essential to the technology of a low-carbon future. However, these materials and technologies do not materialize out of thin air, but instead emerge through human labor on natural resources. The extraction of these raw materials demands substantial water and energy quantities and often relies on precarious and vulnerable labor under unsafe conditions. Approximately one-third of the global lithium is sourced from Chile and Argentina, consuming vast amounts of water and discharging byproducts into the soil, potentially contaminating the groundwater of already severely arid regions. In China, battery-grade lithium production involves high-temperature processes that come with large energy requirements. Meanwhile, in Europe more sustainable processes are under study, prompting the question of why certain techniques are employed in certain places but deemed unacceptable in others. The case of cobalt, of which 70% is concentrated in the Democratic Republic of Congo, faces severe moral concerns, as child labor and unsafe working conditions are prevalent and

routinely denounced by Amnesty International and violent conflicts over cobalt availability are daily happenings. Environmental and human losses are invaluable all around. Having acknowledged these challenges, addressing the ethical implications behind our vision of the future becomes imperative.

1.3. Computational modeling for optimizing electrolyte materials

Understanding the mechanisms that allow the diffusivity of ions in solid-state battery materials is key for their design and the optimization of this technology^[14, 34]. To unlock the full potential of Li_3InCl_6 —through doping or introducing defects, for example—we must thoroughly comprehend its properties and mechanisms at the atomic level. Computational studies play a crucial role in achieving this. Ab initio molecular dynamics (AIMD) simulations serve as a microscopic lens, enabling precise examination of ion movement within the material and structural information, while also offering insight into the energetic and thermodynamic properties. Moreover, in simulation studies the systems are merely observed and do not suffer any inherent alterations through the process of measuring, as is a common limitation in experimental investigations^[35]. In fact, for this reason computational research can help the interpretation of experimental data. For a newly introduced candidate like LIC, computational studies can shed light on the best paths towards enhanced diffusivity.

Nonetheless, ab initio studies face challenges due to their computational-resources-intensive nature. As can be read in more detail in Section 2.4, the first-principles approach does not rely on empirical information; instead, it continually and iteratively solves fundamental quantum-mechanical equations, demanding significant computational power. Consequently, these simulations are limited to the sub-nanosecond scale and small samples, where only a few diffusion events can take place. Even simulating only at high temperatures (500K-1200K) and then extrapolating the results, as is the norm, resting on the assumption that the behavior of the material will not change too drastically, the statistical quality of the studies is often somewhat limited^[36].

In an effort to overcome these constraints, computational research on battery materials is heavily focusing on the development of machine-learning trained potentials (MLTPs) to implement in a classical setup^[37]. In the rapidly evolving landscape of materials science, the synergy between first-principles simulations and machine learning offers a promising avenue. Computational strain is significantly reduced, since computational costs in AIMD scale as $\mathcal{O}(\sim N_e^3)$, N_e being the number of electrons in the system, while classical simulations generally follow $\mathcal{O}(\sim n)$, having n symbolize the number of atoms^[38, 39]. At the same time, MLTPs create more reliable predictions of material properties than the fully classical alternative, having the potential to reach ab initio-level accuracy^[40]. By training the potentials on AIMD simulations, the objective is to capture the vast nature and complexity of the quantum interactions in crystals in a much computational- and assumption-affordable fashion, to allow simulations of much larger systems and during longer times.

1.4. Goals of this work and outline

By improving the transport the Li ions, not only will the desired kinetic performance be achieved, but structural issues, such as the formation of dendrites, can also be mitigated by minimizing hotspots, for example. By improving diffusivity, the traffic of ions will be swifter and no such hot areas will be created, or the rate at which they are formed will be significantly reduced. Therefore, even without

tackling the structural issue directly, the study of diffusion properties can contribute to the general performance and cyclability of SSBs.

At the same time, ameliorating the performance of the electrolyte could conceal poorer performance from cathodes. Perhaps outstanding kinetics in the electrolyte will enable the cells to afford more sluggish cathodes from more available sources^[41, 42].

On the other hand, the inclusion of machine learning in research methods has become of extreme interest over the past few years, justifiably^[43]. In the same way that theory is developed from empirical observation through human reasoning, refined algorithms can take it a step further in recognizing complex high-dimensional relationships that elude our abstract thinking abilities. Marrying the precision of AIMD and the efficiency of classical simulations, a new dimension of computational research of materials can be opened for the first time in the SEE group.

With all these considerations in mind, in this work we will try to shed light on three main questions: i) computational characterization of the kinetics of Li_3InCl_6 as a solid electrolyte, ii) effects of cationic-site disorder and high entropy on its diffusive properties, and iii) application of machine learning techniques for its investigation. For the realization of these tasks, computational tools were enhanced and developed along the way.

2

Theoretical Background

2.1. Principles of (solid-state) batteries

A battery is a device that stores and releases energy through electrochemical reactions during charge and discharge. Two simultaneous movements allow these processes to occur: electrons traverse an external circuit while the corresponding ionic charge moves internally through the electrolyte, as can be seen from the simplified diagram in Figure 2.1. The electrons and ions originate from the splitting of atoms at the electrodes, which engage in reduction/oxidation reactions at the cathode and anode respectively, creating a difference in potential. In such a redox reaction, the cathode undergoes reduction, gaining electrons, while the anode undergoes oxidation, losing them. This ensures the flow of current and allows the use of electrical energy to power our devices, like a light bulb in the example below.

For lithium batteries the discharge process is driven by the difference in lithium chemical potential in the electrodes. During discharge, the cathode (low lithium chemical potential) undergoes electrochemical reduction through the insertion of Li^+ ions coming from the electrolyte and electrons from the external circuit, to constitute complete Li atoms. Meanwhile, the anode (with high lithium potential) is oxidized, releasing Li^+ ions and electrons separately to the electrolyte and wire. The movement of the electrons generates an electrical current, which is the energy that can ultimately be retrieved from the system. In charging, the reverse process takes place by the application of external potential. Therefore, an effective electrolyte must deliver good ionic conductance and electronic insulation to minimize the risk of having the electrons move through the electrolyte instead of the external circuit, which would cause a short-circuit and would render no extractable energy^[34] from the battery.

This working principle is universal in batteries, whether with a solid or liquid electrolyte^[34]. The only difference in the process, besides the obvious change in the aggregation state of the electrolyte and therefore the different diffusion mechanisms, is that in liquid electrolyte batteries a porous membrane is set up to separate the electrodes and prevent a short circuit. A short would impede the whole

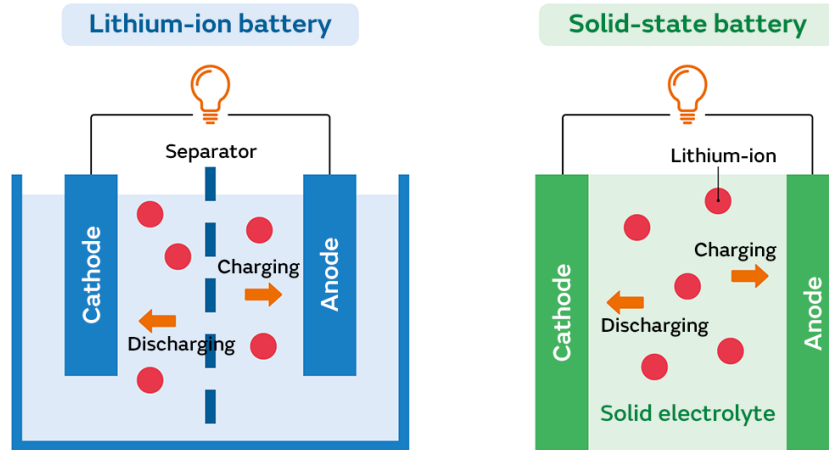


Figure 2.1: Diagram of a traditional Li-ion battery and a solid state battery (Murata Articles, 2022)

functioning of the system. In the case of all-solid-state batteries, the solid nature of the electrolyte itself should ensure no contact between the electrodes.

Whereas ion movement does not pose a big challenge in liquid electrolytes, solid diffusion is less straightforward. Solid electrolytes are typically crystalline structures with a specific short-range and long-range order, and for ions to disperse effectively they must access a limited number of sites that are free and energetically accessible. Briefly, favorable diffusion of ions in the solid electrolyte necessitates: a) free sites available, b) sufficiently low activation energies, and c) that the free sites create a continuous path to ensure macroscopic diffusion of the ions.

2.2. Principles of diffusion in solids

Diffusion comes from the Latin word "diffundere", which means "to spread out". Molecular diffusion is the thermal motion of all particles at temperatures over 0K. In gases, this movement is fast and particles move centimeters every second; for liquids, it is slower and only fractions of a millimeter are advanced per second. For solids, only distances in the range of nanometers to micrometers can be traveled in the same timescale. The free movement of diffusing species is restricted in solids and displacement happens in the form of "hops" between permitted spots. In the case at hand, that of crystalline solids, the lattice restricts the possible movements and allows their description in somewhat simpler terms.

In the pursuit of our goal to study the movement of Li ions in the different configurations possible for Li_3InCl_6 , and perhaps infer a way to improve it, we must stop to consider the mechanisms that allow this transport in the first place. In crystals, atoms hop from site to site in the lattice quite fast (timescale of 10^{-13}s) and then stay there for much longer times until the next jump. The energy toll required to perform these jumps is considerably larger than the average thermal energy $k_B T$, so the atoms cannot jump incessantly. Until the statistics align and the atoms obtain enough energy to jump, though, they do not stay put. Instead, they oscillate around their equilibrium positions causing lattice vibrations with Debye frequency $10^{-12} - 10^{-13}\text{Hz}$. When diffusing atoms do perform

a jump, their migration path happens between stable sites. An overview of diffusion mechanisms in solids can be seen in Figure 2.2 and a more detailed explanation of the most relevant cases for our study will follow Figure 2.3.

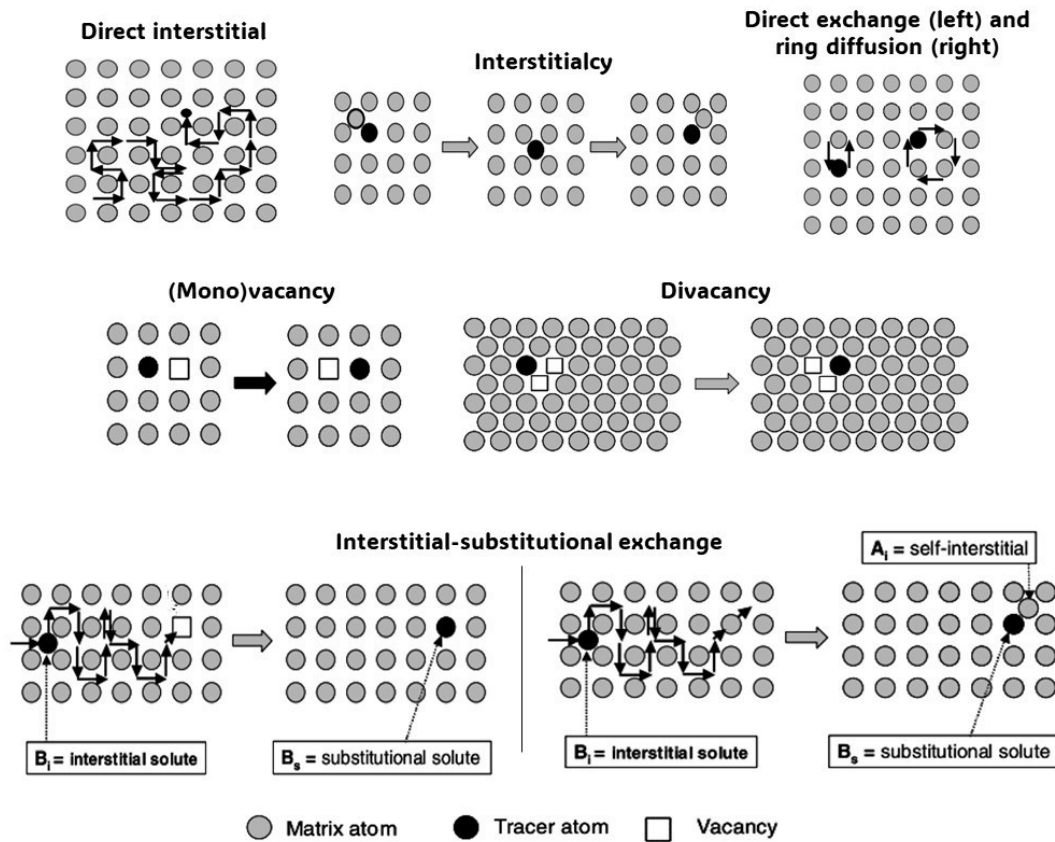


Figure 2.2: Overview of diffusion mechanisms in solids. A more detailed explanation of those relevant to cationic diffusion in crystals can be found following figure 2.3. Reprinted and modified with permission from ref. [44]. Copyright 2007 Springer Nature BV.

Let us proceed to briefly list and explain diffusion mechanisms in solids presented in the figure above. In solid solutions where solute atoms are smaller than solvent atoms, direct interstitial diffusion takes place as solute atoms occupy interstitial sites within the host matrix and move between these stable positions. This mechanism requires the displacement of neighboring matrix atoms, increasing energy requirements. Alternatively, indirect interstitial diffusion (interstitialcy mechanism) involves movement between interstitial and proper lattice sites, often found when atom sizes are comparable, and necessitates coordinated displacements. Temporary displacement of the lattice atoms is required for both of these mechanisms to create space for the displacement of the diffusing species. Direct exchange and ring diffusion also are part of the collective mechanisms, as they require more than one atom to move simultaneously. These require large lattice distortions, making them less relevant due to high energy demands.

On the other hand, vacancy mechanisms dominate the diffusion of both matrix atoms and substitutional solutes. Atoms from the lattice jump into neighboring vacancies, in a sort of direct exchange with the vacancy itself, creating no distortion. There can exist cases of bound groups of vacancies that disperse together, such as divacancies or the less likely trivacancies, that work similarly to the monovacancy case. Finally, complex combinations of diffusion mechanisms are also possible, such

as interstitial-substitutional exchange. In the following, the focus will be on mechanisms especially relevant for the cationic diffusion in ionic crystals, as shown in Figure 2.3.

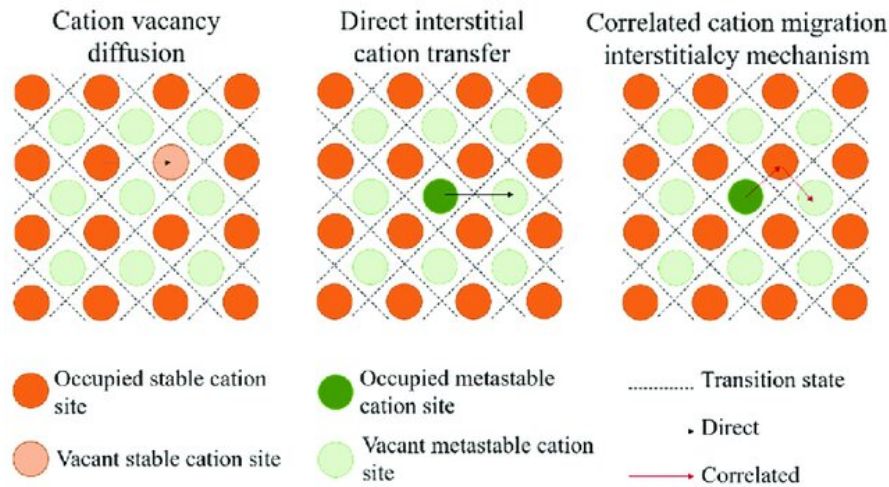


Figure 2.3: Schematic representation of the diffusion mechanisms of ions in solids . Reprinted with permission from ref. [13]. Copyright 2019, Springer Nature Limited.

In solid electrolytes, the cation can occupy energetically stable (shaded orange in Figure 2.3) or metastable positions (shaded green). If the cations move directly from a stable lattice site to an empty stable lattice site, cationic vacancy diffusion happens. If the same direct movement occurs but between metastable positions, then it is interstitial cation transfer. Alternatively, a correlated motion can take place: a cation in a metastable site moves into a stable site as another cation leaves that same stable site for another metastable position, and the first one takes its place. This is referred to as correlated interstitialcy mechanism^[13].

Whichever the case, the atoms will always move from a (meta)stable position to another (meta)stable position passing through unstable states. There will be an intermediate state that has the highest lattice strains and overall energy requirements. That point in the trajectory is named saddle point (refer to Figure 2.4) and gives the measure of the energy required of the atom to perform the jump (E_m). It is commonly said that the atoms move in an energy landscape that represents the energy barrier necessary to overcome.

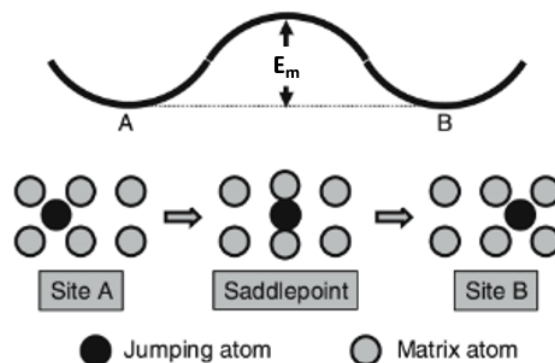


Figure 2.4: Simplified representation of an energy landscape. Reprinted with permission from ref. `Mdiffusion_solids`. Copyright 2007 Springer Nature BV

Lastly, it is important to consider that ion diffusion in the bulk is a multi-scale process governed by mechanisms natural to different length scales. All of them will collectively determine the final impedance of the material and overall device. At the atom scale, ion-lattice and ion-ion interactions occur. Microscopically, important phenomena such as grain boundaries might intervene in the movement of ions, and macroscopically the formation of interfaces between electrolyte and electrode (SEIs) must be considered, as they tend to hinder conductivity. To comprehensively and concurrently investigate ionic diffusion at all scales in batteries, advanced computational techniques that allow larger and longer simulations of more complex systems are indispensable. The integration of such techniques is also an objective of this work.

2.3. The crystal Li_3InCl_6

Understanding the structure of our material is a crucial point for our concern, the study of how lithium moves through it. Li_3InCl_6 crystallizes in the monoclinic structure ($\alpha = 90^\circ$, $\beta \neq 90^\circ$, $\gamma = 90^\circ$) with the $C2/m$ space group, as extensively reported from experimental studies^[23, 27, 45, 46]. It exhibits a distorted rock-salt lattice reminiscent of LiCl , where Li and In ions occupy interstitial sites in the anion sublattice. This sublattice, composed of chlorine anions Cl^- , adopts a ccp (cubic close-packed) lattice configuration.

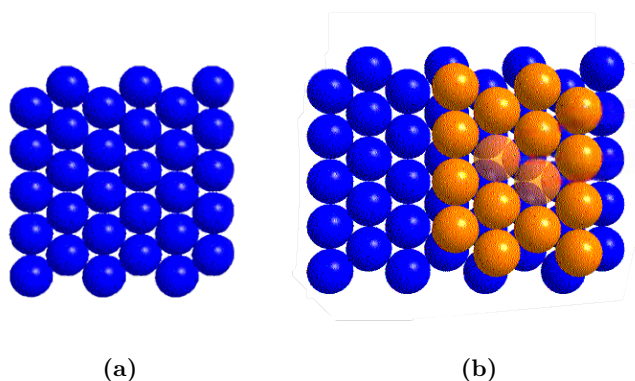


Figure 2.5: Construction of a ccp lattice. **a)** A single layer where the empty space between the atoms can be clearly seen. **b)** A second layer signaled in orange is added to build the bulk. Tetrahedral interstitial sites (shown under the semi-transparent orange atoms) and octahedral interstitial sites (spaces peaking through both layers) are formed.

The ccp lattice, represented in Figure 2.5, gives rise to octahedral and tetrahedral interstitial sites. Tetrahedral interstitials are formed in the spaces between atoms that belong to the same layer and which are then covered by the adjacent layers in the ccp arrangement, as can be seen in Figure 2.5 under each orange ball. This interstitial site is 4-coordinate, meaning that it is coordinated with four atoms in the lattice, while the alignment of empty spaces in consecutive layers creates octahedral interstitials, coordinated with six atoms. For the rock-salt crystal LiCl , all interstitials would be occupied with lithium. By introducing also indium, a reorganization of the cations takes place.

An imbalance is inherent to Li_3InCl_6 due to the insertion of indium in the LiCl structure. The cations, namely Li^+ and In^{3+} , have different charges, and to respect the principle of charge conservation only one In^{3+} is needed per every three Li^+ . Therefore, each trivalent indium ion (In^{3+}) introduced creates two cation vacancies, interstitials that would otherwise be filled with Li^+ but remain empty instead,

giving a 3-1-2 Li-to-In-to-vacancy ratio. These intrinsic vacancies create the opportunity for ionic diffusion in LIC, hence the Li partial occupancies shown in Figure 2.6.

Indeed, experimental studies report partial occupancies of indium^[46] in mechanochemically synthesized samples (0.89 in 2b and 0.05 in 4g). This creates a certain disorder in the arrangement of the indium cations, and therefore in the paths available to lithium too. These proportions mean that approximately one in every eight indium atoms are "displaced" from the 2b position into 4g. Therefore, a multiple of eight atoms of indium is needed to represent this distribution, which corresponds to four unit cells. In this project we study the four possible indium configurations which arise from the combination of indium positions 4g and 2b in the $2 \times 1 \times 2$ supercell. Further details can be found in the Methods Section 3.1.

Interestingly, this type of disorder has been reported to improve the conductive properties of some halide SEs by distorting the lattice and broadening the energy ranges of sites, favoring ionic transport^[18, 28, 47]. A focus of this work will be to study the effects, if any, of this disorder in the lithium diffusion properties.

Regardless, the cationic structure of LIC is layered along the c axis (Figure 2.6 left). In the 001 plane, the filled Wyckoff positions 2b and 4g can be found, whereas 2c and 4h are present in the 002 plane. Because In is confined to the sites 2b and 4g, we will call layer 001 "In layer", and the "Li layer" will be that corresponding to 002, where only Li can be. Nonetheless, it is noteworthy that lithium ions may also occupy the 4g position in the so-called "In layer".

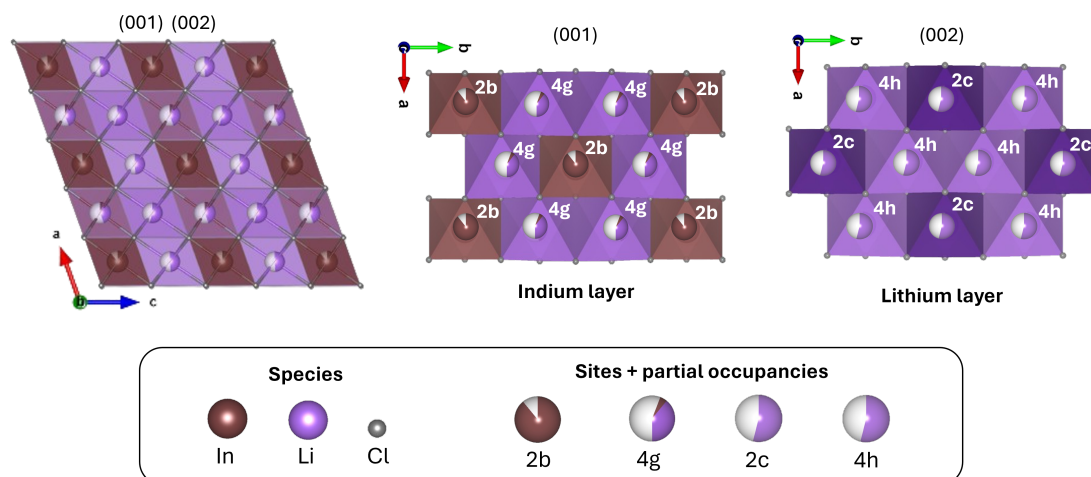


Figure 2.6: **Left:** Layered structure of two stacked Li_3InCl_6 unit cells along the c axis. In and Li sites are mostly octahedral positions but for the one tetrahedral position in the Li layer. Within each layer (**center, right**), a honeycomb-like structure can be observed where 6 sites with multiplicity 4 (4g and 4h) enclose one 2b or 2c site, respectively.

Between the layers there are also tetrahedral sites partially occupied by lithium (8j), as depicted in Figure 2.7. Whereas the octahedral sites are edge-sharing with each other, the tetrahedral site shares a face with all the Li octahedra, which makes for 3D connectivity of Li sites. Per the literature, the tetrahedral sites are expected to be mere transition states between the more stable octahedral spots^[19, 33, 46, 48]. If this is validated, for clarity of the analysis tetrahedral positions shall be disregarded in the coming investigation. Not registering the ions' visits to 8j enables the detection of cross-layer jumps without any loss of information.

Therefore, diffusion in LIC occurs via the vacancy mechanism, where the diffusion species "hops"

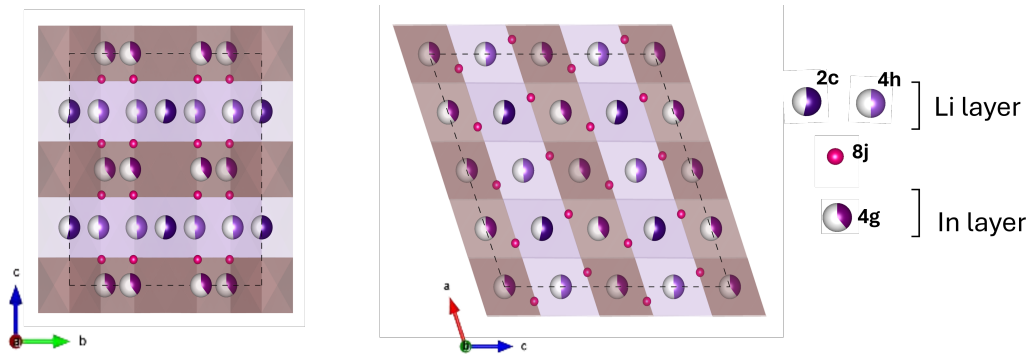


Figure 2.7: 2c, 4h and 4g lithium sites with partial occupancies and 8j tetrahedral sites (pink sites, not to scale and not showing partial occupancies). The tetrahedra sit between 4h and 4g sites creating a cross-layer path along the c axis.

between the empty sites created by the In substitution in LiCl. These hops or jumps can be classified into three categories: cross-layer jumps (when the cation moves from an In layer to a Li layer or vice versa, along the c-axis) and In or Li within-layer jumps, when the cation stays confined to the respective layer. Therefore, jumps 2b-2b, 4g-4g, 2b-4g and 4g-2b will be called "In layer jumps"; jumps 2c-2c, 4h-4h, 2c-4h and 4h-2c will be "Li layer jumps" and 2b-2c, 2c-2b, 4g-4h, 4h-4g, 4h-2b, 2b-4h, 4g-2c and 2c-4g will be "cross-layer jumps".

2.3.1. High entropy: origin and interest

A recent approach to enhancing diffusivity and also stability of SEs is high entropy^[49], previously popular in metallic alloys. High entropy ceramics are complex solid solutions characterized by the presence of multiple principal elements occupying specific lattice sites in near-equimolar ratios and causing high configurational entropy. The configurational entropy S_{config} is calculated via Equation 2.1, where R represents the gas constant, i indicates the species in the system and x_i is their molar concentration, assuming dispersed distribution of all species. Generally, this entropy should be above $1.5R$ as per Equation 2.1 for the multiply-substituted material to be considered high-entropy and more than five species should share a single site^[50, 51]. Likewise, the term medium entropy has been used to describe those structures with between two and four substituents and $R \leq S_{config} \leq 1.5R$ ^[33].

$$S_{config} = -R \sum_i x_i \ln(x_i) \quad 2.1$$

Since 2015, interest in high entropy mixes outside alloys proliferated due to reports of improved corrosion resistance and mechanical properties, introduced by lattice distortion^[29]. In the case of electrolytes, such distortion is suspected to broaden the energy ranges of the sites, resulting in overlapping energies that create a percolation path for the ions to move through^[30]. Moreover, in [33] they report 250% improved cyclability over 500 cycles owing to the anionic confinement as a result of lattice distortion. It must be noted that these effects are not expected to be the result of the presence of a specific element or even a specific combination, but rather an emerging property of the presence of multiple species^[49].

Alongside the five configurations of ordered/disordered Li_3InCl_6 , we will analyze the effects of entropy on the diffusion properties of the solid electrolyte by substituting In by In-Lu-Sc-Yb-Zr.

2.4. Density functional theory as an atomistic microscope

Li diffusion in the electrolyte is atomistic. Considering the size of the Li atom (145 pm, $\sim 10^{-10}\text{m}$ ^[52]) and its associated de Broglie wavelength (up to $\sim 10^{-9}\text{m}$), the wave-like behavior of the atoms is not negligible and quantum considerations become essential for an accurate description of Li^+ diffusion in electrolytes. The observation of the diffusion events is not accessible through experiments, and we just established that non-quantum computation methods are not fit to represent it. Hence, we rely on ab initio calculations constructed from the fundamental laws of physics for its study^[12]. Since the first-principles problem inherent to our crystalline problem cannot be solved analytically, we must resort to density functional theory (DFT) as the tool to solve it.

Starting from the beginning, the ground state of a system can be described by the time-independent, nonrelativistic Schrödinger equation^[53] (eq. 2.2). H stands for the Hamiltonian of the system and E represents the ground-state energy of the system. $\Psi = \Psi(\{\vec{r}_i, s_i, \vec{R}_j\})$ is the wavefunction containing the information of the whole system: electronic positions and spin (\vec{r}_i, s_i) and nuclei positions \vec{R}_j .

$$H\Psi = E\Psi \quad 2.2$$

Although this equation seems simple enough, its complexity escalates quickly when considering the terms of the Hamiltonian. H includes the kinetic energy of all the components and the interaction energy of nuclei with each other, nuclei with electrons, and electrons with each other. This is not trivial. Fortunately, others before us have done the heavy lifting and we can use their approximations and theorems to simplify the task. Considering the slow movement of the nuclei in reference to that of the electrons, due to their significantly larger mass (over 1,000 times bigger), nuclei can be considered static in their interaction, following the Born-Oppenheimer approximation^[53, 54]. Now the electron problem can be tackled on its own:

$$\left[\underbrace{\frac{\hbar^2}{2m} \sum_{i=1}^N \nabla_i^2}_{\text{kinetic energy}} + \underbrace{\sum_{i=1}^N V_l(\vec{r}_i)}_{\text{interaction with nuclei lattice}} + \underbrace{\sum_{i=1}^N \sum_{j<i} U(\vec{r}_i, \vec{r}_j)}_{\text{electron-electron interactions}} \right] \Psi = E_e \Psi; \quad \Psi = \Psi(\{\vec{r}_i, s_i\}) \quad 2.3$$

Here, \hbar represents Planck's constant, m is the mass of the electron and N is as usual the total number of particles (electrons) in the system. In this case, Ψ only depends on the degrees of freedom of the electrons (both position \vec{r}_i and spin s_i), and the energy E_e is also that of the electrons alone.

Continuing, making use of the Hohenberg-Kohn theorems^[55] it can be stated that the electron density (giving name to the name the *Density* Functional Theory) contains all the information of the electronic system, and that the density that minimizes the functional H is that of the ground state configuration. The electron density can be calculated as follows, accounting for spin multiplicity of electrons, 2_S :

$$n(\vec{r}) = 2_S \sum_i^N \psi_i^*(\vec{r}) \psi_i(\vec{r}) \quad 2.4$$

The electron density can be used to calculate the electron-electron interactions, namely in the Hartree and exchange-correlation potentials V_H and V_{xc} . Then, the electronic contributions can be decoupled

into the Kohn-Sham equations (Equation 2.5). Each electron is treated separately by including the classical electron-electron interaction into the Hartree potential V_H and the exchange-correlation potential V_{xc} , quantum-mechanical^[56]. V_{xc} encapsulates the complexities of the electron exchange and correlation effects within the quantum many-body system. The final set of Schrödinger-like equations follows:

$$\left[\frac{\hbar^2}{2m} \nabla^2 + V_l(\vec{r}) + V_H(\vec{r}) + V_{xc}(\vec{r}) \right] \psi_i(\vec{r}) = \varepsilon_i \psi_i(\vec{r}); \quad V_H(\vec{r}) = e^2 \int \frac{n(\vec{r}')}{|\vec{r} - \vec{r}'|} d^3r' \quad 2.5$$

It must be noted that all the electrons are no longer included in a wavefunction, but instead ψ_i represents the wavefunction of each of the individual electron. $\{\varepsilon_i\}$ represent fictional energies that do not relate to anything directly; instead, the energy of the system must be computed including some corrections.

The exact expression of the exchange-correlation potential is, nonetheless, unknown for the density functional expressions. Different approximate functionals are available, the choice of which can affect the accuracy of the DFT calculations. Different functionals such as LDA (local density approximation), GGA (generalized gradient approximation) or meta-GGA are tailored to address specific challenges for specific systems^[57].

Finally, this system is a self-consistent, iterative solution to the many-bodies problem proposed at the beginning of the section. An initial guess for the electronic density starts the iterations, from which $\psi_i(\vec{r})$ is solved for in Equation 2.5, and then used to calculate the new guess for $n(\vec{r})$ (Equation 2.4). When a certain convergence criterion is reached between consecutive iterations of the density, the loop will be stopped and a solution will have been obtained. The lowest-energy electronic configuration is known.

The DFT method can be used in conjunction with different algorithms to perform many calculations, such as optimization of structures or molecular dynamics simulations in our case.

2.4.1. DFT in practice: structure optimization and molecular dynamics

Structure optimization

The lowest-energy electronic configuration of a system, where the lowest-energy distribution of nuclei is achieved, can be obtained for any structure. Conveniently, the Hellmann-Feynman theorem^[58, 59] states that once the electronic configuration of the system is derived from the Schrödinger equation, all the forces between nuclei and electrons in the system can be derived from classical electromagnetic theory. This means that an easy calculation of Coulombic interactions will provide all the necessary information about the electronic-ionic interaction.

The process for structure optimizations is as follows: for a specific configuration of the ions of the system, the lowest energy electron density is obtained through the method described above. Then, all is left is the minimization of the classical forces acting on the nuclei. This is achieved by adjusting their positions until all the forces upon them vanish. Once again, we are presented with an iterative calculation where slight changes to the lattice are introduced until a convergence threshold is reached. The final result of such process will be the lowest-energy configuration of the provided structure. This process is also commonly known as (static) relaxation of the structure, geometry or volume.

It must be remarked that since the DFT relaxation is a strictly ground-state solver, only relaxations at 0K are obtained. Moreover, due to the sensitivity of the algorithm, convergence might not be reached if the structure is initialized too far from equilibrium or is caught in a metastable state, for example.

Ab initio molecular dynamics

Molecular dynamics (MDs) are studies of the evolution of systems at the molecular level based on the evaluation of the forces that act upon their components. The positions of the elements in the systems are updated according to these forces, prompting a new configuration and new interactions, resulting in new forces and a new update. Further explanation of molecular dynamics can be found in Section 2.5, while herein the role of DFT in molecular dynamics is briefly explained. DFT can be integrated into the MD routine to obtain quantum-mechanical-level accurate forces for the simulations. This is the definition of ab initio molecular dynamics, as they involve first principles calculations to obtain the forces in the system. This is performed analogously to the evaluation in forces for structure optimization.

These obtained forces are then integrated according to the classical equations of motion, giving the natural evolution of the positions of the ions while retaining quantum-mechanical accuracy. New positions trigger a new optimization of the electronic structure, similarly to the previous case. However, in molecular dynamics the subsequent configurations owe to the integration of the equations of motion, resulting in a causal correlation between them, contrary to structure optimizations where the updates are caused by an optimization algorithm to find the vanishing of the forces.

Also, importantly, in contrast with the previously explained DFT method of relaxation, AIMDs happen at finite temperature; otherwise, there would be no dynamics to be studied in the first place.

2.5. Principles of molecular dynamics simulations

Experimentally, values of physical quantities of many-body systems can be understood as an ensemble average, or put simply, as an average over all possible system configurations that are present in the bulk material. This is however impossible to achieve with computational methods, since considering all accessible states is too large of a task. The solution to this lies in statistical mechanics, as for ergodic systems proper statistical averages can provide the same information. Molecular dynamics simulations study the time evolution of many-body systems and provide (sufficiently) approximate statistical predictions about their properties.

From MD simulations, whichever their nature, the instantaneous particle coordinates and velocities are extracted and used to infer observables of interest. Naturally, these same observables are not obtained from experimental studies in the same way, and therefore care must be taken in equating results. In the case of experiments, each measurement is a sort of pre-averaged value over the number of particles that constitute the system and over the many configurations that took place throughout the measurement, for example. A comparable averaging is then required from simulations as well. The ergodic hypothesis is accepted in the following work, and hence the observables computed from time-averaged functions of the coordinates and momenta of a many-particle system are taken as equivalent to the ensemble-averaged quantities from experimental studies, under sufficiently long simulations^[54, 60].

Isolated systems can be studied under molecular dynamics using pair-additive forces. This way, by disregarding external forces such as gravitational pull for example, the force over particle i \vec{F}_i can be expressed as

$$\vec{F}_i(\vec{r}_i) = \sum_{j \neq i}^N F(\vec{r}_i - \vec{r}_j) \hat{r}_{ij} \quad 2.6$$

where j represents the rest of the particles in the system (or closest images created by periodic boundary conditions), \vec{r} is the position of a particle and \hat{r}_{ij} is the unit vector directed along $\vec{r}_i - \vec{r}_j$. From this equation, the equation of motion for particle i can only be Equation 2.7, where m_i represents the mass of particle i and t is the time variable.

$$\frac{d^2 \vec{r}_i(t)}{dt^2} = \frac{\vec{F}_i(\vec{r}_i)}{m_i} \quad 2.7$$

At this point, the key to the simulations resides in the choice of forces. They can only be approximated whether it is because the study is restricted to the classical realm of physics (classical molecular dynamics), or due to the impossibility of solving the quantum-mechanical problem (ab initio molecular dynamics) or even because of method limitations such as system sizes, inexact arithmetic or the imprecision of integration algorithms used to integrate the equation of motion.

Here, novel machine learning techniques pose a bridge without inherent compromises between ab initio accuracy and classical convenience. The potentials used in classical MDs are empirically modelled to represent the relevant interactions in different materials, while AIMDs numerically solve the most fundamental of equations possible. Machine learning trained potentials (MLTPs) have the ability to also model data from ab initio calculation but in much higher-dimensional and complex spaces than human minds can grasp, providing ab initio-level accurate results at a much lower computational cost^[40, 61].

Regardless of the method to calculate the forces, as indicated by Equation 2.7, they must be integrated to reveal the dynamics of the particles $\vec{r}_i(t)$. A widespread integration algorithm^[54], and the one that concerns us, is the Verlet algorithm that predicts the position \vec{r} of a particle with mass m at time $t + \Delta t$ with precision Δt^4 like:

$$\vec{r}(t + \Delta t) \approx 2\vec{r}(t) - \vec{r}(t - \Delta t) + \frac{\vec{F}(t)}{m} \Delta t^2 \quad 2.8$$

Some benefits of the Verlet algorithm are time reversibility and conservation of energy. The integration algorithm is routinely altered depending on the restrictions imposed on the dynamics of the system such as temperature or pressure limitations.

Ensembles: NVT and NPT

A final statistical concept is required: the aforementioned ensemble. An ensemble is a set of virtual copies of the system under study that serves as a bridge between the study of individual particles and the bulk properties of a system. This set includes all the possible system configurations under the restrictions imposed by keeping three thermodynamic state variables fixed. These might be the number of particles N , pressure p , temperature T , volume V , energy E , etc. Ensembles can ensure physical meaning from our simulations and help mimic relevant experimental conditions^[62, 63].

$$\langle K \rangle = \frac{3}{2} N k_B T \quad 2.9$$

$$\langle K \rangle = \frac{1}{2} \sum_i^N m_i v_i^2 \quad 2.10$$

For NVT, the number of particles, volume and temperature are kept constant. To this end, there are many algorithms available that control the temperature via the kinetic energy of the system, related according to Equation 2.9 and scaled by the Boltzmann constant k_B . Thus, the average kinetic energy must be kept constant to ensure constant T , which can be granted through the instantaneous velocities of all the particles in the system (v_i), as per Equation 2.10. Differences between the algorithms lie in how the velocities are adjusted.

To keep the temperature to the desired value, the Nosé-Hoover thermostat introduces an extra degree of freedom in the Hamiltonian of the system to account for the fictional heat bath the system is "submerged" in. It comes with associated kinetic and potential energy as well as mass (\mathcal{Q}), which will modify the equations of motion of the system (Equation 2.11). Therefore, the typical Verlet equations^[64] will be slightly modified to include ζ , the fictional friction from the bath. This friction is special considering that it not only slows particles down but might also accelerate them if the temperature needs to be increased (Equation 2.12).

$$m_i \frac{d^2 \vec{r}_i}{dt^2} = \vec{F}_i - \zeta(t) m_i \vec{v}_i \quad 2.11$$

$$\frac{d\zeta(t)}{dt} = \frac{1}{\mathcal{Q}} \left[\sum_i^N \frac{1}{2} m_i \vec{v}_i^2 - \frac{3N+1}{2} k_B T \right] \quad 2.12$$

The friction mass \mathcal{Q} dominates the relaxation of its dynamics and the second term inside the brackets is the updated expression of the average kinetic energy now that an extra degree of freedom has been introduced. In this way, the temperature of the simulated system is intrinsically regulated^[54].

On the other hand, keeping the volume constant is as easy as not moving the boundaries of the system and making them periodic. The particles are free to move and cross them, in which case it will reenter the simulation region from the opposite side. This not only maintains N constant but also allows to simulate a bulk material using a very reduced sample.

An analogous approach can be taken to maintain the pressure in the NPT ensemble, adopting then the Nosé-Hoover barostat. Barostats can also include random collisions between the particles to better portray the stochastic nature of materials, adding a gaussian random force with mean 0 to the equations of motion. Such is the case of the Langevin thermostat.

2.5.1. Study of conductivity from molecular dynamics simulations

From the molecular dynamics simulation, our aim is to study charge conduction in the electrolyte via the ions. The conductivity of a material (σ) only depends on the ability of its ions to move through

the electrolyte, regardless of the specific mechanism. This ability is strongly impacted by the available (thermal) energy of the system, as it will make it easier or harder to overcome energy barriers between sites. Therefore, this quantity can be described as an Arrhenius phenomenon (Equation 2.13) and the conductive properties of the system can be extrapolated from simulations at high temperature by applying this relation.

$$\sigma = \sigma_0 \frac{1}{T} e^{-E_a/k_B T} \quad 2.13$$

The pre-factor σ_0 encompasses ion charge and concentration, but also other elements such as migration entropy, jump distance, attempt frequency, and geometric information. A key aspect in our study, the activation energy E_a , governs the relation above. It includes both the energy needed to form mobile defects (creating vacant or interstitial sites in the crystal lattice), and the energy barrier that must be overcome for the defects to migrate. Unsurprisingly, T signals the operating temperature and k_B is the Boltzmann constant.

Another commonly discussed property of electrolytes is diffusivity (D). The Nernst-Einstein relationship in Equation 2.14 links the two of them, with N representing the total number of mobile ions, V the total volume of the system and q the associated charge. Therefore, an Arrhenius relation for D can also be deduced (Equation 2.15), in which D_0 represents the characteristic diffusivity of the material, quite analogous to σ_0 .

$$\sigma = \frac{Nq^2}{Vk_B T} D \quad 2.14$$

$$D = D_0 e^{-E_a/k_B T} \quad 2.15$$

Magnitudes such as conductivity and diffusivity can be extracted from atomistic simulations following the procedure described by de Klerk in reference [65]. From tracking the positions of each atom throughout the simulation, the diffusivity can be calculated for each temperature in two ways: from the mean squared displacement of the species (MSD, Equation 2.16), or from the jump rate (the rate at which the diffusing species moves in form of jumps, Equation 2.17).

$$D_{MSD} = \frac{1}{2dNt} \sum_{i=1}^N [r_i(t_0 + t) - r_i(t_0)]^2 \quad 2.16$$

$$D_J = \sum_j \frac{\Gamma_j a_j^2}{2d}; \quad \Gamma_j = J_j/Nt \quad 2.17$$

Equation 2.16, 2.17: In addition to the previously introduced quantities, d represents the diffusion dimensions and t represents the total time of the simulation. As is usual, $r_i(t)$ indicates the position of atom i at time t . In equation 2.17, Γ_j is the jump rate of a specific jump j , a_j is the distance of such jump, and J_j the number of jumps of that nature that occur throughout the simulation.

Both of these expressions have advantages and disadvantages. D_{MSD} is a straightforward calculation as it only uses information we directly obtain from the simulation without making any assumptions,

but it only provides insight into the bulk behavior of the material. On the other hand, more precise information about the diffusion mechanism and preferences is obtained through D_J when observing specific jumps or types of jump, restricting the summation over j . However, this jump study requires the definition of radii for the sites as a way to categorize in which position an atom is at each timestep. Therefore, an element of possible error is introduced.

A significant difference between both methods to extract D is back-and-forth jumping between two sites. By definition, its contribution to D_{MSD} will be null but not so for D_J . Therefore, an overestimation of the diffusivity can be expected from D_J . Notwithstanding this detail, jump- or type-specific D_J is valuable to compare with other jump diffusivities calculated in the same way to detect preferred directions of diffusion or diffusion blockages.

Due to the limitations of AIMD, namely the length of the simulations, good statistics are only feasible for high temperatures at which the diffusion events are more numerous. To extrapolate the activation energy and the diffusivity at working temperatures ($\sim 300K$), a linear fit can be drawn if Arrhenius behavior is assumed (Equation 2.15). The total activation energy can be extrapolated using D_{MSD} , or jump-specific activation energy from D_J datapoints. An in-between approach was taken in the following study. Category-specific diffusivities, which consider only a subgroup of all the possible jumps, were used to compare migration in different directions and domains of the material.

2.6. Brief introduction to machine learning

From Turing's question: "can machines think?" we find ourselves decades later wondering "can machines learn?". Just like him, we must concretize this question in order to solve it. Therefore: what is machine learning?

The term machine learning (ML) was introduced in 1959 at IBM when employee Arthur Samuel created a program that could play checkers. Previous to that, there had already been interest in studying and reproducing human cognitive processes dating back to 1949^[66], which laid the ground for what we now know as artificial neural networks. In 1951 the first neural network machine, the SNARC, was built^[67].

Not long after, the field started to leave behind the intention to model human cognition and to focus on potential applications. In the 1970s, the realization that technology was not developed sufficiently to achieve the expected level of artificial cognition prompted the so-called "AI winter", when little funding and attention was paid to the topic. Still, during this time algorithms different than the artificial neural networks were designed^[68], and the technical background for AI and ML slowly expanded.

In the next years, owing to the development of sophisticated fitting algorithms and the growth in data availability, machine learning gradually morphed into what we currently understand by the term^[69]. Surprisingly, the first ML software was commercialized for personal computers as early as 1989 to solve optimization problems such as resource allocation. Finally, in the decade of the 2010s machine learning became a cornerstone of many software services and in the last years the popularization of generative AI has brought machine learning to daily life in much of the world.

2.6.1. Principles of machine learning

The general machine learning problem is formally given by the definition^[43]:

“given a known set of information \mathbb{X} , called feature space and composed of many \mathbf{x} (feature or attribute vectors), predict or approximate the unknown function $f(\mathbb{X})$ ”

The goal in a machine learning problem is then to produce an approximate \hat{f} that reproduces f sufficiently well. Therefore, given enough data to accurately represent the dynamics of a system, the machine learning process will decipher the underlying connection between its attributes and resulting behavior. This allows it to precisely predict the outcomes of systems unknown to it. This property is called the *generalization* of the model.

From this basic definition stem many different categories of the machine learning problem. When the so-called set of labels $f(\mathbb{X}) = \{f(\mathbf{x})\}$ is known, then $(\mathbb{X}, f(\mathbb{X}))$ is called the training set and the problem is a *supervised learning problem*. The two main types of supervised learning are classification and regression, depending on whether the outcome is continuous (regression) or discrete (classification). In the opposite case, when the machine must find a pattern in the data without any reference results, then it is a problem of *unsupervised learning*. Clustering or density approximation (depending on the finitude of the output space) are the most common types among such problems. There exist other less widespread categories like semi-supervised (when only a few of the datapoints have a label) or reinforcement problems (when the model is trained to make decisions based on feedback). A summary of this categorization can be found in Figure 2.8, together with a graphical representation of some of the cases.

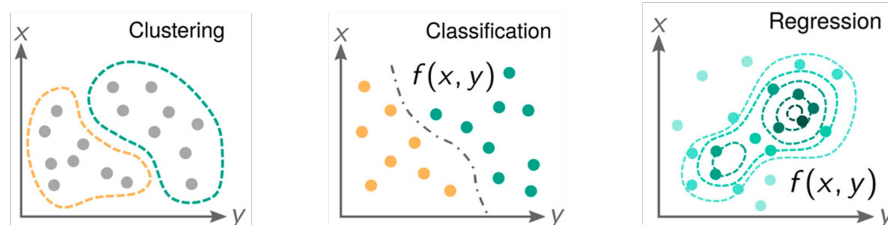
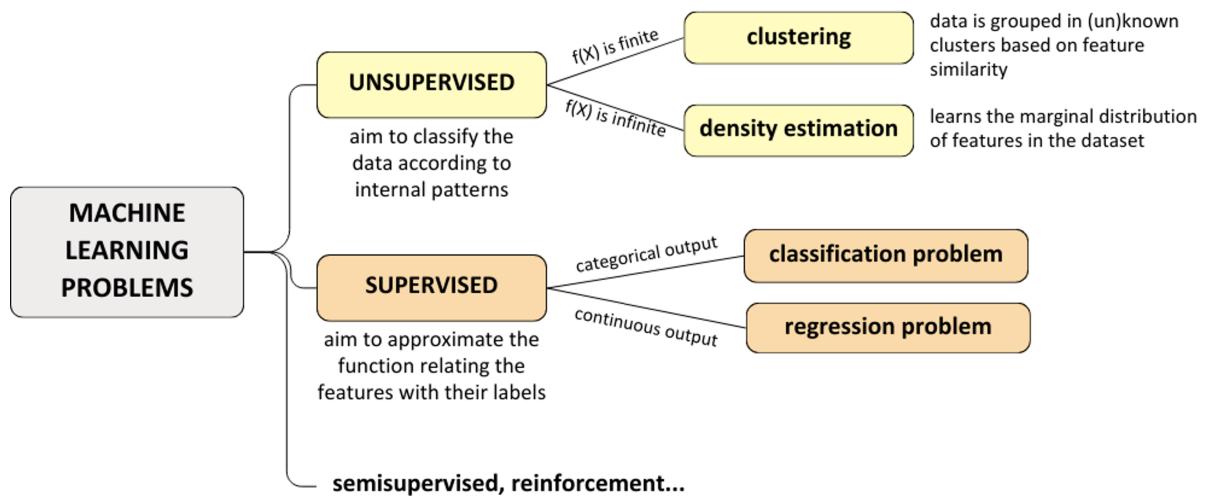


Figure 2.8: Visual summary of the most common machine learning problems and diagrams of clustering, classification and regression as representative examples of such problems.

Each of the aforementioned problems requires a particular strategy to solve it, naturally, leading to

a variety of algorithms. For instance, common approaches to unsupervised learning are k-means or hierarchical clustering algorithms, while linear regression, k-nearest neighbors or decision trees are well-established techniques for supervised problems. Detailed discussion of algorithms is beyond the scope of this report, as our focus are complex nonlinear regression problems. In this case, artificial neural networks (ANNs) and kernel-based methods dominate^[69], and only the former are used in this study. Further discussion of ANNs can be found in Section 2.6.2. For more extensive discussion of ML algorithms it is recommended to refer to [70], [71].

In the supervised regression problem, the output can either be the model itself \hat{f} or the set of predicted labels $\hat{\mathbf{y}} = \hat{f}(\mathbf{x}) = \theta^T \mathbf{x}$. As can be seen from the expression, the attributes obtained by the algorithm are a result of applying the transformation Θ^T to the feature vector \mathbf{x} . Θ represents the parameter vector, and it is the element that is optimized to produce the desired output. On the other hand, the feature vector \mathbf{x} is composed of the descriptors of the system.

The descriptors contain the properties of the system(s) under study that inform the training process. They must accurately represent the system in a physical way, and be systematic and computationally efficient. Descriptors ought to be a direct measure of how different two systems are from the mathematical point of view, and they can highlight or conceal the underlying mechanisms that the model must recognize. Hence, thorough understanding of the problem at hand is needed for their proper choice and ultimately the success of the model.

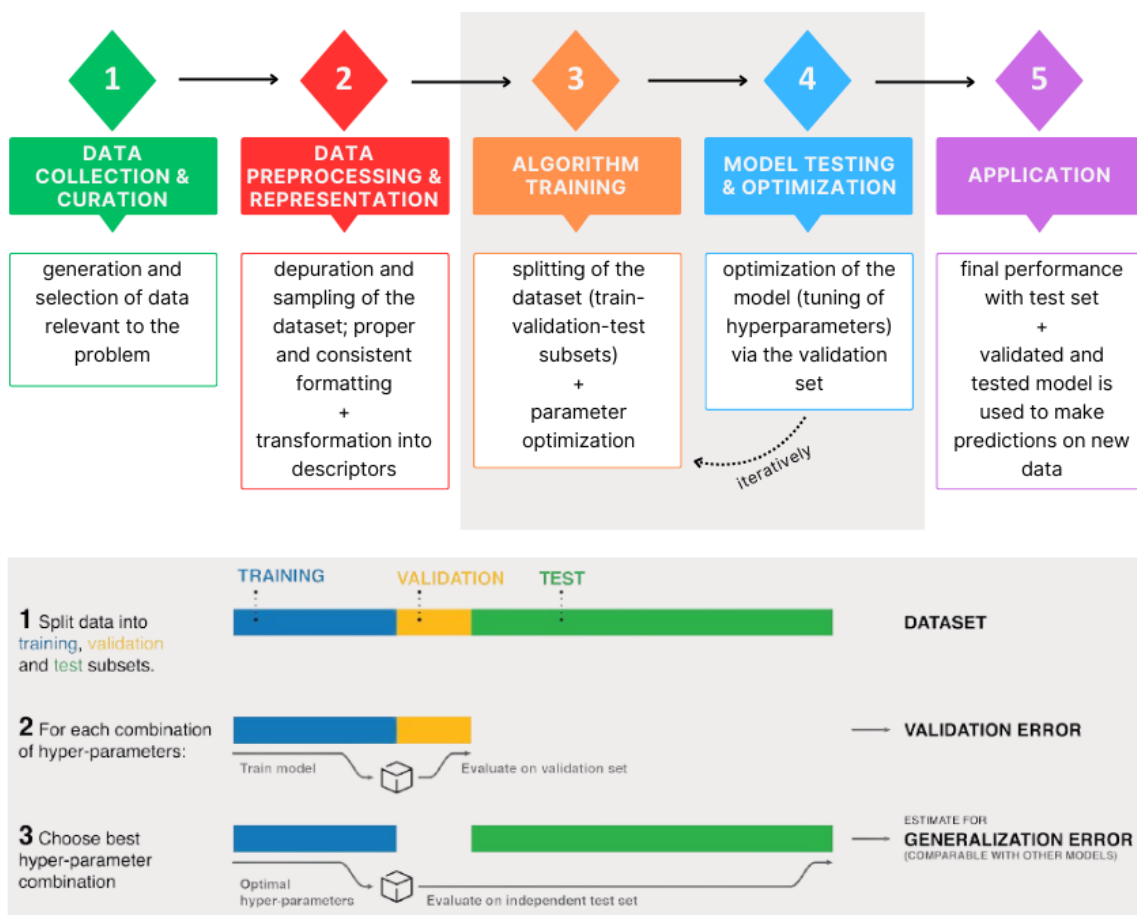


Figure 2.9: Schematic of the ML workflow and a focus [top] on the training of the model [bottom] including an visualization of the dataset splitting and relevant quantities such as errors. Extracted from [72], licensed under CC-BY-NC-ND 4.0.

On the other hand, the parameter vector Θ contains the weights and hyperparameters that define the model. The weights determine the relative importance of specific descriptors and other inputs at different levels of the model, while the hyperparameters control characteristics of the model itself such as details about the architecture or training process. To find optimal values for these quantities, the model is trained. A synoptic view of this process is depicted in Figure 2.9 (top). Data collection and preparation steps (1-2) refer to the previous paragraph, whereas steps (3-4) represent the training outlined in the following.

During training, the available data points $(X, f(X))$ are divided into test and training sets, the latter of which is further split into training and validation subsets, as depicted in Figure 2.9 bottom (step 1). An initial set of hyperparameters is chosen, and the weights of this initial model are optimized accordingly (step 2). For regression problems, this optimization consists on minimizing a loss function, which can range from standard options like those in Equation 2.18 to more task-specific ones. The selection of the loss function is not trivial, as it affects model performance by penalizing errors differently. For instance, while RMSE might overcompensate for some outliers, potentially skewing generalization, a robust regression approach like the Huber loss function may ignore minor discrepancies to achieve a generally accurate model. The goal of the machine learning task should inform the choice of loss function to ensure the desired results.

After the first training, the first iteration of Θ (preset hyperparameters and optimized weights) is tested on the validation set, providing the validation error (Figure 2.9 bottom, step 2). This error measures the deviation of the predictions on the validation set with respect to its known labels according to the metrics of choice (common metrics summarized in Equation 2.18). Then, a new set of hyperparameters is selected, the corresponding optimal weights are found, and the validation error is evaluated again. As a final step, the choice of hyperparameters that provides the lowest validation error is finally adopted, together with its optimal weight set, conforming the final Θ and therefore the trained model. This trained model is evaluated on the test set to obtain its generalization error, and is ready to be used (step 3).

$$\begin{aligned} \text{MAE} &= \frac{1}{n} \sum_{i=1}^n |y_i - \hat{y}_i| & \text{MSE} &= \frac{1}{n} \sum_{i=1}^n (y_i - \hat{y}_i)^2 \\ \text{RMSE} &= \sqrt{\frac{1}{n} \sum_{i=1}^n (y_i - \hat{y}_i)^2} & L_\delta(y_i - \hat{y}_i) &= \begin{cases} \frac{1}{2}(y_i - \hat{y}_i)^2 & \text{for } |y - \hat{y}_i| \leq \delta \\ \delta(|y_i - \hat{y}_i| - \frac{1}{2}\delta) & \text{otherwise} \end{cases} \end{aligned} \tag{2.18}$$

Equation 2.18: Four most common choices for evaluating metrics are presented here: MAE—mean absolute error—, MSE—mean squared error—, RMSE—root mean squared error—and the Huber loss L_δ . In the first three cases, y and \hat{y} represent the actual and predicted labels of datapoint i , of which there are n in total. For the case of the Huber loss, depending on the magnitude of the residual $y_i - \hat{y}_i$ compared to a threshold δ , it is weighted quadratically or linearly scaled to avoid overcompensation of outliers. The combination of the losses at each datapoint is linear and can be weighted to determine priorities in the fitting.

The performance of the trained model is a delicate balance influenced by several factors. The size and quality of the data pool, the choice of descriptors, algorithm, and hyperparameters all play a crucial role. The data must be enough to allow the algorithm to identify the trends in it, and the descriptors must facilitate the task. Likewise, the ideal algorithm with appropriate hyperparameters must be able to recognize such trends efficiently among the available datapoints and consequent noise.

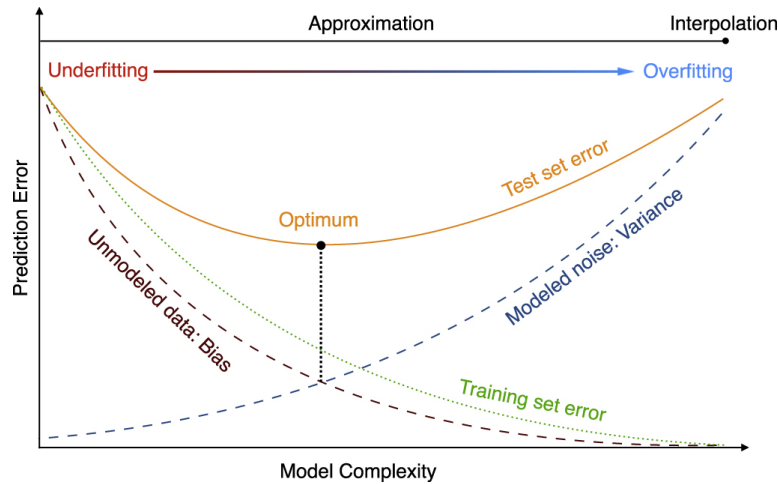


Figure 2.10: A schematic representation of the main magnitudes in ML training, model complexity and test set error, and their relationship with different extremes of the model performance. Reproduced from ref.[71]. Licensed under CC by 3.0.

In the case that any of these links fails, the model performance will be inadequate. Two extremes of poor performance are shown in Figure 2.10: underfitting and overfitting. Insufficient data or an inadequate model, among others, can lead to underfitting, when the model fails to detect or accurately represent the relevant information. If underfitted, the model will present large errors on all datasets. Conversely, a too-complex model or a small dataset can result in overfitting. The overfitted model will perform extremely well on the training set but fail to generalize. Therefore, careful data collection, sampling, and the appropriate choice of algorithm and hyperparameters are essential for the success of the model.

2.6.2. Principles of artificial neural networks

Artificial neural networks are an algorithm initially inspired by the brain structure. In this spirit, the processing units that make up consecutive computation layers are called neurons, and they are interconnected by links or edges in resemblance to synapses in the brain. Nonetheless, current day ANNs no longer strive for biomimetics, and today efforts are focused on efficiency and performance of the trained models^[71]. They are especially relevant in modeling complex systems with large datasets.

In artificial neural networks, an artificial neuron receives a signal from each of its connected neurons as represented by Figure 2.11, interprets their input, processes it applying non-linear activation functions, and outputs it to the next neuron(s). These neurons, or processing units, are organized in layers that can handle different aspects of the ML problem, or at least use different non-linear transformations on them. Two layers are always needed: input and output. Nonetheless, this is a somewhat naïve architecture and complex problems require more layers (hidden layers). Usually at least one hidden layer is also present. Any more hidden layers are denominated deep layers, giving rise to the term deep learning. Thanks to this intricate architecture, artificial neural networks can mimic convoluted patterns in data structures^[73, 74].

Despite the numerous varieties of ANNs, it is possible to define a general routine for their functioning. First, each neuron must combine all the information it receives from the connected neurons. The input $z_j^{(k)}$ to the neuron j in layer k is given by Equation 2.19, where $w_{ji}^{(k)}$ is the weight associated

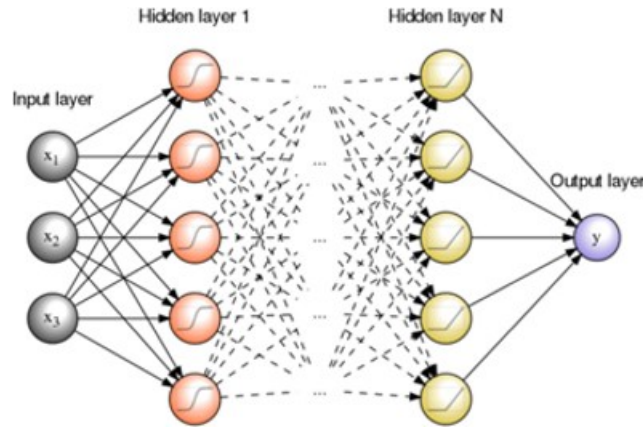
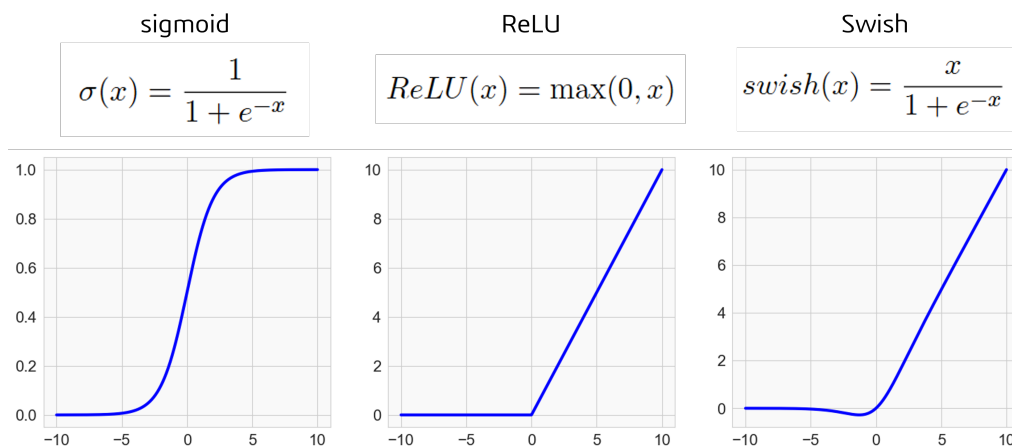


Figure 2.11: Schematic of a neural network showing layers of neurons, divided into input, output and hidden layers, and an example of their interconnection. Many possible interconnection arrangements are possible for different architectures of ANNs. Reproduced from ref.[71]. Licensed under CC by 3.0.

with the connection from neuron i in layer $k - 1$ to neuron j in layer k , $a_i^{(k-1)}$ is the output of neuron i in layer $k - 1$, and $w_{j0}^{(k)}$ is the bias of neuron j in layer k .

$$z_j^{(k)} = \sum_{i=1} w_{ji}^{(k)} a_i^{(k-1)} + w_{j0}^{(k)} \quad 2.19$$

Once the neuron has created the global input value z_j^k , it will perform a non-linear operation on it called called activation function, and its output will be called the activation of the neuron. Below, a few common examples of activation functions: sigmoid, for binary classification problems, the more advanced and common rectified linear unit (ReLU) and the newer swish function, which provides continuity and differentiability in the whole domain, hence facilitating the optimization process.



Given the layered structure of the processing centers in artificial neural networks, it is possible to refine a trained model by continuing the training only on specific layers, typically those closer to the output. This method is known as fine tuning. Fine-tuning allows to maintain the fundamental knowledge from extensive prior training encapsulated in the deeper layers, while still tailoring the

model to the particular features of a specific application.

Artificial neural networks can be classified depending on the design of the interconnections between neurons (feedforward neural networks FNNs vs. recurrent neural networks RNNs), on the presence of specific layers that perform specific tasks like convolutional neural networks (CNNs) or based on the structure of the data. This is the case of graph neural networks (GNNs), favored in materials science for handling graph-like data structures, which are organized in nodes and edges between them that encapsulate their interactions. This aligns perfectly with the interconnected nature of material interactions, as opposed to the grid-like or array-like data structures used in other domains^[75, 76, 77].

2.6.3. Machine learning trained potentials

The role of machine learning in materials science is still incipient, but some major contributions have already been made. There are many possible applications where machine learning can be beneficial, like materials classification^[78] or high-throughput studies of stability to discover new materials as back as 2003^[79]. Another application of machine learning is machine learning trained potentials, also machine learning interatomic potentials (MLIPs), which are the tools used in this work.

These potentials serve as a replacement to the strenuous AIMD protocol. They can predict the interactions in atomic configurations without the quantum considerations, thus lightening the process significantly. With MLTPs, interatomic forces can be used directly into the equations of motion (Equation 2.8). In this way computational costs are reduced from $\mathcal{O}(N_e^3)$ in DFT calculations, increasing with the number of electrons of the system, to a linear increase with the number of atoms $\mathcal{O}(n)$ ^[38, 39]. To our ease of minds, it has been proved that no accuracy is lost by neglecting electrons in the MLTP approach^[40]. Therefore, as represented in Figure 2.12, simulations closer to the working conditions of battery materials have become achievable: longer times, lower temperatures and larger complex systems could be studied atomistically while showing grain formation or degradation, for example.

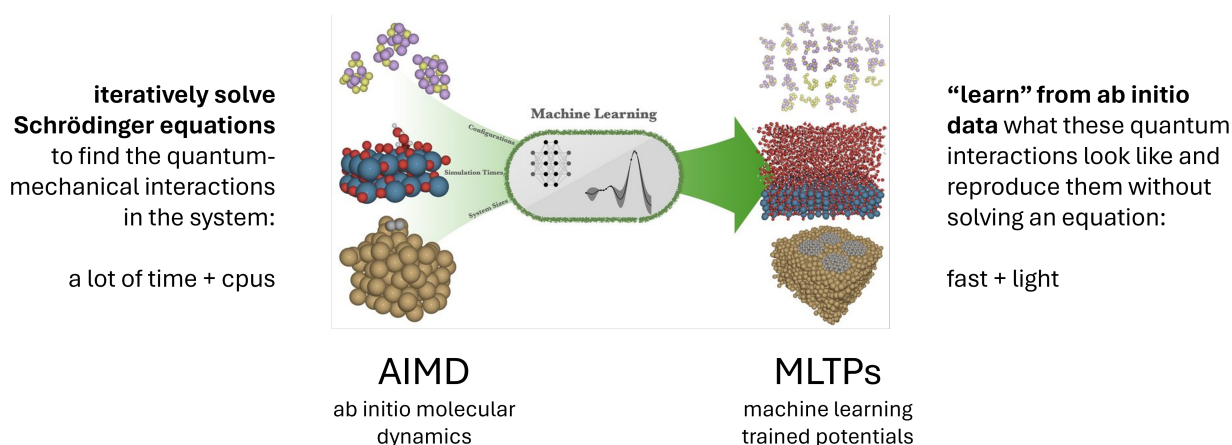


Figure 2.12: Enter Caption

The machine learning problem to fit an interatomic potential is a supervised regression one. There is a feature set (atomic structures) with its labels (total energy and forces from ab initio calculations), mapped over a continuous infinite variable. Ultimately, the goal is to obtain the function \hat{f} that relates both of them, namely the machine learning trained potential itself or the forces it causes. All

the required characteristics of regression problems are fulfilled. As such, several algorithms can fit them. Nonetheless, artificial neural networks have been generally prevalent, starting as early as the 1990s^[69, 80, 81].

Despite all, MLTPs did not flourish until 2007, when descriptors symmetric under translation, rotation and permutation were introduced^[82]. Since then, many algorithms have been used^[69] such as kernel-based Gaussian approximation potentials (GAPs)^[83], spectral neighbor analysis potential (SNAP)^[84] or moment-tensor potential (MTP)^[85] for many applications in the study of cathodes, anodes, electrolytes and interfaces^[86, 87, 88, 89, 90]. Today, they are widely considered as the new paradigm in computational materials science and the key to high efficiency research^[69].

3

Methods

3.1. Bringing disorder and high entropy to Li_3InCl_6

$2 \times 1 \times 2$ and $2 \times 2 \times 2$ supercells were created for the study of disorder and high entropy, respectively. As explained below, the indium and substituted frameworks were carefully designed, whereas the lithium distribution was chosen to minimize Li-Li repulsions. The same lithium sublattice was maintained across ordered and disordered structures, and across pristine and high entropy ones for consistency.

Cationic-site disorder

Partial occupancies are reported in the indium sublattice of Li_3InCl_6 ^[46]. Approximately 11% of the In ions ($\approx 1/8$) were located outside the main site 2b and placed in 4g. Once the symmetry in the supercell is broken by the removal of indium from 2b, the choice of destination 4g will impact the overall structure of the cationic lattice of LIC. To represent such distribution of indium, a multiple of 4 unit cells is required. To this end, we created $2 \times 1 \times 2$ supercells where one indium atom was moved from 2b to 4g. Therefore, in the disordered structures there will be 7 indium atoms in 2b positions, and 1 in a different 4g per structure. In this study, the so-called ordered structure (indium only in 2b) was analyzed in contrast to the four different disordered structures. The disordering process and resulting structures can be seen in Figure 3.1.

Two main effects are caused by the displacement of the one indium atom: changes in the parity of atoms in adjacent indium layers, and different aggregation of indium polyhedra (see Figure 3.2). This results in two differentiated indium layers: the one that indium is removed from, hence resulting in 3 or 4 indium ions there (top layer in the figure, in yellow), and the other layer that might receive it or not, resulting in 4 or 5 ions (bottom layer, brown polyhedra).

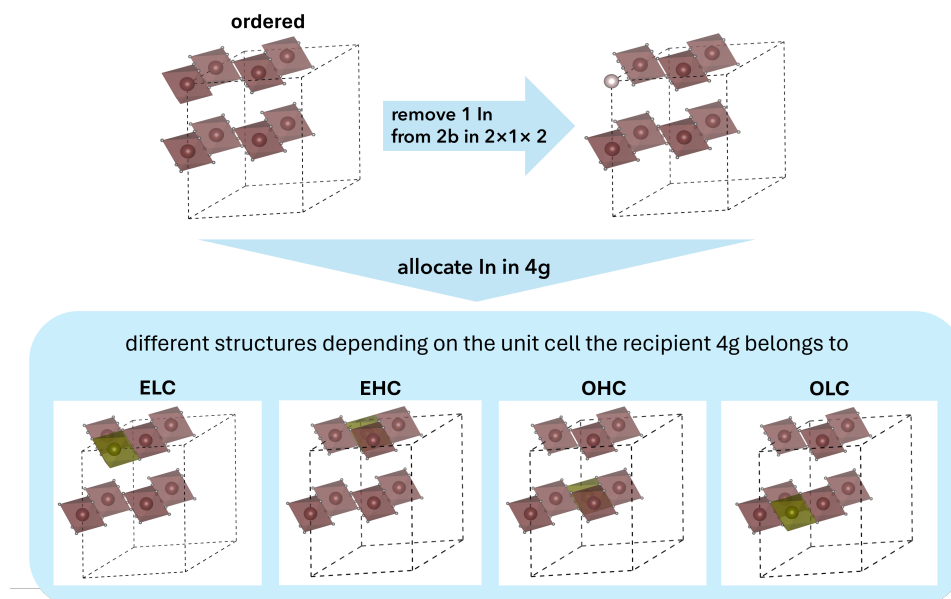


Figure 3.1: Schematic of In sublattice in $2 \times 1 \times 1$ supercell omitting periodic boundary conditions to illustrate the origin of the disorder in the cationic sublattice of Li_3InCl_6 . The four resulting structures (ELC, EHC, OHC and OLC) and the original ordered structure are studied in the following sections.

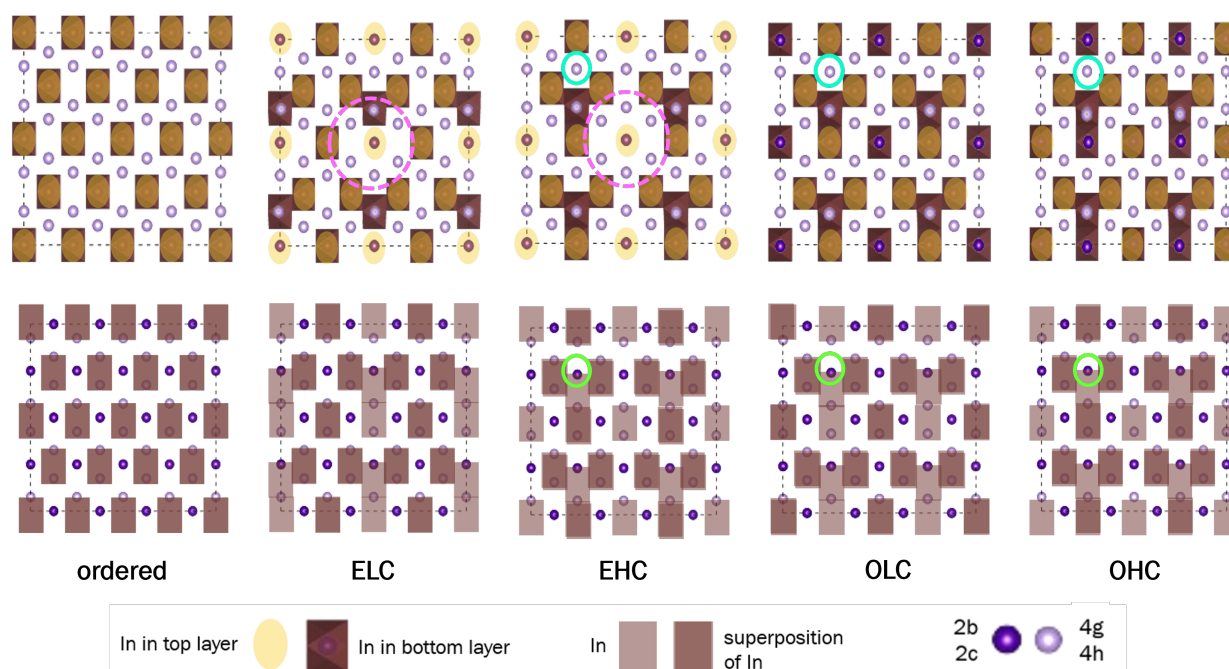


Figure 3.2: Different indium sublattices for the five structures O, ELC, EHC, OLC and OHC and their effects on available sites and paths to lithium distribution in the indium layers (**top**) and lithium layers (**bottom**). Especially relevant strangling or open distributions of the octahedra are signaled by colored circles and discussed in the text.

The structures are named accordingly with E (even) or O (odd) to describe the distribution of In atoms (4:4 or 3:5, respectively), and LC or HC to describe the low or high level of clustering in every

second In layer. In the even configurations, low and high clustering is determined by the number of aggregated indium polyhedra (3 or 4), whereas in the odd case there are always 4 conjoined polyhedra in the clustered layer. The difference then lies in how the indium aligns along consecutive layers (OHC–three, one at each end–, or OLC–two, at the base). This can be seen in both Figure 3.1 and Figure 3.2.

As per the latter, the different configurations in the indium sublattice may affect the diffusion of lithium, the study of which is the focus of Section 4.1.4. EHC and the odd structures display four edge-sharing octahedra, enclosing one of the 4g positions in the lithium layer a 4h in the indium layer in a very unfavorable area due to Coulombic distributions (marked by blue circles in the case of 4g and green ones in the case of 4h). At the same time, the even distributions create wider spaces in the indium layer for the lithium to disperse through, signaled by the pink dashed circle. It is expected that the specifics of these arrangements will impact the preferred sites for lithium and have an effect on its transport.

High entropy

For the creation of high-entropy structures, the indium in the original ordered configuration is changed into a mix of five (HE5) or four (HE4) elements: Sc, Yb, Zr and Lu, including indium or not for HE5 and HE4 respectively. All of them share ionic charge 3+ but for Zr, with charge 4+, and have atomic radii ranging between 155pm and 194pm^[52]. These differences introduce a degree of lattice distortion which is suspected to play a role in diffusion kinetics.

The high-entropy $\text{Li}_{2.8125}\text{In}_{0.1875}\text{Lu}_{0.1875}\text{Sc}_{0.25}\text{Yb}_{0.1875}\text{Zr}_{0.1875}\text{Cl}_6$ (onwards, HE5) and the medium-entropy variation $\text{Li}_{2.75}\text{Lu}_{0.25}\text{Sc}_{0.25}\text{Yb}_{0.25}\text{Zr}_{0.25}\text{Cl}_6$ (HE4) were studied. Notably, an exact equimolar configuration for HE5 is unattainable within the limits of DFT and AIMD, as 10 unit cells (200 atoms) would be needed. The computational toll of that system size is too large for ab initio methods. Therefore, 2x2x2 supercells (160 atoms) were simulated as a close alternative, which allowed for a cationic ratio of 3:3:4:3:3 (In:Lu:Sc:Yb:Zr) in HE5. Equimolarity is possible in the case of HE4, where all substituents have $x = 0.25$ (four atoms of each are present in the 2x2x2 supercell).

Five structures were selected for the study of each HE5 and HE4 from the many that emerge from the combination of species. The structures considered for each HE5 and HE4 range from the most ordered configuration possible (substituents organized in layers) to the most dispersed one, including an in-between distribution and two randomized configurations for completeness (Figure 3.3). From each group of HE structures, that with the lowest ground state energy was selected for the subsequent analysis of diffusivity (Figure A.4).

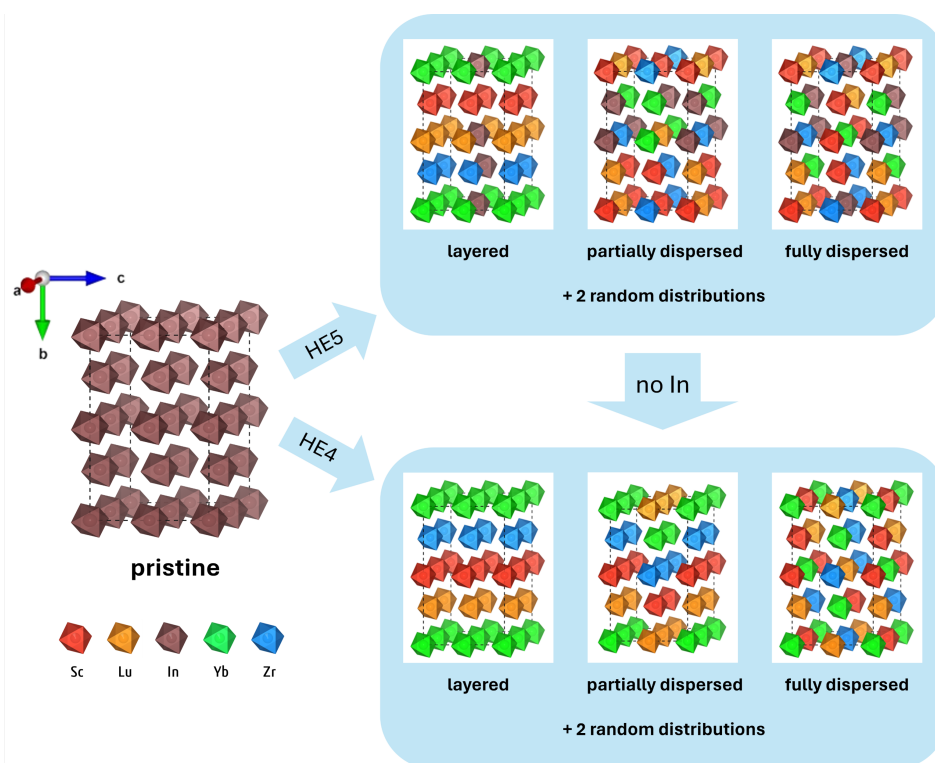


Figure 3.3: Diagram of the creation of HE structures for the case of five (HE5) and four (HE4) elements in the cation sublattice, originally composed of only In. Five different configurations were built for each of the compositions with different degrees of order in the sublattice, including two randomized configurations.

In both cases the lowest energy was achieved in the randomized distributions shown in Figure A.3. However, all the considered configurations had energies within the expected thermal fluctuations, rendering all of them potentially present in bulk materials.

3.2. Computational specifications

The supercells were created with Materials Studio^[91] and VESTA^[92] from crystallographic information from ref. [46]. Using an in-house Python script, 30,000 randomly assigned lithium configurations were generated for the 2x1x2 supercells. For the 2x2x2 supercells, 100,000 configurations were generated. In this pre-screening, the chemically appropriate amount of lithium was positioned in a random selection of sites among those available to them, and only electrostatic Li-Li interactions were considered by the method of undamped shifted force^[93]. The configuration with the smallest repulsions was selected to start the usual ab initio calculations with the Vienna Ab Initio Simulation Package software (VASP)^[94].

For AIMD studies, first DFT relaxations of the supercells were performed using the projected-augmented wave approach (PAW)^[95]. The generalized-gradient approximation (GGA) Perdew-Burke-Ernzerhof potential with correction for solids PBEsol^[96] was chosen after a study of volume convergence against other common pseudopotentials. The electronic convergence was defined at 10^{-4} eV. For the study of disorder with 2x1x2 supercells, we set the plane-wave energy cutoff at 520 eV and

k-mesh 3x3x3 over Γ . For the high entropy samples with 2x2x2 supercells, an energy cutoff of 400 eV and k-mesh 2x1x2 over Γ were selected.

The ab initio molecular dynamics simulations were performed in the NVT ensemble from the relaxed structures, with a timestep of 2fs and using the Nosé-Hoover thermostat. The cutoff energies were chosen at 400 eV for the smaller supercells and 300 eV for the larger ones. The pseudopotential and convergence criterion were maintained the same as in the relaxations. For the study of disorder, NVTs were recorded at 550K, 700K, 775K, 850K, 925K and 1000K for 200ps. For high entropy, they ran at 700K, 800K, 900K, 1000K, 1100K and 1200K during 120ps in the case of HE5 and 90ps in the case of HE4 (due to the expensive computational requirements of such big AIMD simulations).

The classical molecular dynamics simulations were exclusively conducted using machine learning trained potentials. In particular, a fine-tuned model of CHGNet^[97] (referred to as FT or CHGNet-FT hereafter) was utilized via the LAMMPS software^[98]. Similarly to the ab initio studies, first a static relaxation was conducted and the NVT simulations were started from the resulting structure, all using the FT potential. Only relative values for the energy convergence criterion for relaxations can be passed to LAMMPS, so a blind estimation for this value was chosen (10^{-16}). The relaxations stopped before arriving at this criterion but reached $\Delta E = 10^{-12}$ eV, exceeding the ab initio criteria and were therefore considered satisfactory. In the molecular dynamics simulations, for consistency with the ab initio studies, the timestep was also chosen to be 2fs and the simulations span the same duration at the same temperatures as AIMDs, kept by a Nosé-Hoover thermostat as well.

In all scenarios, the first 2.5ps were considered to be the equilibration time of the system, and therefore disregarded in the calculations. The simulation data was analyzed with the Python packages GEMDAT^[99] and Pymatgen^[100]. Additionally, we developed code based on the GEMDAT library to analyze the diffusivity contributions per axis and per category of jump (cross-layer, within In layer or within Li layer), as discussed in Section 2.5.1 (Appendix B).

3.2.1. Fine tuning of a machine-learning trained potential

CHGNet was the pretrained MLTP model chosen to initiate the machine learning methods in the group, as it has been praised for its integration of charge-based phenomena through magnetic moments without the necessity to explicitly include electrons^[101]. Its impressive pretraining dataset of over a million structures and streamlined fine tuning process made it an attractive choice. Moreover, CHGNet contains 412,525 parameters to describe the complexity of atomic interactions. The pretrained model was subsequently fine tuned to better represent our system.

The dataset used for fine tuning consisted of static force calculations and a few full relaxations of uncorrelated frames from the previous AIMDs of the 2x1x2 cells. To this end, an autocorrelation analysis was performed using block-bootstrapping^[54] (Figure A.6), and the autocorrelation time was decided to be 5,000 steps. Therefore, 600 uncorrelated frames were obtained (120 per each structure—O, ELC, EHC, OHC and OLC). For all of them, a static calculation of their forces was performed with ENCUT = 450 eV and EDIFF = 10^{-6} eV. Additionally, 20 full relaxations of the ELC structure at 505K were included ($\approx 3\%$ of the full set), introducing some volume variability in the dataset as well.

For the fine tuning, thanks to the streamlined process by CHGNet, formatting and transformation into descriptors is not required to do manually. The VASP output files from the relaxations were processed directly by CHGNet functions and no hands-on work was needed. CHGNet is pretrained on the structures from the 2022 Materials Project database, so given the limited size of our dataset

and the smaller historical interest on halide electrolytes we chose a training set larger than typical. The training set represented 95% of the total data, and 20% of it was allocated for validation. This left a reduced test set which could lead to skewed generalization metrics. This was an intentional trade off to prioritize the thorough training of the model. As a consequence, the performance of CHGNet-FT was manually assessed, including the 2x2x2 supercell which was not a part of the fine tuning dataset.

The FT model was trained on energies, forces and stresses with relative weights of 1:1.5:0.15 using the optimizer Adam and scheduler CosLR. The training encompassed 50 epochs with learning rate 10^{-3} using the Huber loss (Equation 2.18). Only the embedding layers were retrained (atom, bond and angle embedding), together with the reference energy AtomRef. This was needed to reconcile the data from the pretraining of CHGNet and our own data, which had been calculated using different pseudopotentials.

4

Results and discussion

The broad topic investigated in this work must be narrowed down to concise and manageable research questions that can be tackled systematically. Therefore, research will be addressed in three main steps. First, cationic disorder in the In layer was studied as an approach to the general characterization of the diffusive properties of Li_3InCl_6 and the effect of disorder itself: ordered vs. disordered LIC. Secondly, high-entropy structures where In was substituted by a mix of several elements were compared to the pristine In-only sample: pristine vs. high entropy. Finally, the first strides towards incorporating machine-learning techniques as a key complement of ab initio studies have been taken: ab initio vs. MLTP. In this way, the three aforementioned research questions can be examined to shed light on each of the topics.

4.1. Characterization of the diffusivity of Li_3InCl_6 and effects of disorder

In this section, we present the study of the diffusion characteristics of Li_3InCl_6 for different atomic arrangements of the material. The ordered structure O and the four disordered structures ELC, EHC, OLC and OHC in the $2 \times 1 \times 2$ supercells are analyzed side by side in an effort to understand and characterize the diffusion of lithium in this solid electrolyte.

First, the structural integrity of the cells is verified, as formation of stacking faults has been reported experimentally in similar materials and found computationally in LIC itself^[47, 102, 103]. Following, the diffusivity in the different structures is investigated in two ways: MSD diffusivity and jump diffusivity via jump analysis. Previous literature agrees that diffusion in Li_3InCl_6 is dominated by the vacancy mechanism and that Li movement follows octahedral-tetrahedral-octahedral paths^[19, 46, 48]. Nonetheless, there is less consensus on activation energies, conductivity at room temperature and dimensionality of diffusion. Our contribution to this discussion is presented in this section, alongside with the study of possible differences arising from different lattice configurations.

A comprehensive summary of all results and errorbars introduced in this section can be found in Appendix A.

4.1.1. Structure stability

To confirm the stability of the electrolyte, the movement of indium and chlorine atoms in the NVT simulations was studied. While lithium is expected to diffuse and move throughout the simulation cell, well-behaved cationic and anionic sublattices should remain in place. However, and interestingly, unexpected movement was detected in the cationic sublattice of indium for all the disordered structures, as per the indium MSD plots in Figure 4.1. Notably, the ordered structure does not present any indium displacements.

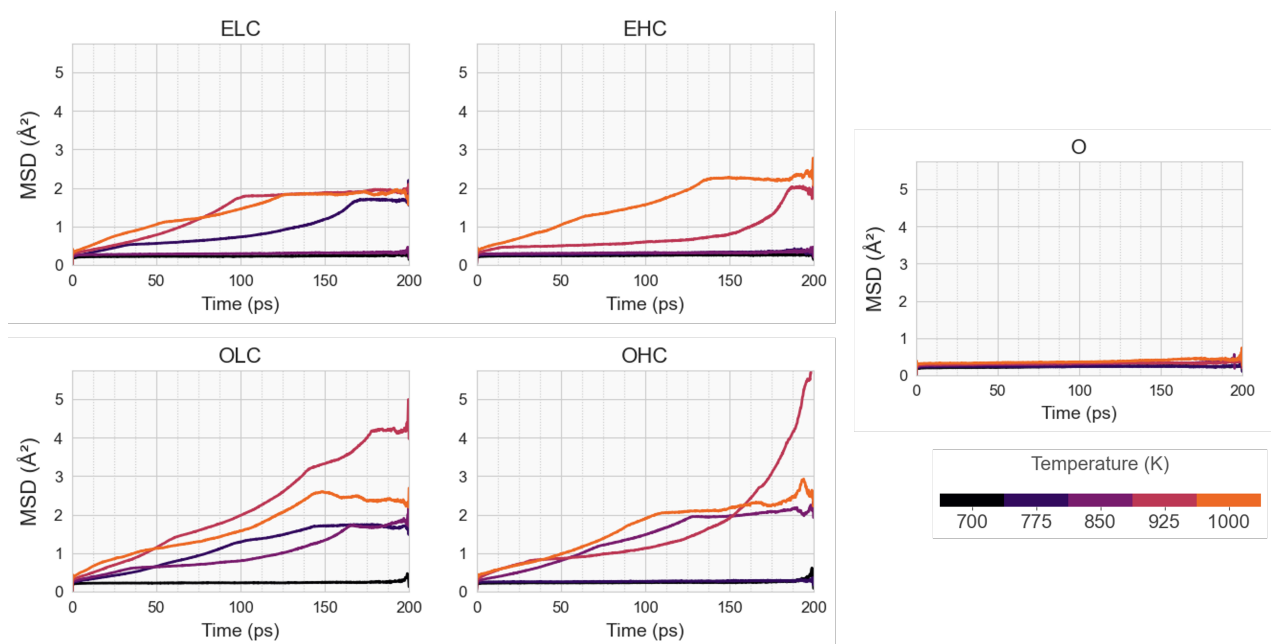


Figure 4.1: Mean square displacement evolution of the indium atoms at different temperatures for each structure. While all the disordered structures present a varying degree of mobility, the In sublattice in the ordered structure O remains intact.

While this movement does not represent the formation of stacking faults, a certain degree of instability is introduced. In that case, a coordinated movement of whole lattice planes would occur. For us, the displacement of indium was not accompanied by the chlorine sublattice, as formation of stacking faults would entail. Instead, more detailed examination shows that only one or two atoms move in each case. Indeed, this movement has a more erratic nature: its presence and magnitude do not directly correlate with temperature, and often atoms return to their original positions or close by them.

The specific movements of the indium atoms can be seen in Figure 4.2, not revealing any particular tendency. As a reminder to the reader, positions 4g and 2b belong to the indium layer, and 4h and 2c belong to the lithium layer. In structure O all indium is in site 2b, and in the disordered structures one of the indium atoms has been removed from 2b and placed in site 4g. Notably, the movements do not seem to represent reconfigurations towards a preferred, more stable arrangement common to all structures. ELC (the even, low clustering structure) returns to the ordered configuration, while

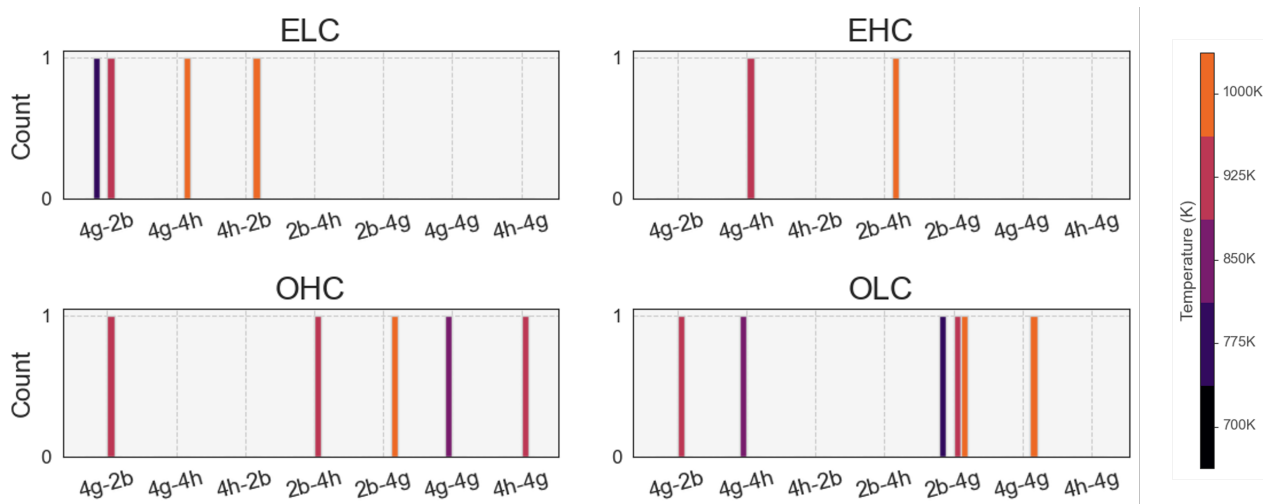


Figure 4.2: Bar plot summarizing the indium hops during the NVTs (temperature indicated by bar color). On the x-axis, the labels of the jumps, while the y-axis shows how many jumps have occurred. Positions 4g and 2b belong to the In layer, and 4h and 2c belong to the Li layer.

its high-clustering counterpart EHC has an opposite behavior, moving an indium to the Li-layer. In the odd configurations OLC and OHC, the indium in 4g tends to be joined by a second atom that leaves its original position 2b. Sometimes, indium even visits the Li layer.

Given the seeming randomness in this movement no further conclusions can be drawn from this analysis apart from identifying a certain degree of indium mobility at high temperatures. The analysis of lithium diffusivity is carried out normally in the following sections despite these small displacements in the indium sublattice.

4.1.2. Bulk diffusivity and activation energy

The MSD curves from the NVT simulations between 700K and 1000K are well behaved, growing sufficiently linearly with time and increasing their slope as temperature increases (Figure 4.3). Therefore, they are adequate to perform typical Arrhenius studies of diffusivity and extrapolate the activation energy and the conductivity at room temperature, as per Section 2.5.1. In contrast, the runs at 550K displayed step-like MSD curve in several of the structures and were therefore excluded from the analysis.

The fits for each structure are collected in Figure 4.4, resulting in $\sigma \sim 0.2 - 0.3$ mS/cm for all disordered structures, and $\sigma = 0.856$ mS/cm for structure O at room temperature. Recently published experimental results concur in conductivities around 0.47-2.04 mS/cm for LIC^[19, 23, 26, 27, 46], showing good agreement. Computational studies^[47, 104, 105] report more varied results, ranging from 0.001-0.01 mS/cm to 12 mS/cm. Disparity between experimental and computational investigations is natural and expected^[48, 106], as experimental studies often account for phenomena happening at many length scales and impurities, for example. Meanwhile, computational methods are limited due to small viable system sizes and simulation times, and are sensitive to specific settings and initial configurations, which also explains the discrepancies among them. For that reason, comparison with literature will focus on qualitative aspects like diffusion mechanisms or preferred diffusion direction.

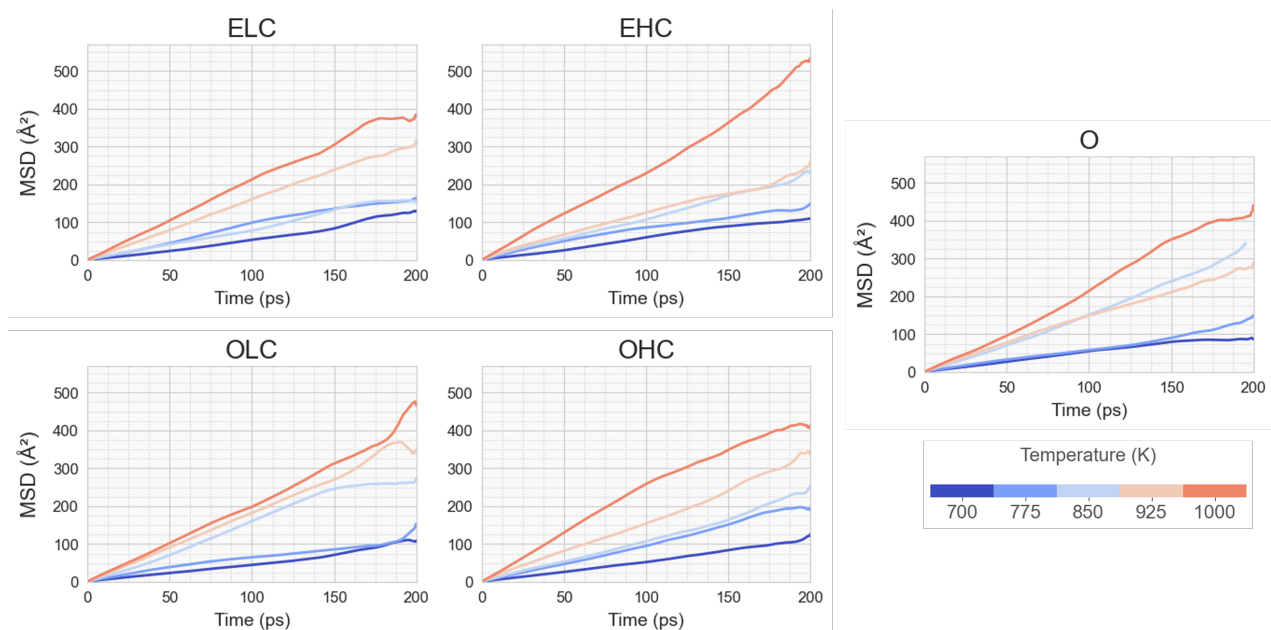


Figure 4.3: Mean squared displacement of the lithium atoms at different temperatures (700K, 775K, 850K, 925K and 1000K) for each structure.

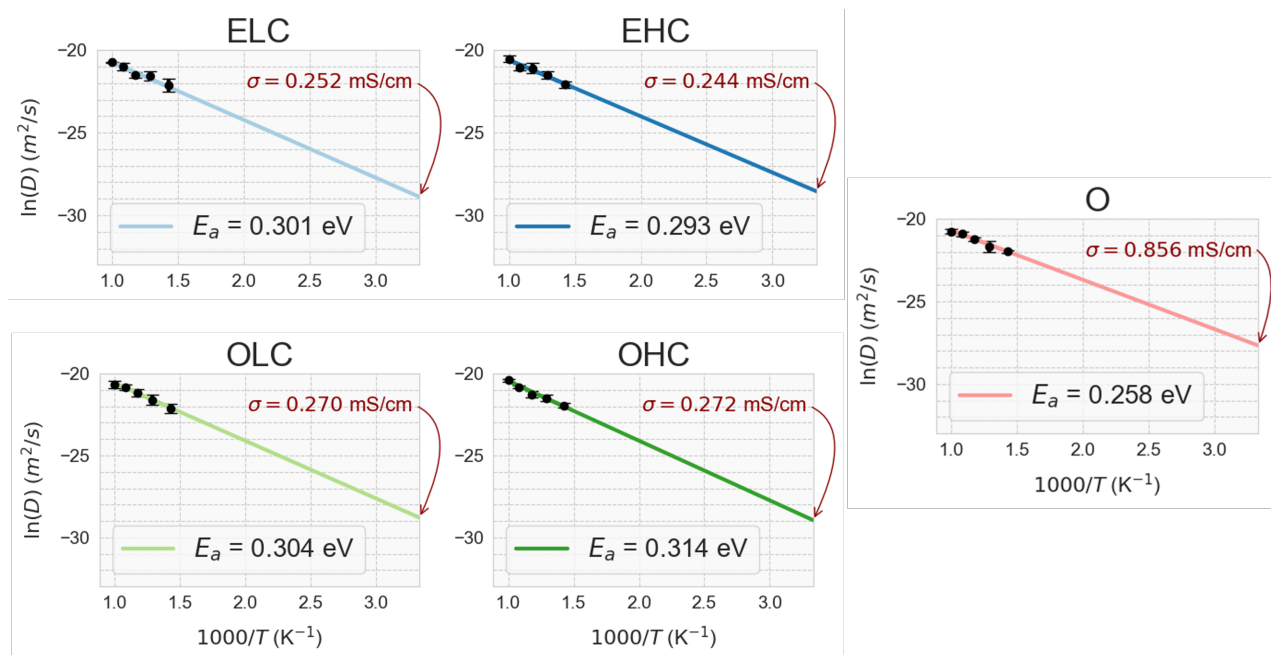


Figure 4.4: Arrhenius plots for the total MSD diffusivity of each structure. Datapoints at 700K, 775K, 850K, 925K and 1000K. Activation energies from the slope of the fit are shown in the graphs, as well as the extrapolated value of ionic diffusivity at room temperature. Errorbars can be seen in Figure 4.6 and in Appendix A.

From the fittings we obtained sensible activation energies, well aligned with the experimentally reported data for similar halide solid electrolytes such as Li_3YCl_6 , Li_3YBr_6 , $\text{Li}_3\text{YBr}_3\text{Cl}_3$ (0.2-0.4 eV) and LIC itself (0.347-0.325 eV)^[19, 23, 24, 48, 102, 103]. Computational evidence also supports our results, having found an activation energy of 0.294 eV^[105]. Only one other computational study^[47] presents

a significant deviation, publishing energies of 0.13-0.15 eV. However, the limited simulation times analyzed in this study (20ps) could affect the statistical robustness of its results, and the ballistic regime may have significantly influenced the outcomes. In light of these observations, our results, which are in good consonance with the majority of the literature, seem to represent a well-contrasted behavior for the diffusion of Li in this solid electrolyte.

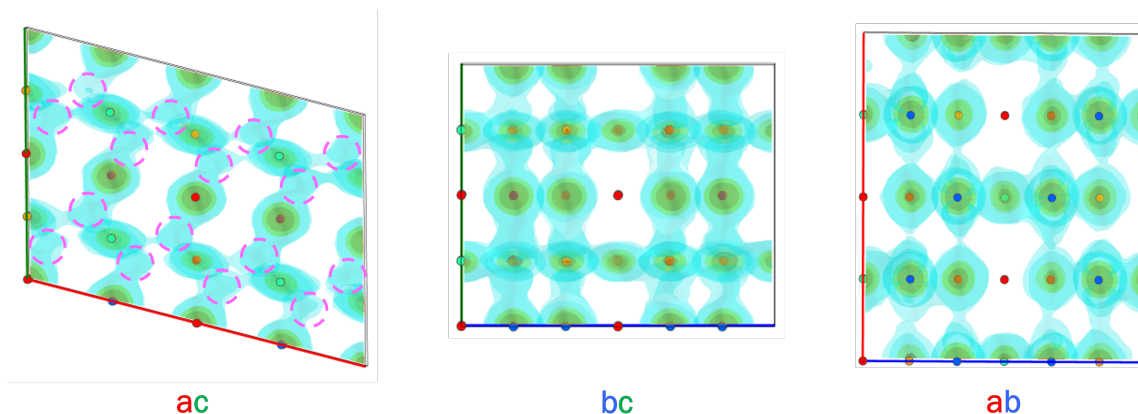


Figure 4.5: Lithium density plot to show the diffusion path between octahedral positions and connectivity (structure O, 775K). Tetrahedral positions $8j$ are signaled by pink dashed circles, clearly visited in the diffusion path. Moreover, 3D connectivity is evident. High temperature was chosen to show all possible paths, but equivalent features are observed across all structures and temperatures.

Additionally, the expected oct-tet-oct diffusion path is confirmed by our results, as exemplified by Figure 4.5 (left), and consistent across all temperatures and structures. All movements between layers necessarily pass through the $8j$ tetrahedra, with the tetrahedrals acting as transitional states. While they are clearly visited by the ions, $8j$ positions do not show as prevalent concentration of lithium as the other sites, hence validating the hypothesis that $8j$ positions are only intermediate steps. Moreover, no lithium is visible outside the expected paths, and the density probability plot exhibits three-dimensional connectivity, further confirming previous results.

This preliminary investigation is in reasonably good agreement with current knowledge. It demonstrates an average activation energy of 0.294 eV across all configurations, being slightly lower for the ordered structure, and suggest conductivities at room temperature around $10^{-7} - 10^{-6}$ S/cm. Moreover, 3D connectivity is proved and the diffusion path across layers was found to be octahedral-tetrahedral-octahedral in the cross-layer transport.

4.1.3. Dimensionality of diffusion

There has been contradictory evidence regarding the dimensionality of diffusion in C2/m halide SEs: Helm described isotropic 3D diffusion in LIC^[46], whereas others found preferences for both within-layer diffusion^[104] or cross-layer diffusion^[103]. To investigate any preferences in the diffusion direction in LIC, we performed an Arrhenius fit on D_{MSD} separated per axis and found no distinct preferred direction. From our data, we could restrict the expression of MSD diffusivity Equation 2.16 from $\Delta \mathbf{r}_i = |\mathbf{r}_i(t_0+t) - \mathbf{r}_i(t_0)|$ to $\Delta \mathbf{a}_i$, $\Delta \mathbf{b}_i$ or $\Delta \mathbf{c}_i$. The results from this analysis are collected in Figure 4.6 and analyzed below.

The first result to extract from the graph is the pronounced agglomeration of datapoints, with

no distinct outliers, especially when considering the errorbars. No clear favorite direction can be observed, as the *a priori* lower activation energy along direction *b* is concealed by the large errorbars. In conjunction with the upcoming study of lithium density distribution (Figure 4.9), 3D diffusion is concluded for LIC.

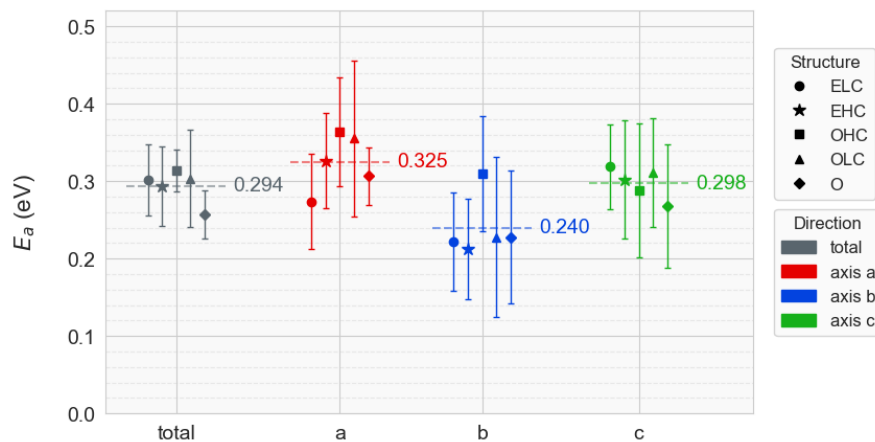


Figure 4.6: Comparison of activation energies from MSD diffusivities for each structure (symbol) and axis (color). The dashed line across each cluster represents the simple average of the cluster (average activation energy per axis).

Nonetheless, the dimensional study per axis contains convoluted information for the vastly different indium and lithium layers in the *a* and *b* axes, which could be responsible for the large errorbars. To rid our data from the such large uncertainties, a study of diffusivity per layer was carried out. The total jump diffusivities from all jumps in a same category (In within-layer, Li within-layer or cross-layer) were fitted to an Arrhenius relation to deconvolute the lithium migration in both layers. This resulted in improved resolution of the activation energies as per Figure 4.7.

The activation energies via jump diffusivity per layer exhibit reduced errorbars compared to the study per axis. Furthermore, the suspected pattern is confirmed: diffusivity in the lithium layer is favorable and comparable to that across layers, whereas movement in the indium layer is more restricted. Hence, larger errorbars are concentrated in the indium layer and activation energy is higher as well, although inconclusive for this reason.

The elevated activation energy of cross-layer jumps in structure O is of particular interest. this is especially relevant as cross-layer jumps directly correlate with migration along *c*, for which structure O showed no distinctive behavior. Further investigation showed that a significant amount of lithium density was not captured as belonging to any specific sites for this structure (Figure 4.8, left), leading to diminished values for the jump diffusivity of cross-layer jumps in structure O. Thus, the cross-layer activation energy for structure O is deemed an artifact of the analysis tools. The disordered structures, however, show acceptable density capture rates (around 90%) and therefore no other points from the figure need to be disregarded.

Considering both dimensionality analyses, no strongly preferred direction has been found: diffusion in the *ab* plane (within-layer) is almost as probable as diffusion along *c* (cross-layer). The only discernable differences lie in the diffusivity in the In layer due to the scarce movement in that layer. Regardless, our findings suggest that the interlayer connectivity renders the diffusion process tridimensional, in support of [46].

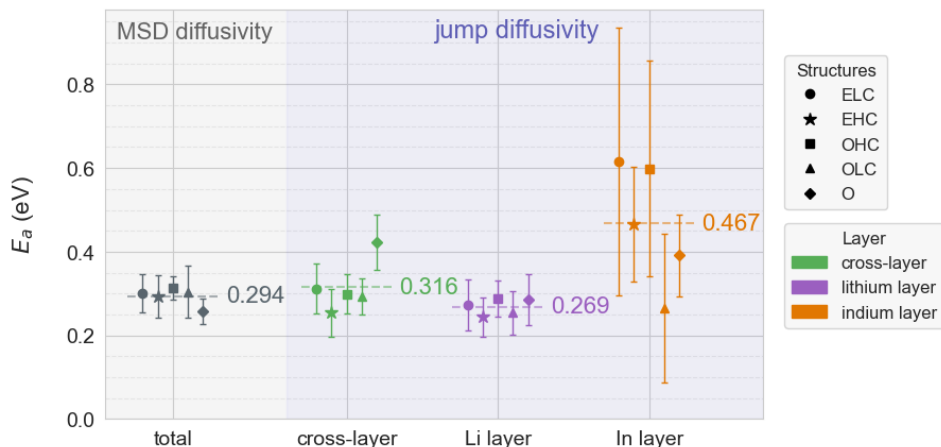


Figure 4.7: Activation energies per layer (axis, color) and structure (symbol) calculated from jump diffusivity, and total MSD diffusivity for reference

4.1.4. Effect of cationic-site disorder

Our study of the lithium occupation per site revealed that for the ordered structure around 35% of lithium is unaccounted for (Figure 4.8 left), as suspected. Furthermore, the density distribution within the cell (Figure 4.9) ensures that lithium does not visit sites other than 2c, 4h, 2b, 4h and 8j, and including 8j in the occupation analysis does not significantly increase the total capture for structure O (Figure A.2). Therefore, the missing lithium in structure O is not at a site outside our scope. It must then be distributed in the space between the known sites.

This hypothesis is sustained by the study of occupation at the sites when their radii are increased selectively (Figure 4.8, right). It shows increasing concentration of lithium beyond 1.8\AA , which, as previously noted, cannot be attributed to the tetrahedra (at around 2.2\AA from all the sites shown). The density distribution in Figure 4.9 offers easier access to these considerations. The figure shows better ion transport in O in opposition to ELC (as an example of disorder, for clarity, showing characteristics shared by all the disordered structures).

Indeed, the density distribution in the cell shows connections along the a axis in the ordered structure that are absent in the disordered case (green rectangle). At the same time, the existing paths in the disordered structure are less pronounced and uniform, as indicated by the shade of blue (purple, and red rectangles), and are narrower (red rectangle). Additionally, lithium concentrates at certain sites (black circle), in contrast with structure O. Therefore, lithium mobility is expected to be higher in the ordered structure, as backed by the calculated conductivity.

The enhanced conduction of lithium in the ordered structure is contrary to the conclusions from a computational study on LIC from 2022^[47], which reported enhanced mobility of Li ions in a disordered configuration, and other findings for similar halide SEs, as previously established. Concurrently, nonetheless, the experimental investigation from Li *et al.*^[23] concluded that a less crystalline sample of Li_3InCl_6 showed lower diffusivity than its crystalline counterpart. Our results are consistent with the latter experience.

Naturally, in experiments the crystallinity of the sample is impacted by a broader definition of disorder than the one we are studying, such as including defects and impurities. Therefore, only a cautious correlation can be established with our observations, but such a correlation is nonetheless

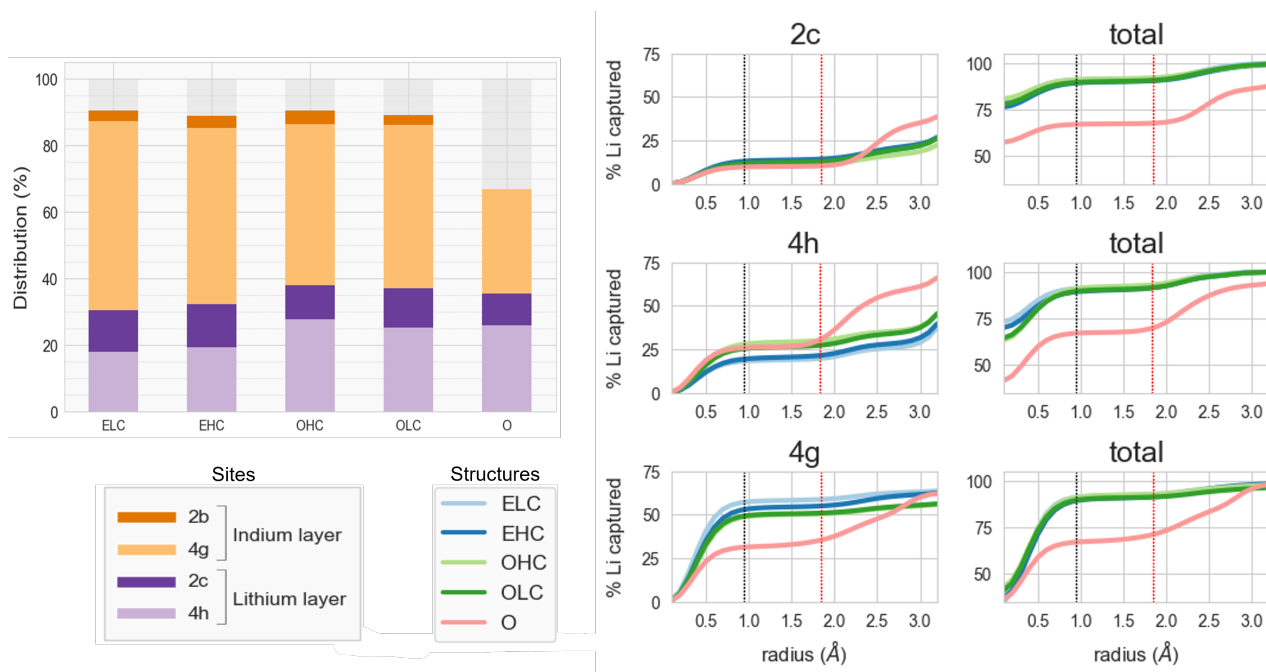


Figure 4.8: Analysis of occupation of lithium. Snapshots correspond to 550K, but consistent results are found across all temperatures. **Left:** distribution of the lithium density among the defined sites, per structure. The percentage of time that lithium spends on average in each of the sites is shown. **Right:** evolution of the total lithium density assigned to a site as only the radius of that site increases, per structure (color). On the left column, the percentage captured at that site. On the right, how that impacts the total lithium count. The vertical lines represent the radius selected for the analysis (double the vibration amplitude, in black) and the distance until overlap with the nearest site (red). Site 2b omitted as it is fully occupied for O.

present. Moreover, the same detrimental effects of disorder have been found in samples of Li_3YCl_6 synthesized with the same methods^[19] as Li_3InCl_6 . In that case, the lower crystallinity was even directly attributed to cation-site disorder, further backing our findings.

Finally, a comparison can be established among the different types of disorder. ELC, EHC, OHC and OLC exhibit considerably different characteristics which could have an impact on lithium mobility. Due to the aforementioned movements of indium, the activation energies and conductivities extracted from the Arrhenius relation contain information pertaining to many indium configurations outside our initial set. Therefore, they are not adequate to compare the consequences of clustering or parity of indium. Yet, data at 550K and 700K is representative of the original structures and can be used to establish a comparison. Figure 4.8 shows a trend in the distribution of indium that correlates with the specifics of the configurations.

At 550K and across all temperatures, odd structures show less indium layer occupation, which is expected due to the large indium clusters caused by five indium octahedra in every other layer. Within this first split, OLC and OHC also show different distributions of lithium in the lithium layer. In OHC the indium cluster completely surrounds the 2c position (four at the bottom and three on top, as per Figure 3.2), and this is likely a reason for the preference of 4h rather than 2c. Occupation of 2c is easier in OLC, where 2c likely feels smaller repulsion from indium as it is less concentrated around it.

In contrast, for the even configurations clustering appears to have minimal effects. It seems that the space created by the removal of indium from 2b, when not overly blocking the adjacent layer as

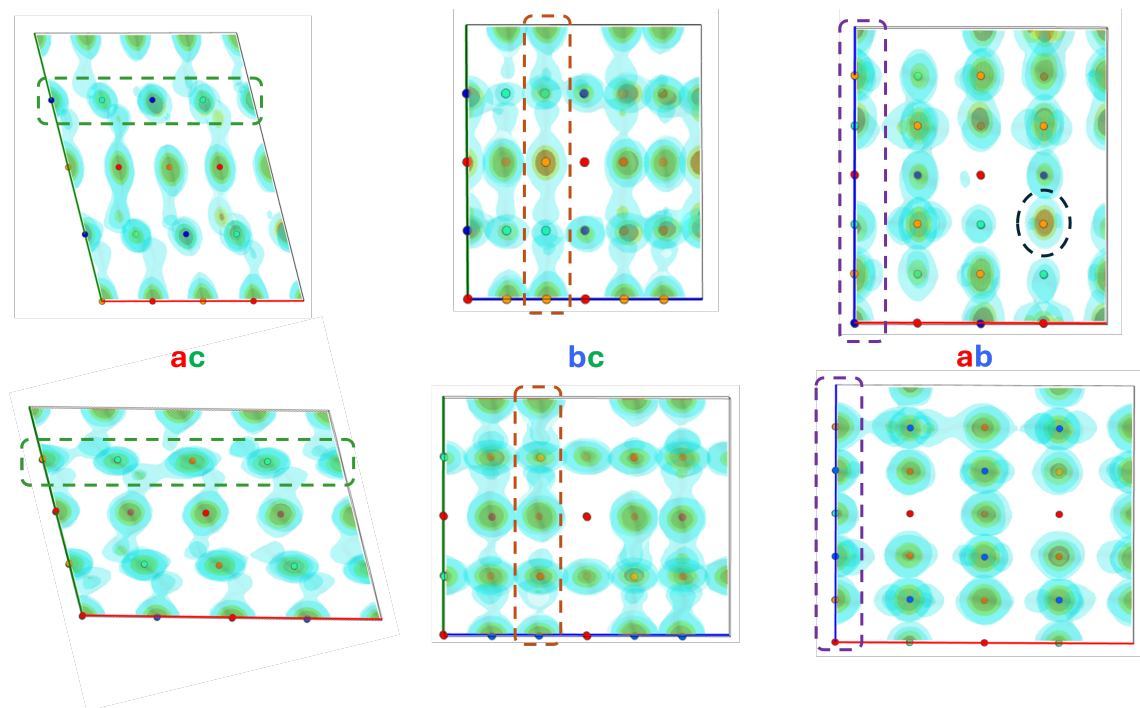


Figure 4.9: Density distribution plots for the disordered structure ELC versus the ordered structure, at 550K. Differences in the lithium distribution are signaled by dashed rectangles. In green, the better connectivity of O. In red and purple, the stronger and wider paths along b and c . In black, the higher concentration at sites in the disordered structure. Structure ELC is chosen for ease of comparison, but EHC, OHC and OLC show the same features).

in the odd cases (Figure 3.2), is sufficient to facilitate the presence of lithium in the indium layers overall, regardless of the agglomeration.

It is difficult to say how and if the specifics of the cationic-site disorder impact lithium transport in Li_3InCl_6 , as statistics at lower temperatures are not enough to obtain estimations of the diffusivity independent of the higher temperatures. Nonetheless, the effects on the occupation of sites are not drastic and from our results it is likely that the nature of the disorder has little impact on the overall performance of LIC as a solid electrolyte. However, it is possible to conclude that any disordered configuration is outperformed by the ordered structure as has been proved quantitatively by the activation energy and qualitatively by the distribution of lithium in the supercells.

4.2. Effects of high entropy: multicationic substitution

To test the effect of high entropy in the performance of Li_3InCl_6 we chose to substitute In with a mixture of five elements (In, Lu, Sc, Yb and Zr), resulting in $\text{Li}_{2.8125}\text{In}_{0.1875}\text{Lu}_{0.1875}\text{Sc}_{0.25}\text{Yb}_{0.1875}\text{Zr}_{0.1875}\text{Cl}_6$ (HE5). This introduces a certain variability in the radii (155-194 pm) and charge of the cations (3^+ for all except Zr, with 4^+), which could lead to the creation of favorable percolation paths due to lattice distortions^[30] and improve the diffusive properties of the electrolyte.

A second structure with only four substituents was also studied to corroborate the entropic origin of the possible enhancements. The physical principle behind the improved properties of high entropy

electrolytes is, justifiably, under question^[107]. Doubts are raised regarding whether these enhancements are in turn due to the selective addition of species. Therefore, we included in our study a third structure with only four substituents. We chose it to be $\text{Li}_{2.75}\text{Lu}_{0.25}\text{Sc}_{0.25}\text{Yb}_{0.25}\text{Zr}_{0.25}\text{Cl}_6$ (HE4).

In the following we present a comparison between all three configurations as obtained for the $2 \times 2 \times 2$ supercells. It must be noted that only 90ps were obtained for the NVT simulations of HE4, whereas 120ps are available for the pristine sample (LIC) and HE5. Due to the short timescales under consideration, this difference could impact the results. For consistency, results are shown for LIC and HE5 for the full 120ps, and for LIC, HE5 and HE4 restricted to the 90ps duration, so they can be compared directly. Moreover, the particular HE5 and HE4 used in this investigation were those with the lowest energies among the five options explained in Section 3.1.

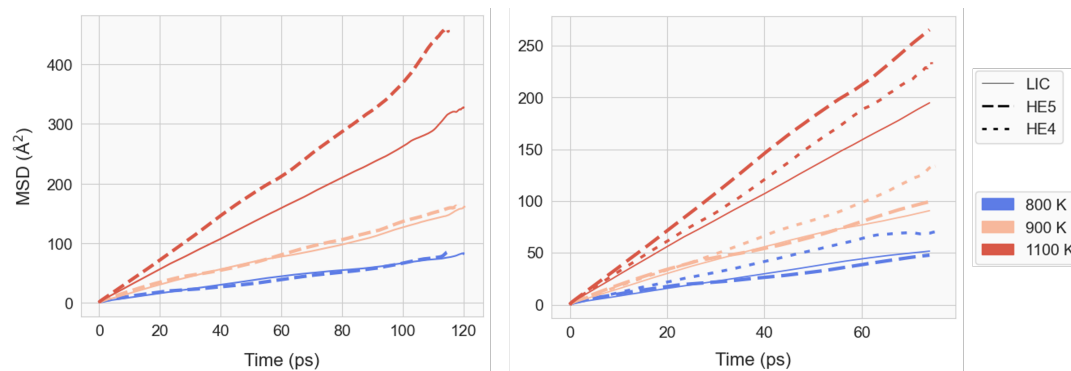


Figure 4.10: Left: MSD curves for the pristine structure (LIC, solid) and HE5 (dashed) at selected temperatures. **Right:** MSD curves at the same temperatures, also including HE4 (shorter dashes). Only shorter simulations for HE4 were obtained (90ps), hence different limits between the figures must be noted.

We found that HE4 outperforms the pristine structure by almost an order of magnitude in its conductivity at room temperature compared to the full length LIC simulation, whereas HE5 shows little to no improvement (Figure 4.10, Figure 4.11). In the 90ps comparison, LIC shows a quite higher conductivity than for 120ps. That is not outside the ordinary since due to the exponential relation between activation energy and conductivity, expected ranges of conductivity at room temperature are quite high. Moreover, LIC presents large errorbars for 90 ps, which leads to doubt this result. On the other hand, HE4 has lower smaller errorbars, comparable to those for the long simulation times of LIC and HE5, and even better. This is probably due to the higher kinetics just providing better statistics. Therefore, we consider the conclusion that HE4 is more conductive and reliable.

Indeed, HE4 lowers the energy barrier considerably in all dimensions and layers, as per Figure 4.12. This challenges expectations about high entropy effects. A similar study from 2024 also reported moderate improvement in ionic conductivity in a HE-LIC with Y, Yb, Er, In and Zr^[33]. However, their three-element substitution (Y, In and Zr) did not show as distinctive behavior as our HE4, and instead seemed to back the high entropy hypothesis. The opposite is deduced from our investigation.

Having negated the pure high entropy mechanism, two main features of HE4 that could impact its diffusive properties remain: reduced indium content and increased vacancy concentration from Zr substitution. An investigation of exactly this aliovalent substitution in LIC was carried out in [46]. For $\text{Li}_{3-x}\text{In}_{1-x}\text{Zr}_x\text{Cl}_6$ with $0 \leq x \leq 0.5$, the optimal concentration of lithium was found at $x_{\text{Li}} = 2.6$, nearly tripling the conductivity. In our case, HE4 displays a 6-fold increase in conductivity at $x_{\text{Li}} = 2.75$ whereas at $x_{\text{Li}} = 2.8125$ HE5 does not exhibit improvements. These results show similar trends and suggest that the introduction of vacancies could be responsible for the enhanced properties in HE4.

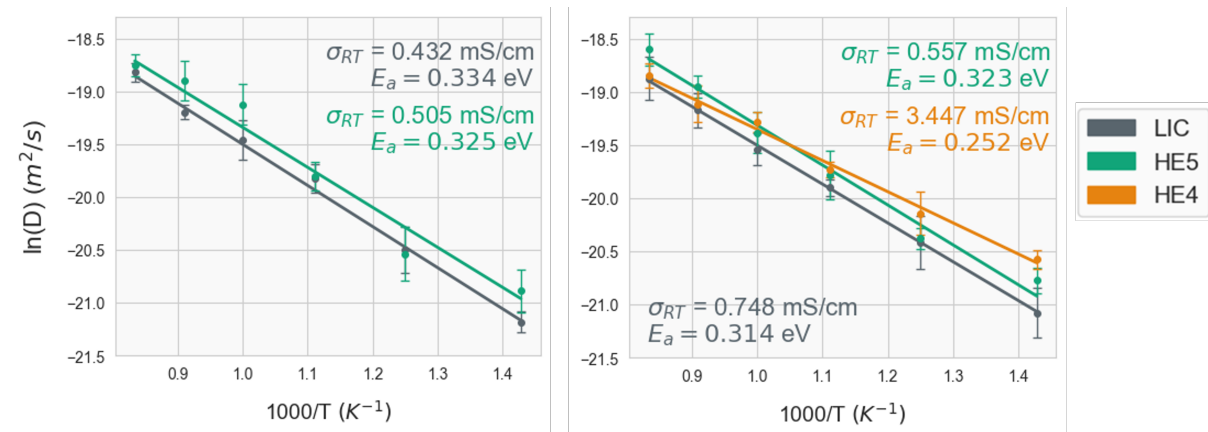


Figure 4.11: Arrhenius fits for LIC and HE5 (left), and including HE4 (right). Annotated, the conductivity at 300K (room temperature, RT) and the activation energy

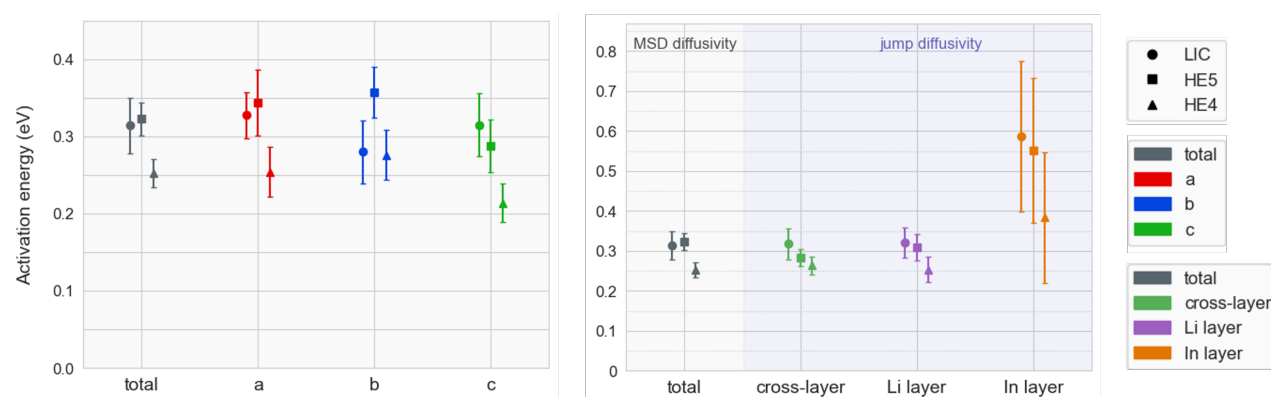


Figure 4.12: Dimensionality analysis of the three structures over 90ps. **Left** shows the diffusivity along each axis, while **right** shows it per layer. Figures for the full 120ps for LIC and HE5 were omitted as they show no changes. The label "In layer" is retained for simplicity despite now having a multi-cationic framework. Circle marker represents LIC, square represents HE5 and triangle represents HE4.

Finally, we studied the distribution of the distribution of lithium among the crystallographic sites and found comparable occupations for the pristine and the five-element structures, whereas the previously called indium layer is less occupied for HE4 (Figure 4.13, top left). In this case, slightly less lithium is captured throughout the three sites, and the allocation between the layers becomes more equitable.

Lithium specifically occupies more the site 2c in HE4. However, per the density distribution plots (Figure 4.13, bottom left), the site does not trap the ions. The concentration of lithium remains low around them but more connected. In the plane ab (Figure 4.13, right) more channels are open for lithium along a in HE4, and lower concentration of lithium is seen around specific sites than in its two counterparts. LIC and HE5 show extremely comparable distributions albeit a timid preference for the a direction. Although faint, due to the short simulation times and the relative scale of the plots, these changes in the observed mobility of lithium in HE4 make for a much better connectivity in the material and easy movement of charge across the electrolyte, as obviously demonstrated by its activation barrier 0.252eV versus 0.3eV from LIC and HE5.

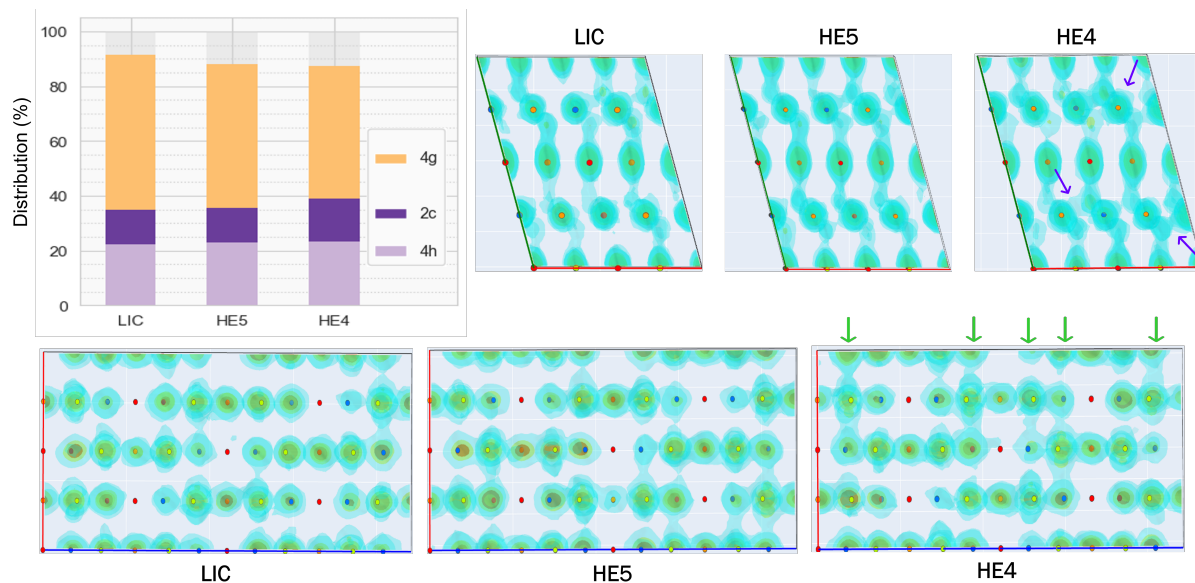


Figure 4.13: Top left: Lithium occupation distribution at 700K for the pristine structure, structure HE5 and structure HE4. **Bottom left, right:** Arrows indicate higher concentration around sites (left) or diffusion channels (right) present most relevantly in the high-entropy-4 configuration.

Overall, findings from the analysis of high entropy are insightful. They reveal that other factors can be behind improved properties in high entropy solid battery materials rather than the claimed configurational entropy. In this case, enhancement of conductivity due to the introduction of vacancies via substitution with Zr seems most probable.

4.3. Implementing machine learning trained potentials for solid electrolyte analysis

As already established, machine learning trained potentials promise to enable many key features for computational materials research, especially for solid battery materials. Here we present the first steps towards implementing these methods in the research group.

First, the performance of the pretrained *universal* CHGNet model is presented, compared with the performance of fine tuned model trained as per Section 3.2.1, and taking the DFT simulations as reference. Consequently, we evaluate how well the MLTP represents the diffusion phenomena found in Li_3InCl_6 , and finally we test some of the premises that make machine learning trained potentials attractive. We present 1ns-long and low-temperature simulations as an example.

4.3.1. To fine tune or not to fine tune

Given the large training set of the pretrained model of CHGNet (PT), the model was introduced as universal. Nonetheless, as can be seen in Figure 4.14, the original model is far from accurate for our Li_3InCl_6 . Further refinement of CHGNet-PT is necessary to use it in our investigation. Without it, in

the NVT-MD at 700K the structure decomposes and the lattice is no longer existent. The fine tuned model, however, mimicked remarkably well the displacement curves shown in that figure, which was compared as a preliminary test.

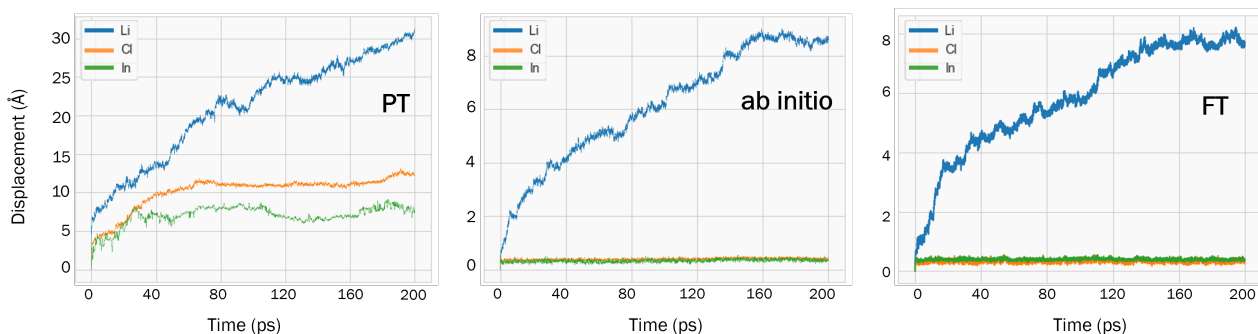


Figure 4.14: NVT simulations of the 212-ordered structure at 700K using the pretrained CHGNet model (PT), the previous ab initio results and the fine tuned CHGNet model (FT).

The fine tuned model achieved satisfactory metrics in its training, with 3 meV/atom in the energy, 50 meV/Å in the force and 0.052 GPa for the stress. These values are sensible for CHGNet but slightly higher than reported in cases where fine tuned CHGNet models were used^[28, 97]. The generalization error was null, unsurprisingly given the small test set (explained in Section 3.2.1). For that reason, the model was manually tested on the static and NPT relaxations of structures O and OHC (Section 3.1), yielding excellent results when compared with ab initio as shown in Figure 4.15. The NPT-MD was carried out with the same settings as NVT (Section 3.2), and using the Langevin barostat for VASP and the Nosé-Hoover barostat for LAMMPS.

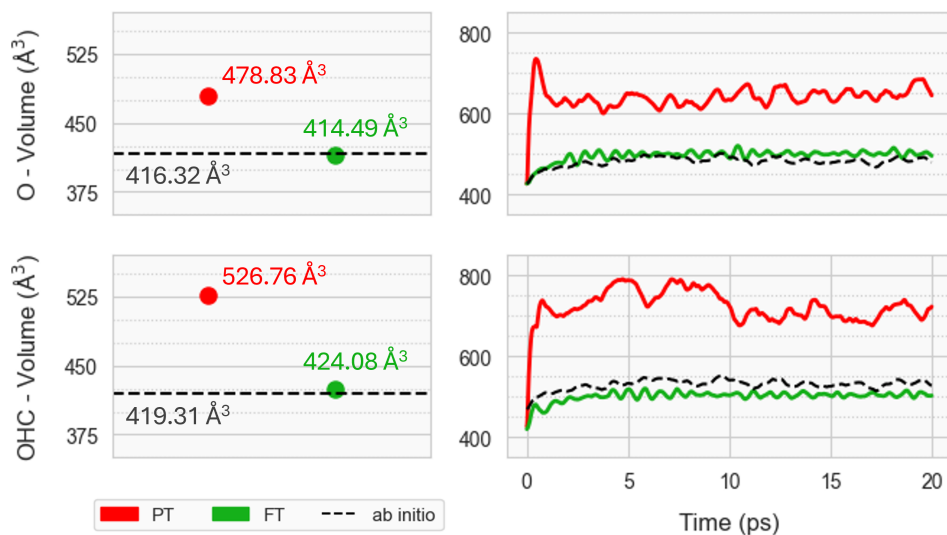


Figure 4.15: **Top:** Performance of the pretrained and fine tuned models of CHGNet in relaxing the structures 2x1x2-O (top row) and 2x1x2-OHC (bottom row). **Left:** static relaxations. **Right:** NPT relaxations at 300K.

The agreement is practically perfect for the static relaxations (Figure 4.15 left), and the improvement with respect to the pretrained model is even more striking for the NPT case. This suggests that the

fine tuning was of high quality, as it correctly predicted the evolution of a system under conditions far from the training data.

Therefore, whereas the pretrained model failed to represent the physical interactions in our system, the FT model reproduced correctly the volume of the structures and the initial NVT simulation. Herein we present further analysis of the electrolyte using the fine tuned MLTP, focusing on the simulation of its diffusive properties.

4.3.2. Reproducibility of ab initio results

Once established that the FT model provides good baseline results for Li_3InCl_6 in its two tested configurations, $2\times 1\times 2\text{-O}$ (O from now on) and $2\times 1\times 2\text{-OHC}$ (OHC), we include the $2\times 2\times 2\text{-O}$ structure. $2\times 2\times 2\text{-O}$ is the same structure as O but doubled along b . It was referred to as the pristine structure in Section 4.2 and hereafter referred to as $2\times 2\times 2$.

To further corroborate the ability of the FT-MLTP to simulate ionic diffusion in LIC, we studied the MSDs and associated activation energies for the three structures, and compared them with their ab initio counterparts. To ensure a fair comparison, the simulation settings were kept as consistent as possible: simulations spanned 200ps for O and OHC at 550K, 700K-1000K and 120ps for $2\times 2\times 2$ at 700K-1200K. The lithium distribution for each of the structures was also inherited from the ab initio investigation.

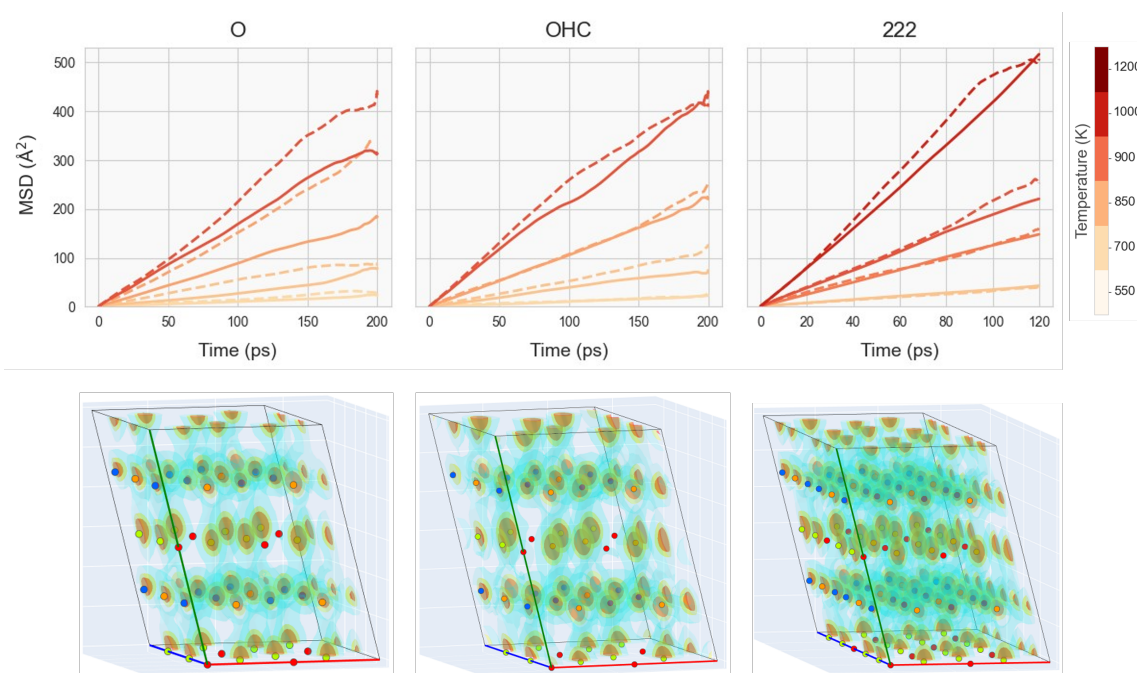


Figure 4.16: Top: MSD curves for the three structures at selected temperatures (550K, 700K, 850K and 1000K for O and OHC; 700K, 900K, 1000K and 1200K for 222). Solid lines represent the FT trajectories and the dashed lines are the corresponding ab initio ones. **Bottom:** Lithium density probability for each of the structures at 1000K.

The FT model provides reasonable results that can be observed in Figure 4.16. The MSD curves grow linearly and are sensitive to temperature increases, while the lithium density distributions and diffusion paths are analogous to the ab initio simulations. Furthermore, the disordered structure OHC also presented small indium movements like observed in Section 4.1.1. The high accordance

of results for the 2x2x2 supercell is especially encouraging, since the training set for FT was only made up of 2x1x2 supercells. This suggests that smaller systems could provide sufficient training for simulating large systems with the FT-MLTP.

Some deviations from the ab initio reference can be seen in the MSD curves of structure O at high temperature (Figure 4.16, top left), and most importantly from the activation energies in Figure 4.17. The fits for both structures O and OHC are notably different from the ab initio ones, although interestingly structure O still shows lower activation energy than the disordered OHC. However, considering the large errorbars, which include the ab initio values, we cannot pass a judgement too strict on these results.

Moreover, there is great accordance between FT and ab initio for 2x2x2, arguably the truest to the physics of the material given the improved statistics and larger system size. The simulations are therefore deemed generally satisfactory to the end of verifying the applicability of MLTPs in our study. They preserve the physical behavior of the system and exhibit the expected features of lithium transport in Li_3InCl_6 , even though exact reproducibility was not been achieved.

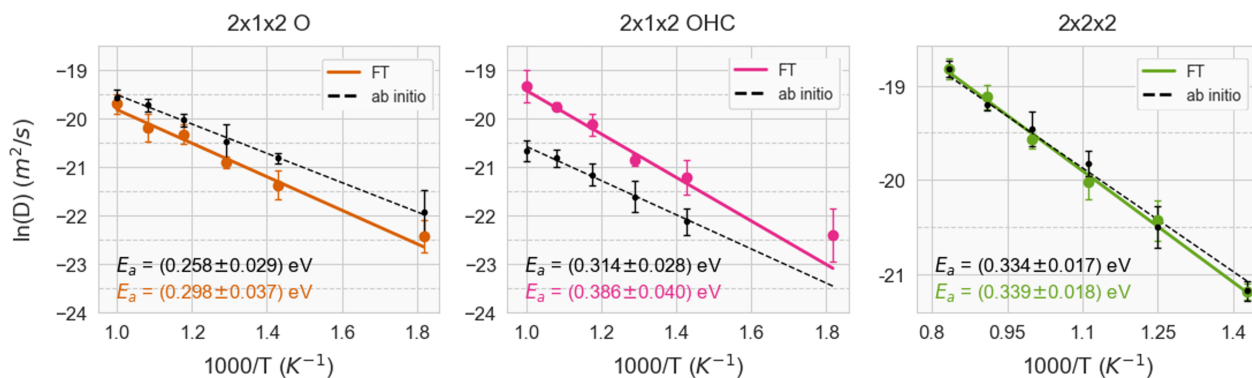


Figure 4.17: Arrhenius fits for FT (solid line) and ab initio (dashed line) NVTs for each structure.

This is especially true when considering the limited size of the training data, 30 times smaller than used by the creators of CHGNet in a similar study^[28], or the lack of intuition to choose the fine tuning hyperparameters. We consider this a successful first implementation of machine learning techniques into the computational research at the research group. Following studies using this method will undoubtedly benefit from the knowledge acquired during this first approach.

Finally, an illustration of the improvement in computational costs of MLTP-MDs versus ab initio MDs throughout this investigation is shown on Table 4.1. The lightness and scalability of machine learning trained potentials, when combined with the proper training and usage, has the potential to revolutionize the state of the art, if it is not doing so already.

	2x1x2	2x2x2
VASP	3,045.53	18,791.63
LAMMPS	66.00	138.80

Table 4.1: CPU hours required for 200 ps NVT simulations for 2x1x2 (structure O) and 2x2x2 supercells using an ab initio software (VASP) or the classical software with the MLTP implementation (LAMMPS). Illustrative data from simulations at 700K is shown.

4.3.3. Beyond the limits of ab initio

To conclude, we tested the FT-MLTP on two of its biggest attractions, namely the ability to perform simulations for long times and at lower temperatures. We experimented increasing the simulation times of the previous structures to 1 ns, and we also included an extra simulation at 300K. Figure 4.18 (top) shows the effect of longer simulation times in the Arrhenius study. At the bottom, the conductivity calculated from the simulation at 300K compared to the extrapolations from the high temperature simulations.

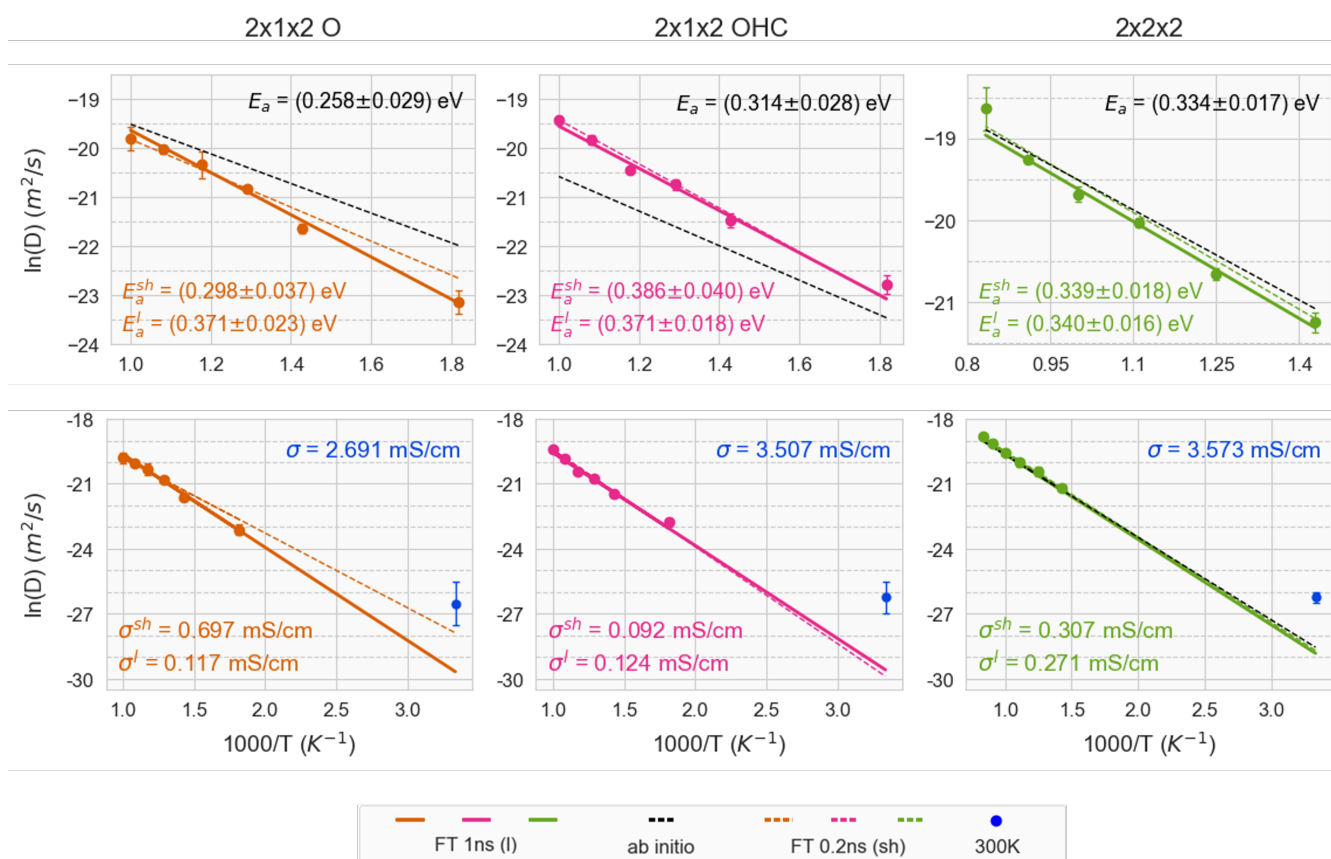


Figure 4.18: Arrhenius fits for the three structures showing data from the ab initio (dashed black) and FT simulations (color), for the short simulation times (dashed) and 1ns (solid). **Top:** Bounds are the simulation temperatures (550K to 1000K for 2x1x2 and 700-1200K for 2x2x2). **Bottom:** The plot is expanded to include $T=300\text{K}$, and the diffusivity directly calculated at that temperature

The longer simulations reduced the errorbars significantly, and in the case of O the calculated activation energy also suffered a major change (Figure 4.18 top). Under these conditions, its value matches perfectly the activation energy of OHC, which was also reduced slightly. However, both of them are still far from the ab initio results (colored representing the FT fits and black representing the ab initio ones) even considering the large errorbars. 2x2x2 remains essentially unchanged and in good alignment with the reference data, on the other hand, probably due to the already good statistics in the short simulations due to the large system size.

Notwithstanding the match in activation energies, the diffusivity calculated at 300K for 2x2x2 is also far from the extrapolated value from the high temperature simulations, just as for O and OHC. Interestingly, all three structures coincide in $\sigma \sim 2-4\text{mS/cm}$. Although minute details should not be deduced from our FT model, as previously noted, we have settled that the simulations do not seem unphysical. Therefore, it is likely that simulations around 300K would return a different slope than at high temperatures for all three structures. This finding highlights the importance of unlocking the ability to simulate materials close to their working temperatures.

This incursion into the range of possibilities offered by MLTPs, almost anecdotic, is a timid presentation of the reach of current-day computational techniques. We have shown two examples of how machine learning methods can surpass the limitations of ab initio, and We hope it will inspire further exploration in this area.

5

Conclusions

In this investigation we examined the diffusion properties of the promising halide solid electrolyte Li_3InCl_6 through computational analysis. Simultaneously, we sought to answer three questions: i) how and if cationic-site disorder affects them, ii) how and if high entropy affects them, and iii) how machine learning techniques can enhance the computational investigation of materials, specifically molecular dynamics simulations. We have found answers to all these questions.

First, we found that Li_3InCl_6 , which belongs to the $C2/m$ symmetry group, exhibits an activation energy for the diffusion of lithium of around 0.25-0.31 eV and ionic conductivity at room temperature between 0.2-0.8 mS/cm via a octahedral-tetrahedral-octahedral path. Moreover, through a study of the diffusion dimensionality, we found that there is no strongly preferred direction. Li_3InCl_6 presents isotropic three-dimensional diffusivity.

Throughout this study we compared the effect of cationic-site disorder of indium, and observed that the most ordered structure shows the highest conductivity. We created four structures disordered in the indium sublattice and compared them to the ordered structure to see what effects this could have on the transport of lithium. Despite creating quite dissimilar lattices, all the disordered structures showed similar properties and the ordered structure outperformed them all.

Next, we created a high entropy structure where the indium in Li_3InCl_6 was substituted by five elements (In, Lu, Sc, Yb and Zr) and another one with only four substituents, completely removing the indium. Our results contradict the high entropy claim that more is better. The five-element structure shows virtually no improvement over the pristine one, while the four-element configuration showed a 400% improvement in lithium diffusivity. We have defended that this is the effect of the introduction of vacancies, and not entropy.

Finally, we have implemented a machine learning trained potential into the computational research methods of the SEE group. We fine tuned the CHGNet artificial neural network to better represent our system, achieving a drastic improvement in the simulation of Li_3InCl_6 from the general pretrained model, and were able to analyze the diffusion mechanisms as usual. In this way, we established a pipeline for including machine learning trained potentials in the computational study of materials at

the group. As a closing note, we demonstrated the appeal of using machine learning in molecular dynamics experimenting beyond the limits of *ab initio*. We were able to perform nanosecond-long simulations and go to temperatures as low as 300K.

References

- [1] D. Price, “Energy and human evolution,” *Population and Environment*, vol. 16, no. 4, pp. 301–319, 1995, ISSN: 0199-0039. [Online]. Available: <https://www.jstor.org/stable/27503404>.
- [2] R. A. Fessenden, *System of storing power*, Nov. 1917. [Online]. Available: <https://patents.google.com/patent/US1247520A/en>.
- [3] V. Eyring, V. Mishra, G. P. Griffith, *et al.*, “Reflections and projections on a decade of climate science,” en, *Nature Climate Change*, vol. 11, no. 4, pp. 279–285, Apr. 2021, ISSN: 1758-678X, 1758-6798. DOI: 10.1038/s41558-021-01020-x. [Online]. Available: <https://www.nature.com/articles/s41558-021-01020-x>.
- [4] Y. Sekerci and S. Petrovskii, “Mathematical modelling of plankton–oxygen dynamics under the climate change,” en, *Bulletin of Mathematical Biology*, vol. 77, no. 12, pp. 2325–2353, Dec. 2015, ISSN: 0092-8240, 1522-9602. DOI: 10.1007/s11538-015-0126-0. [Online]. Available: <http://link.springer.com/10.1007/s11538-015-0126-0>.
- [5] G. Limpens and H. Jeanmart, “Electricity storage needs for the energy transition: An eroi based analysis illustrated by the case of belgium,” en, *Energy*, vol. 152, pp. 960–973, Jun. 2018, ISSN: 03605442. DOI: 10.1016/j.energy.2018.03.180. [Online]. Available: <https://linkinghub.elsevier.com/retrieve/pii/S0360544218305899>.
- [6] D. Heide, L. Von Bremen, M. Greiner, C. Hoffmann, M. Speckmann, and S. Bofinger, “Seasonal optimal mix of wind and solar power in a future, highly renewable europe,” en, *Renewable Energy*, vol. 35, no. 11, pp. 2483–2489, Nov. 2010, ISSN: 09601481. DOI: 10.1016/j.renene.2010.03.012. [Online]. Available: <https://linkinghub.elsevier.com/retrieve/pii/S0960148110001291>.
- [7] D. Heide, M. Greiner, L. von Bremen, and C. Hoffmann, “Reduced storage and balancing needs in a fully renewable european power system with excess wind and solar power generation,” *Renewable Energy*, vol. 36, no. 9, pp. 2515–2523, Sep. 2011, ISSN: 0960-1481. DOI: 10.1016/j.renene.2011.02.009. [Online]. Available: <https://www.sciencedirect.com/science/article/pii/S0960148111000851>.
- [8] G. Plessmann, M. Erdmann, M. Hlusiak, and C. Breyer, “Global energy storage demand for a 100% renewable electricity supply,” *Energy Procedia*, 8th International Renewable Energy Storage Conference and Exhibition (IRES 2013), vol. 46, pp. 22–31, Jan. 2014, ISSN: 1876-6102. DOI: 10.1016/j.egypro.2014.01.154. [Online]. Available: <https://www.sciencedirect.com/science/article/pii/S1876610214001702>.
- [9] en. [Online]. Available: https://ec.europa.eu/eurostat/statistics-explained/index.php?title=Passenger_cars_in_the_EU.

- [10] M. Mohsin, Q. Abbas, J. Zhang, M. Ikram, and N. Iqbal, "Integrated effect of energy consumption, economic development, and population growth on co2 based environmental degradation: A case of transport sector," eng, *Environmental Science and Pollution Research International*, vol. 26, no. 32, pp. 32 824–32 835, Nov. 2019, ISSN: 1614-7499. DOI: 10.1007/s11356-019-06372-8.
- [11] Q. Zhao, S. Stalin, C.-Z. Zhao, and L. A. Archer, "Designing solid-state electrolytes for safe, energy-dense batteries," en, *Nature Reviews Materials*, vol. 5, no. 3, pp. 229–252, Mar. 2020, ISSN: 2058-8437. DOI: 10.1038/s41578-019-0165-5. [Online]. Available: <https://www.nature.com/articles/s41578-019-0165-5>.
- [12] S. Zhang, J. Ma, S. Dong, and G. Cui, "Designing all-solid-state batteries by theoretical computation: A review," en, *Electrochemical Energy Reviews*, vol. 6, no. 1, p. 4, Feb. 2023, ISSN: 2520-8136. DOI: 10.1007/s41918-022-00143-9. [Online]. Available: <https://doi.org/10.1007/s41918-022-00143-9>.
- [13] T. Famprikis, P. Canepa, J. A. Dawson, M. S. Islam, and C. Masquelier, "Fundamentals of inorganic solid-state electrolytes for batteries," en, *Nature Materials*, vol. 18, no. 12, pp. 1278–1291, Dec. 2019, ISSN: 1476-1122, 1476-4660. DOI: 10.1038/s41563-019-0431-3. [Online]. Available: <https://www.nature.com/articles/s41563-019-0431-3>.
- [14] C. Wang and X. Sun, "The promise of solid-state batteries for safe and reliable energy storage," *Engineering*, vol. 21, pp. 32–35, Feb. 2023, ISSN: 2095-8099. DOI: 10.1016/j.eng.2022.10.008. [Online]. Available: <https://www.sciencedirect.com/science/article/pii/S2095809922007664>.
- [15] J. Janek and W. G. Zeier, "Challenges in speeding up solid-state battery development," en, *Nature Energy*, vol. 8, no. 3, pp. 230–240, Mar. 2023, ISSN: 2058-7546. DOI: 10.1038/s41560-023-01208-9. [Online]. Available: <https://www.nature.com/articles/s41560-023-01208-9>.
- [16] K. Tuo, C. Sun, and S. Liu, "Recent progress in and perspectives on emerging halide superionic conductors for all-solid-state batteries," *Electrochemical Energy Reviews*, vol. 6, no. 1, pp. 1–46, Dec. 2023, ISSN: 2520-8136. DOI: 10.1007/s41918-023-00179-5. [Online]. Available: <https://link.springer.com/article/10.1007/s41918-023-00179-5>.
- [17] J. Kendall, E. D. Crittenden, and H. K. Miller, "A study of the factors influencing compound formation and solubility in fused salt mixtures 1," en, *Journal of the American Chemical Society*, vol. 45, no. 4, pp. 963–996, Apr. 1923, ISSN: 0002-7863, 1520-5126. DOI: 10.1021/ja01657a015. [Online]. Available: <https://pubs.acs.org/doi/abs/10.1021/ja01657a015>.
- [18] D. C. Ginnings and T. E. Phipps, "Temperature-conductance curves of solid salts. iii. halides of lithium," en, *Journal of the American Chemical Society*, vol. 52, no. 4, pp. 1340–1345, Apr. 1930, ISSN: 0002-7863, 1520-5126. DOI: 10.1021/ja01367a006. [Online]. Available: <https://pubs.acs.org/doi/abs/10.1021/ja01367a006>.
- [19] "Solid halide electrolytes with high lithium-ion conductivity for application in 4 v class bulk-type all-solid-state batteries," en, vol. 30, p. 1 803 075, Nov. 2018, ISSN: 0935-9648, 1521-4095. DOI: 10.1002/adma.201803075. [Online]. Available: <https://onlinelibrary.wiley.com/doi/10.1002/adma.201803075>.
- [20] H. Kwak, S. Wang, J. Park, *et al.*, "Emerging halide superionic conductors for all-solid-state batteries: Design, synthesis, and practical applications," en, *ACS Energy Letters*, vol. 7, no. 5, pp. 1776–1805, May 2022, ISSN: 2380-8195, 2380-8195. DOI: 10.1021/acsenenergylett.2c00438. [Online]. Available: <https://pubs.acs.org/doi/10.1021/acsenenergylett.2c00438>.

- [21] L. Zhou, T.-T. Zuo, C. Y. Kwok, *et al.*, “High areal capacity, long cycle life 4 v ceramic all-solid-state li-ion batteries enabled by chloride solid electrolytes,” en, *Nature Energy*, vol. 7, no. 1, pp. 83–93, Jan. 2022, ISSN: 2058-7546. DOI: 10.1038/s41560-021-00952-0. [Online]. Available: <https://www.nature.com/articles/s41560-021-00952-0>.
- [22] Y. Han, S. H. Jung, H. Kwak, *et al.*, “Single- or poly-crystalline ni-rich layered cathode, sulfide or halide solid electrolyte: Which will be the winners for all-solid-state batteries?” en, *Advanced Energy Materials*, vol. 11, no. 21, p. 2100126, Jun. 2021, ISSN: 1614-6832, 1614-6840. DOI: 10.1002/aenm.202100126. [Online]. Available: <https://onlinelibrary.wiley.com/doi/10.1002/aenm.202100126>.
- [23] X. Li, J. Liang, J. Luo, *et al.*, “Air-stable li₃incl₆ electrolyte with high voltage compatibility for all-solid-state batteries,” en, *Energy & Environmental Science*, vol. 12, no. 9, pp. 2665–2671, Sep. 2019, ISSN: 1754-5706. DOI: 10.1039/C9EE02311A. [Online]. Available: <https://pubs.rsc.org/en/content/articlelanding/2019/ee/c9ee02311a>.
- [24] X. Li, J. Liang, N. Chen, *et al.*, “Water-mediated synthesis of a superionic halide solid electrolyte,” en, *Angewandte Chemie International Edition*, vol. 58, no. 46, pp. 16427–16432, Nov. 2019, ISSN: 1433-7851, 1521-3773. DOI: 10.1002/anie.201909805. [Online]. Available: <https://onlinelibrary.wiley.com/doi/10.1002/anie.201909805>.
- [25] S. Wang, Q. Bai, A. M. Nolan, *et al.*, “Lithium chlorides and bromides as promising solid-state chemistries for fast ion conductors with good electrochemical stability,” en, *Angewandte Chemie*, vol. 131, no. 24, pp. 8123–8127, Jun. 2019, ISSN: 0044-8249, 1521-3757. DOI: 10.1002/ange.201901938. [Online]. Available: <https://onlinelibrary.wiley.com/doi/10.1002/ange.201901938>.
- [26] R. Schlem, S. Muy, N. Prinz, *et al.*, “Mechanochemical synthesis: A tool to tune cation site disorder and ionic transport properties of li₃mcl₆ (m = y, er) superionic conductors,” en, *Advanced Energy Materials*, vol. 10, no. 6, p. 1903719, Feb. 2020, ISSN: 1614-6832, 1614-6840. DOI: 10.1002/aenm.201903719. [Online]. Available: <https://onlinelibrary.wiley.com/doi/10.1002/aenm.201903719>.
- [27] P. Molaiyan, S. E. Mailhot, K. Voges, *et al.*, “Investigation of the structure and ionic conductivity of a li₃incl₆ modified by dry room annealing for solid-state li-ion battery applications,” en, *Materials & Design*, vol. 227, p. 111690, Mar. 2023, ISSN: 02641275. DOI: 10.1016/j.matdes.2023.111690. [Online]. Available: <https://linkinghub.elsevier.com/retrieve/pii/S0264127523001053>.
- [28] P. Zhong, S. Gupta, B. Deng, K. Jun, and G. Ceder, “Effect of cation disorder on lithium transport in halide superionic conductors,” en, *ACS Energy Letters*, pp. 2775–2781, May 2024, ISSN: 2380-8195, 2380-8195. DOI: 10.1021/acsenergylett.4c00799. [Online]. Available: <https://pubs.acs.org/doi/10.1021/acsenergylett.4c00799>.
- [29] C. Oses, C. Toher, and S. Curtarolo, “High-entropy ceramics,” en, *Nature Reviews Materials*, vol. 5, no. 4, pp. 295–309, Apr. 2020, ISSN: 2058-8437. DOI: 10.1038/s41578-019-0170-8. [Online]. Available: <https://www.nature.com/articles/s41578-019-0170-8>.
- [30] Y. Zeng, B. Ouyang, J. Liu, *et al.*, “High-entropy mechanism to boost ionic conductivity,” en, *Science*, vol. 378, no. 6626, pp. 1320–1324, Dec. 2022, ISSN: 0036-8075, 1095-9203. DOI: 10.1126/science.abq1346. [Online]. Available: <https://www.science.org/doi/10.1126/science.abq1346>.
- [31] Y. Li, S. Song, H. Kim, *et al.*, “A lithium superionic conductor for millimeter-thick battery electrode,” *Science*, vol. 381, no. 6653, pp. 50–53, 2023. DOI: 10.1126/science.add7138. eprint: <https://www.science.org/doi/pdf/10.1126/science.add7138>. [Online]. Available: <https://www.science.org/doi/abs/10.1126/science.add7138>.

- [32] F. Strauss, J. Lin, M. Duffiet, *et al.*, “High-entropy polyanionic lithium superionic conductors,” *ACS Materials Letters*, vol. 4, no. 2, pp. 418–423, 2022. DOI: 10.1021/acsmaterialslett.1c00817. [Online]. Available: <https://doi.org/10.1021/acsmaterialslett.1c00817>.
- [33] Z. Song, T. Wang, H. Yang, *et al.*, “Promoting high-voltage stability through local lattice distortion of halide solid electrolytes,” en, *Nature Communications*, vol. 15, no. 1, p. 1481, Feb. 2024, ISSN: 2041-1723. DOI: 10.1038/s41467-024-45864-1. [Online]. Available: <https://www.nature.com/articles/s41467-024-45864-1>.
- [34] A. Urban, D.-H. Seo, and G. Ceder, “Computational understanding of li-ion batteries,” en, *npj Computational Materials*, vol. 2, no. 1, pp. 1–13, Mar. 2016, ISSN: 2057-3960. DOI: 10.1038/npjcompumats.2016.2. [Online]. Available: <https://www.nature.com/articles/npjcompumats20162>.
- [35] A. Urban, D.-H. Seo, and G. Ceder, “Computational understanding of li-ion batteries,” en, *npj Computational Materials*, vol. 2, no. 1, pp. 1–13, Mar. 2016, ISSN: 2057-3960. DOI: 10.1038/npjcompumats.2016.2. [Online]. Available: <https://www.nature.com/articles/npjcompumats20162>.
- [36] X. He, Y. Zhu, A. Epstein, and Y. Mo, “Statistical variances of diffusional properties from ab initio molecular dynamics simulations,” en, *npj Computational Materials*, vol. 4, no. 1, pp. 1–9, Apr. 2018, ISSN: 2057-3960. DOI: 10.1038/s41524-018-0074-y. [Online]. Available: <https://www.nature.com/articles/s41524-018-0074-y>.
- [37] P. Friederich, F. Häse, J. Proppe, and A. Aspuru-Guzik, “Machine-learned potentials for next-generation matter simulations,” en, *Nature Materials*, vol. 20, no. 6, pp. 750–761, Jun. 2021, ISSN: 1476-4660. DOI: 10.1038/s41563-020-0777-6. [Online]. Available: <https://www.nature.com/articles/s41563-020-0777-6>.
- [38] W. Jia, H. Wang, M. Chen, *et al.*, “Pushing the limit of molecular dynamics with ab initio accuracy to 100 million atoms with machine learning,” in *SC20: International Conference for High Performance Computing, Networking, Storage and Analysis*, Nov. 2020, pp. 1–14. DOI: 10.1109/SC41405.2020.00009. [Online]. Available: <https://ieeexplore.ieee.org/document/9355242>.
- [39] [Online]. Available: https://docs.lammps.org/Speed_bench.html.
- [40] A. P. Bartók, M. C. Payne, R. Kondor, and G. Csányi, “Gaussian approximation potentials: The accuracy of quantum mechanics, without the electrons,” en, *Physical Review Letters*, vol. 104, no. 13, p. 136403, Apr. 2010, ISSN: 0031-9007, 1079-7114. DOI: 10.1103/PhysRevLett.104.136403. [Online]. Available: <https://link.aps.org/doi/10.1103/PhysRevLett.104.136403>.
- [41] S.-P. Chen, D. Lv, J. Chen, Y.-H. Zhang, and F.-N. Shi, “Review on defects and modification methods of lifepo 4 cathode material for lithium-ion batteries,” en, *Energy & Fuels*, vol. 36, no. 3, pp. 1232–1251, Feb. 2022, ISSN: 0887-0624, 1520-5029. DOI: 10.1021/acs.energyfuels.1c03757. [Online]. Available: <https://pubs.acs.org/doi/10.1021/acs.energyfuels.1c03757>.
- [42] Z. Ahsan, B. Ding, Z. Cai, *et al.*, “Recent progress in capacity enhancement of lifepo4 cathode for li-ion batteries,” en, *Journal of Electrochemical Energy Conversion and Storage*, vol. 18, no. 1, p. 010801, Feb. 2021, ISSN: 2381-6872, 2381-6910. DOI: 10.1115/1.4047222. [Online]. Available: <https://asmedigitalcollection.asme.org/electrochemical/article/doi/10.1115/1.4047222/1083876/Recent-Progress-in-Capacity-Enhancement-of-LiFePO4>.
- [43] K. Steven W., *Machine Learning: a Concise Introduction*. Wiley, 2018, ISBN: 978-1-119-43919-6.

- [44] H. Mehrer, *Diffusion in solids: fundamentals, methods, materials, diffusion-controlled processes* (Springer series in solid state science). Berlin; New York: Springer, 2007, ISBN: 9783540714866.
- [45] M. Yamagishi, S. Tachibana, T. Shimizu, K. Mitsuhashi, and Y. Orikasa, “Analyzing sulfur-doped Li_3InCl_6 solid electrolytes by x-ray absorptin spectroscopy,” 2021.
- [46] B. Helm, R. Schlem, B. Wankmiller, *et al.*, “Exploring aliovalent substitutions in the lithium halide superionic conductor $\text{Li}_{3-x}\text{Zr}_x\text{Cl}_6$ ($0 \leq x \leq 0.5$),” *en, Chemistry of Materials*, vol. 33, no. 12, pp. 4773–4782, Jun. 2021, ISSN: 0897-4756, 1520-5002. DOI: 10.1021/acs.chemmater.1c01348. [Online]. Available: <https://pubs.acs.org/doi/10.1021/acs.chemmater.1c01348>.
- [47] E. Kim and Y. Kim, “Investigation of the effect of point defects on the Li-ion conductivity of Li_3InCl_6 ,” *en, Dalton Transactions*, vol. 51, no. 47, pp. 18159–18168, Dec. 2022, ISSN: 1477-9234. DOI: 10.1039/D2DT02943J. [Online]. Available: <https://pubs.rsc.org/en/content/articlelanding/2022/dt/d2dt02943j>.
- [48] S. Wang, Q. Bai, A. M. Nolan, *et al.*, “Lithium chlorides and bromides as promising solid-state chemistries for fast ion conductors with good electrochemical stability,” *en, Angewandte Chemie International Edition*, vol. 58, no. 24, pp. 8039–8043, Jun. 2019, ISSN: 1433-7851, 1521-3773. DOI: 10.1002/anie.201901938. [Online]. Available: <https://onlinelibrary.wiley.com/doi/10.1002/anie.201901938>.
- [49] B. Ouyang and Y. Zeng, “The rise of high-entropy battery materials,” *en, Nature Communications*, vol. 15, no. 1, p. 973, Feb. 2024, ISSN: 2041-1723. DOI: 10.1038/s41467-024-45309-9. [Online]. Available: <https://www.nature.com/articles/s41467-024-45309-9>.
- [50] J. Lin, G. Cherkashinin, M. Schäfer, *et al.*, “A high-entropy multicationic substituted lithium argyrodite superionic solid electrolyte,” *en, ACS Materials Letters*, vol. 4, no. 11, pp. 2187–2194, Nov. 2022, ISSN: 2639-4979, 2639-4979. DOI: 10.1021/acsmaterialslett.2c00667. [Online]. Available: <https://pubs.acs.org/doi/10.1021/acsmaterialslett.2c00667>.
- [51] *en*. [Online]. Available: <https://link.springer.com/book/10.1007/978-3-030-80359-9>.
- [52] J. C. Slater, “Atomic radii in crystals,” *en, The Journal of Chemical Physics*, vol. 41, no. 10, pp. 3199–3204, Nov. 1964, ISSN: 0021-9606, 1089-7690. DOI: 10.1063/1.1725697. [Online]. Available: <https://pubs.aip.org/jcp/article/41/10/3199/352896/Atomic-Radii-in-Crystals>.
- [53] D. S. Sholl and J. A. Steckel, *Density Functional Theory: A Practical Introduction*, *en*, 1st ed. Wiley, Mar. 2009, ISBN: 9780470373170. DOI: 10.1002/9780470447710. [Online]. Available: <https://onlinelibrary.wiley.com/doi/book/10.1002/9780470447710>.
- [54] J. Thijssen, *Computational Physics*, 2nd ed. Cambridge University Press, Mar. 2007, ISBN: 9780521833462. DOI: 10.1017/CB09781139171397. [Online]. Available: <https://www.cambridge.org/core/product/identifier/9781139171397/type/book>.
- [55] P. Hohenberg and W. Kohn, “Inhomogeneous electron gas,” *Physical Review*, vol. 136, no. 3B, B864–B871, Nov. 1964. DOI: 10.1103/PhysRev.136.B864. [Online]. Available: <https://link.aps.org/doi/10.1103/PhysRev.136.B864>.
- [56] W. Kohn and L. J. Sham, “Self-consistent equations including exchange and correlation effects,” *Physical Review*, vol. 140, A1133–A1138, Nov. 1965. DOI: 10.1103/PhysRev.140.A1133. [Online]. Available: <https://link.aps.org/doi/10.1103/PhysRev.140.A1133>.
- [57] J. Behler and M. Parrinello, “Generalized neural-network representation of high-dimensional potential-energy surfaces,” *Physical Review Letters*, vol. 98, no. 14, p. 146401, Apr. 2007. DOI: 10.1103/PhysRevLett.98.146401. [Online]. Available: <https://link.aps.org/doi/10.1103/PhysRevLett.98.146401>.

- [58] H. Hellmann, “Einführung in die quantenchemie,” *Nature*, vol. 141, no. 3572, pp. 667–668, Apr. 1938, ISSN: 0028-0836, 1476-4687. DOI: 10.1038/141667a0. [Online]. Available: <https://www.nature.com/articles/141667a0>.
- [59] R. P. Feynman, “Forces in molecules,” en, *Physical Review*, vol. 56, no. 4, pp. 340–343, Aug. 1939, ISSN: 0031-899X. DOI: 10.1103/PhysRev.56.340. [Online]. Available: <https://link.aps.org/doi/10.1103/PhysRev.56.340>.
- [60] B. Smit, “Understanding molecular simulation: From algorithm to applications,” [Online]. Available: https://www.academia.edu/13666033/Understanding_Molecular_Simulation_From_Algorithm_to_Applications.
- [61] V. Eyert, J. Wormald, W. A. Curtin, and E. Wimmer, “Machine-learned interatomic potentials: Recent developments and prospective applications,” en, *Journal of Materials Research*, vol. 38, no. 24, pp. 5079–5094, Dec. 2023, ISSN: 0884-2914, 2044-5326. DOI: 10.1557/s43578-023-01239-8. [Online]. Available: <https://link.springer.com/10.1557/s43578-023-01239-8>.
- [62] D. Marx and J. Hutter, *Ab Initio Molecular Dynamics: Basic Theory and Advanced Methods*, 1st ed. Cambridge University Press, Apr. 2009, ISBN: 9780521898638. DOI: 10.1017/CB09780511609633. [Online]. Available: <https://www.cambridge.org/core/product/identifier/9780511609633/type/book>.
- [63] V. I. Kalikmanov, “Ensembles in statistical mechanics,” in *Statistical Physics of Fluids*. Berlin, Heidelberg: Springer Berlin Heidelberg, 2001, pp. 1–27, ISBN: 9783642075117. DOI: 10.1007/978-3-662-04536-7_1. [Online]. Available: http://link.springer.com/10.1007/978-3-662-04536-7_1.
- [64] L. Verlet, “Computer “experiments” on classical fluids. i. thermodynamical properties of lennard-jones molecules,” *Physical Review*, vol. 159, no. 1, pp. 98–103, Jul. 1967. DOI: 10.1103/PhysRev.159.98. [Online]. Available: <https://link.aps.org/doi/10.1103/PhysRev.159.98>.
- [65] N. J. De Klerk, E. Van Der Maas, and M. Wagemaker, “Analysis of diffusion in solid-state electrolytes through md simulations, improvement of the li-ion conductivity in β -li 3 ps 4 as an example,” en, *ACS Applied Energy Materials*, vol. 1, no. 7, pp. 3230–3242, Jul. 2018, ISSN: 2574-0962, 2574-0962. DOI: 10.1021/acsaem.8b00457. [Online]. Available: <https://pubs.acs.org/doi/10.1021/acsaem.8b00457>.
- [66] D. Hebb, *The Organization of Behavior*, en, 0th ed. Psychology Press, Apr. 2005, ISBN: 9781410612403. DOI: 10.4324/9781410612403. [Online]. Available: <https://www.taylorfrancis.com/books/9781135631918>.
- [67] P. McKevitt, “Daniel crevier, ai: The tumultuous history of the search for artificial intelligence . london and new york: Basic books, 1993. isbn 0-465-02997-3.” en, *The British Journal for the History of Science*, vol. 30, no. 1, pp. 101–121, Mar. 1997, ISSN: 0007-0874, 1474-001X. DOI: 10.1017/S0007087496302963. [Online]. Available: https://www.cambridge.org/core/product/identifier/S0007087496302963/type/journal_article.
- [68] M. L. Jones, “Ai in history,” en, *The American Historical Review*, vol. 128, no. 3, pp. 1360–1367, Sep. 2023, ISSN: 0002-8762, 1937-5239. DOI: 10.1093/ahr/rhad361. [Online]. Available: <https://academic.oup.com/ahr/article/128/3/1360/7282241>.
- [69] H. Guo, Q. Wang, A. Stuke, A. Urban, and N. Artrith, “Accelerated atomistic modeling of solid-state battery materials with machine learning,” *Frontiers in Energy Research*, vol. 9, p. 695902, Jun. 2021, ISSN: 2296-598X. [Online]. Available: <https://www.frontiersin.org/articles/10.3389/fenrg.2021.695902/full>.

- [70] I. H. Sarker, “Machine learning: Algorithms, real-world applications and research directions,” en, *SN Computer Science*, vol. 2, no. 3, p. 160, May 2021, ISSN: 2662-995X, 2661-8907. DOI: 10.1007/s42979-021-00592-x. [Online]. Available: <https://link.springer.com/10.1007/s42979-021-00592-x>.
- [71] G. R. Schleder, A. C. M. Padilha, C. M. Acosta, M. Costa, and A. Fazzio, “From dft to machine learning: Recent approaches to materials science—a review,” *Journal of Physics: Materials*, vol. 2, no. 3, p. 032001, Jul. 2019, ISSN: 2515-7639. DOI: 10.1088/2515-7639/ab084b. [Online]. Available: <https://iopscience.iop.org/article/10.1088/2515-7639/ab084b>.
- [72] O. T. Unke, S. Chmiela, H. E. Sauceda, *et al.*, “Machine learning force fields,” en, *Chemical Reviews*, vol. 121, no. 16, pp. 10142–10186, Aug. 2021, ISSN: 0009-2665, 1520-6890. DOI: 10.1021/acs.chemrev.0c01111. [Online]. Available: <https://pubs.acs.org/doi/10.1021/acs.chemrev.0c01111>.
- [73] J. Behler, “Four generations of high-dimensional neural network potentials,” en, *Chemical Reviews*, vol. 121, no. 16, pp. 10037–10072, Aug. 2021, ISSN: 0009-2665, 1520-6890. DOI: 10.1021/acs.chemrev.0c00868. [Online]. Available: <https://pubs.acs.org/doi/10.1021/acs.chemrev.0c00868>.
- [74] en, Apr. 2017. [Online]. Available: <https://news.mit.edu/2017/explained-neural-networks-deep-learning-0414>.
- [75] A.-N. Sharkawy, “Principle of neural network and its main types: Review,” en, *Journal of Advances in Applied & Computational Mathematics*, vol. 7, pp. 8–19, Aug. 2020, ISSN: 2409-5761. DOI: 10.15377/2409-5761.2020.07.2. [Online]. Available: <https://www.avantipublishers.com/index.php/jaacm/article/view/851>.
- [76] Z. Wu, S. Pan, F. Chen, G. Long, C. Zhang, and P. S. Yu, “A comprehensive survey on graph neural networks,” *IEEE Transactions on Neural Networks and Learning Systems*, vol. 32, no. 1, pp. 4–24, Jan. 2021, arXiv:1901.00596 [cs, stat], ISSN: 2162-237X, 2162-2388. DOI: 10.1109/TNNLS.2020.2978386. [Online]. Available: <http://arxiv.org/abs/1901.00596>.
- [77] C. Chen, W. Ye, Y. Zuo, C. Zheng, and S. P. Ong, “Graph networks as a universal machine learning framework for molecules and crystals,” en, *Chemistry of Materials*, vol. 31, no. 9, pp. 3564–3572, May 2019, ISSN: 0897-4756, 1520-5002. DOI: 10.1021/acs.chemmater.9b01294. [Online]. Available: <https://pubs.acs.org/doi/10.1021/acs.chemmater.9b01294>.
- [78] P. V. Balachandran, J. Theiler, J. M. Rondinelli, and T. Lookman, “Materials prediction via classification learning,” en, *Scientific Reports*, vol. 5, no. 1, p. 13285, Aug. 2015, ISSN: 2045-2322. DOI: 10.1038/srep13285. [Online]. Available: <https://www.nature.com/articles/srep13285>.
- [79] S. Curtarolo, D. Morgan, K. Persson, J. Rodgers, and G. Ceder, “Predicting crystal structures with data mining of quantum calculations,” *Physical Review Letters*, vol. 91, no. 13, p. 135503, Sep. 2003. DOI: 10.1103/PhysRevLett.91.135503. [Online]. Available: <https://link.aps.org/doi/10.1103/PhysRevLett.91.135503>.
- [80] B. G. Sumpter and D. W. Noid, “Potential energy surfaces for macromolecules. a neural network technique,” en, *Chemical Physics Letters*, vol. 192, no. 5–6, pp. 455–462, May 1992, ISSN: 00092614. DOI: 10.1016/0009-2614(92)85498-Y. [Online]. Available: <https://linkinghub.elsevier.com/retrieve/pii/000926149285498Y>.
- [81] T. B. Blank, S. D. Brown, A. W. Calhoun, and D. J. Doren, “Neural network models of potential energy surfaces,” en, *The Journal of Chemical Physics*, vol. 103, no. 10, pp. 4129–4137, Sep. 1995, ISSN: 0021-9606, 1089-7690. DOI: 10.1063/1.469597. [Online]. Available: <https://pubs.aip.org/jcp/article/103/10/4129/481485/Neural-network-models-of-potential-energy-surfaces>.

- [82] J. Behler and M. Parrinello, “Generalized neural-network representation of high-dimensional potential-energy surfaces,” vol. 98, p. 146401, Apr. 2007. DOI: 10.1103/PhysRevLett.98.146401. [Online]. Available: <https://link.aps.org/doi/10.1103/PhysRevLett.98.146401>.
- [83] M. Eckhoff, F. Schönewald, M. Risch, C. A. Volkert, P. E. Blöchl, and J. Behler, “Closing the gap between theory and experiment for lithium manganese oxide spinels using a high-dimensional neural network potential,” en, *Physical Review B*, vol. 102, no. 17, p. 174102, Nov. 2020, ISSN: 2469-9950, 2469-9969. DOI: 10.1103/PhysRevB.102.174102. [Online]. Available: <https://link.aps.org/doi/10.1103/PhysRevB.102.174102>.
- [84] T. Thompson, J. Wolfenstine, J. L. Allen, *et al.*, “Tetragonal vs. cubic phase stability in al-free ta doped li₇la₃zr₂o₁₂ (llzo),” en, *J. Mater. Chem. A*, vol. 2, no. 33, pp. 13431–13436, 2014, ISSN: 2050-7488, 2050-7496. DOI: 10.1039/C4TA02099E. [Online]. Available: <https://xlink.rsc.org/?DOI=C4TA02099E>.
- [85] A. V. Shapeev, “Moment tensor potentials: A class of systematically improvable interatomic potentials,” en, *Multiscale Modeling & Simulation*, vol. 14, no. 3, pp. 1153–1173, Jan. 2016, ISSN: 1540-3459, 1540-3467. DOI: 10.1137/15M1054183. [Online]. Available: <http://epubs.siam.org/doi/10.1137/15M1054183>.
- [86] Z. Ahmad, T. Xie, C. Maheshwari, J. C. Grossman, and V. Viswanathan, “Machine learning enabled computational screening of inorganic solid electrolytes for suppression of dendrite formation in lithium metal anodes,” en, *ACS Central Science*, vol. 4, no. 8, pp. 996–1006, Aug. 2018, ISSN: 2374-7943, 2374-7951. DOI: 10.1021/acscentsci.8b00229. [Online]. Available: <https://pubs.acs.org/doi/10.1021/acscentsci.8b00229>.
- [87] A. R. Natarajan and A. Van Der Ven, “Machine-learning the configurational energy of multicomponent crystalline solids,” en, *npj Computational Materials*, vol. 4, no. 1, p. 56, Nov. 2018, ISSN: 2057-3960. DOI: 10.1038/s41524-018-0110-y. [Online]. Available: <https://www.nature.com/articles/s41524-018-0110-y>.
- [88] G. Houchins and V. Viswanathan, “An accurate machine-learning calculator for optimization of li-ion battery cathodes,” en, *The Journal of Chemical Physics*, vol. 153, p. 054124, Aug. 2020, ISSN: 0021-9606, 1089-7690. DOI: 10.1063/5.0015872. [Online]. Available: <https://pubs.aip.org/jcp/article/153/5/054124/1065685/An-accurate-machine-learning-calculator-for>.
- [89] T. Nishiyama, A. Seko, and I. Tanaka, “Application of machine learning potentials to predict grain boundary properties in fcc elemental metals,” en, *Physical Review Materials*, vol. 4, no. 12, p. 123607, Dec. 2020, ISSN: 2475-9953. DOI: 10.1103/PhysRevMaterials.4.123607. [Online]. Available: <https://link.aps.org/doi/10.1103/PhysRevMaterials.4.123607>.
- [90] N. Artrith, A. Urban, Y. Wang, and G. Ceder, “Atomic-scale factors that control the rate capability of nanostructured amorphous si for high-energy-density batteries,” 2019. DOI: 10.48550/ARXIV.1901.09272. [Online]. Available: <https://arxiv.org/abs/1901.09272>.
- [91] D. S. BIOVIA, *Materials studio*, San Diego: Dassault Systèmes, Version 2017, 2017.
- [92] K. Momma and F. Izumi, “Vesta 3 for three-dimensional visualization of crystal, volumetric and morphology data,” *Journal of Applied Crystallography*, vol. 44, no. 6, pp. 1272–1276, Dec. 2011, ISSN: 0021-8898. DOI: 10.1107/S0021889811038970. [Online]. Available: <https://scripts.iucr.org/cgi-bin/paper?S0021889811038970>.
- [93] T. K. Schwietert, V. A. Arszelewska, C. Wang, *et al.*, “Clarifying the relationship between redox activity and electrochemical stability in solid electrolytes,” en, *Nature Materials*, vol. 19, no. 4, pp. 428–435, Apr. 2020, ISSN: 1476-4660. DOI: 10.1038/s41563-019-0576-0. [Online]. Available: <https://www.nature.com/articles/s41563-019-0576-0>.

- [94] G. Kresse and J. Hafner, “Ab initio molecular dynamics for liquid metals,” *Physical Review B*, vol. 47, no. 1, pp. 558–561, Jan. 1993. DOI: 10.1103/PhysRevB.47.558. [Online]. Available: <https://link.aps.org/doi/10.1103/PhysRevB.47.558>.
- [95] P. E. Blöchl, “Projector augmented-wave method,” *Physical Review B*, vol. 50, no. 24, pp. 17 953–17 979, Dec. 1994. DOI: 10.1103/PhysRevB.50.17953. [Online]. Available: <https://link.aps.org/doi/10.1103/PhysRevB.50.17953>.
- [96] J. P. Perdew, A. Ruzsinszky, G. I. Csonka, *et al.*, “Restoring the density-gradient expansion for exchange in solids and surfaces,” *Physical Review Letters*, vol. 100, no. 13, p. 136 406, Apr. 2008. DOI: 10.1103/PhysRevLett.100.136406. [Online]. Available: <https://link.aps.org/doi/10.1103/PhysRevLett.100.136406>.
- [97] B. Deng, P. Zhong, K. Jun, *et al.*, “Chgnet as a pretrained universal neural network potential for charge-informed atomistic modelling,” en, *Nature Machine Intelligence*, vol. 5, no. 9, pp. 1031–1041, Sep. 2023, ISSN: 2522-5839. DOI: 10.1038/s42256-023-00716-3. [Online]. Available: <https://www.nature.com/articles/s42256-023-00716-3>.
- [98] A. P. Thompson, H. M. Aktulga, R. Berger, *et al.*, “Lammps - a flexible simulation tool for particle-based materials modeling at the atomic, meso, and continuum scales,” en, *Computer Physics Communications*, vol. 271, p. 108 171, Feb. 2022, ISSN: 00104655. DOI: 10.1016/j.cpc.2021.108171. [Online]. Available: <https://linkinghub.elsevier.com/retrieve/pii/S0010465521002836>.
- [99] V. Azizi, S. Smeets, A. K. Lavrinenko, and S. Ciarella, *Gemdat*, Feb. 2024. DOI: 10.5281/ZENODO.10683188. [Online]. Available: <https://zenodo.org/doi/10.5281/zenodo.10683188>.
- [100] S. P. Ong, W. D. Richards, A. Jain, *et al.*, “Python materials genomics (pymatgen): A robust, open-source python library for materials analysis,” en, *Computational Materials Science*, vol. 68, pp. 314–319, Feb. 2013, ISSN: 09270256. DOI: 10.1016/j.commatsci.2012.10.028. [Online]. Available: <https://linkinghub.elsevier.com/retrieve/pii/S0927025612006295>.
- [101] J. Pan, “Adding charge to neural network potentials,” en, *Nature Computational Science*, vol. 3, no. 10, pp. 816–816, Oct. 2023, ISSN: 2662-8457. DOI: 10.1038/s43588-023-00542-y. [Online]. Available: <https://www.nature.com/articles/s43588-023-00542-y>.
- [102] Z. Liu, S. Ma, J. Liu, S. Xiong, Y. Ma, and H. Chen, “High ionic conductivity achieved in li₃y(br₃cl₃) mixed halide solid electrolyte via promoted diffusion pathways and enhanced grain boundary,” en, *ACS Energy Letters*, vol. 6, no. 1, pp. 298–304, Jan. 2021, ISSN: 2380-8195, 2380-8195. DOI: 10.1021/acsenerylett.0c01690. [Online]. Available: <https://pubs.acs.org/doi/10.1021/acsenerylett.0c01690>.
- [103] T. Jeon and S. C. Jung, “High conductivity enabled by concerted li ion diffusion in li₃y(br₃cl₃) solid electrolytes for all-solid-state batteries,” en, *Journal of Materials Chemistry A*, vol. 11, no. 8, pp. 4334–4344, 2023, ISSN: 2050-7488, 2050-7496. DOI: 10.1039/D2TA09184D. [Online]. Available: <https://xlink.rsc.org/?DOI=D2TA09184D>.
- [104] D. Park, H. Park, Y. Lee, *et al.*, “Theoretical design of lithium chloride superionic conductors for all-solid-state high-voltage lithium-ion batteries,” eng, *ACS applied materials & interfaces*, vol. 12, no. 31, pp. 34 806–34 814, Aug. 2020, ISSN: 1944-8252. DOI: 10.1021/acsemi.0c07003.
- [105] Y. Kim and S. Choi, “Investigation of the effect of f-doping on the solid-electrolyte property of li₃incl₆,” *Journal of Power Sources*, vol. 567, p. 232 962, May 2023, ISSN: 0378-7753. DOI: 10.1016/j.jpowsour.2023.232962. [Online]. Available: <https://www.sciencedirect.com/science/article/pii/S0378775323003373>.

- [106] A. M. Nolan, Y. Zhu, X. He, Q. Bai, and Y. Mo, “Computation-accelerated design of materials and interfaces for all-solid-state lithium-ion batteries,” en, *Joule*, vol. 2, no. 10, pp. 2016–2046, Oct. 2018, ISSN: 25424351. DOI: 10.1016/j.joule.2018.08.017. [Online]. Available: <https://linkinghub.elsevier.com/retrieve/pii/S2542435118304021>.
- [107] K. Wang, W. Hua, X. Huang, *et al.*, “Synergy of cations in high entropy oxide lithium ion battery anode,” en, vol. 14, p. 1487, Mar. 2023, ISSN: 2041-1723. DOI: 10.1038/s41467-023-37034-6. [Online]. Available: <https://www.nature.com/articles/s41467-023-37034-6>.

A

Appendix: supporting information

Structure	E_total (eV)	s(E_total) (eV)
ELC	0.301	0.046
EHC	0.293	0.051
OHC	0.314	0.028
OLC	0.304	0.063
O	0.258	0.031

Structure	E_a (eV)	S(E_a) (eV)	E_b (eV)	S(E_b) (eV)	E_c (eV)	S(E_c) (eV)
ELC	0.274	0.061	0.222	0.063	0.319	0.055
EHC	0.326	0.062	0.212	0.065	0.302	0.076
OHC	0.364	0.070	0.310	0.074	0.288	0.086
OLC	0.355	0.100	0.228	0.104	0.311	0.070
O	0.306	0.037	0.228	0.086	0.267	0.080

Structure	E_cross (eV)	S(E_cross) (eV)	E_Li (eV)	S(E_Li) (eV)	E_In (eV)	S(E_In) (eV)
ELC	0.311	0.060	0.273	0.061	0.616	0.320
EHC	0.254	0.057	0.243	0.046	0.465	0.138
OHC	0.299	0.047	0.288	0.043	0.599	0.257
OLC	0.293	0.044	0.254	0.052	0.266	0.178
O	0.423	0.066	0.285	0.061	0.391	0.098

Figure A.1: Summary of the calculated activation energies per structure and axis/layer in the Li_3InCl_6 /disorder analysis.

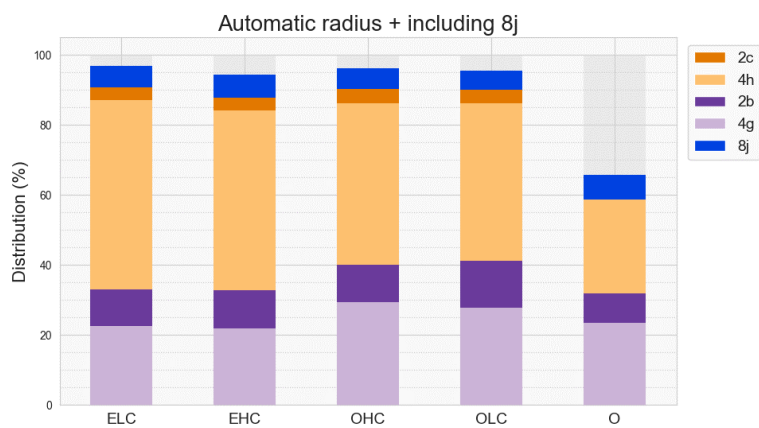


Figure A.2: Captured percentage of lithium density when including site 8j

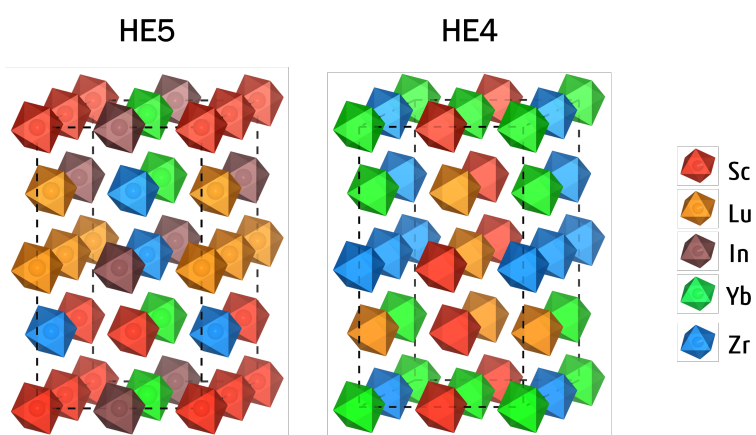


Figure A.3: Lowest energy structures among the five candidates for the study of high entropy effects with HE4 and HE5

(meV per atom)	layered	close together	dispersed	random 1	random 2
LIC	-3203.32				-3203.32
L-SYZL-C	-3849.58	-3858.10	-3851.09	-3850.09	-3859.71
difference with minimum	10.13255682	1.614034091	8.621988636	9.626306818	0
L-IYZLmoreS-C	-3729.71	-3734.41	-3729.07	-3732.53	-3735.85
difference with minimum	4.692429379	1.444293785	6.775084746	3.317175141	0

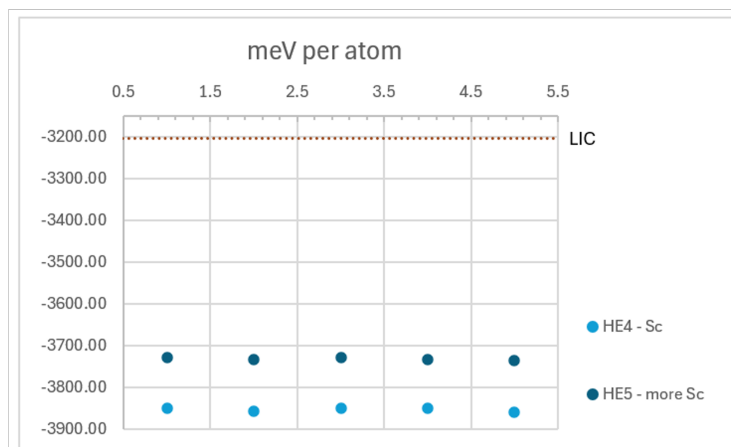


Figure A.4: Relaxation energies of the 5 high entropy structures for HE4 and HE5

Structure	E _{total} (eV)	s(E _{total}) (eV)
LIC	0.334	0.017
HE5	0.325	0.028
LIC - 90 ps	0.314	0.036
HE5 - 90 ps	0.323	0.021
HE4	0.252	0.019

Structure	E _a (eV)	S(E _a) (eV)	E _b (eV)	S(E _b) (eV)	E _c (eV)	S(E _c) (eV)
LIC	0.323	0.033	0.305	0.042	0.351	0.025
HE5	0.329	0.032	0.333	0.044	0.308	0.042
LIC - 90 ps	0.027	0.030	0.280	0.041	0.315	0.041
HE5 - 90 ps	0.344	0.025	0.357	0.033	0.288	0.034
HE4	0.254	0.033	0.276	0.032	0.214	0.025

Structure	E _{cross} (eV)	S(E _{cross}) (eV)	E _{Li} (eV)	S(E _{Li}) (eV)	E _{ln} (eV)	S(E _{ln}) (eV)
LIC	0.318	0.038	0.320	0.038	0.587	0.188
HE5	0.283	0.021	0.308	0.034	0.552	0.182
LIC - 90 ps	0.318	0.038	0.320	0.038	0.587	0.188
HE5 - 90 ps	0.283	0.021	0.308	0.034	0.552	0.182
HE4	0.263	0.022	0.253	0.032	0.384	0.164

Figure A.5: Summary of the calculated activation energies per structure and axis/layer in the high entropy analysis

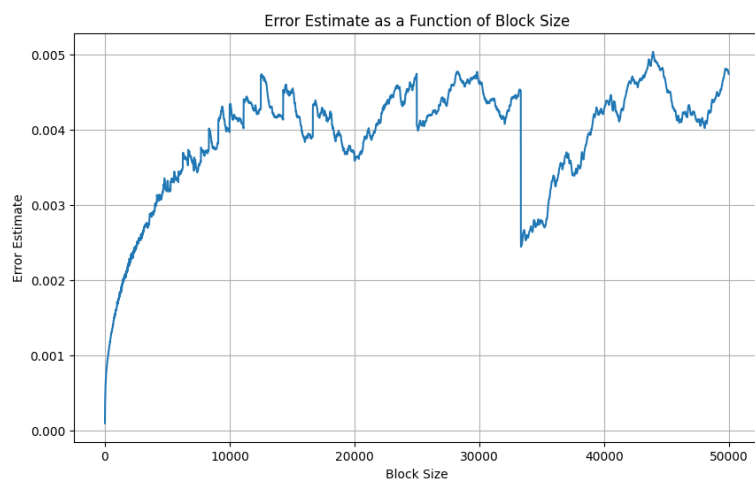


Figure A.6: Saturation of the error in MSD (axis y) as a function of the block length in which to group the coordinates (x)

B

Appendix: Python tools

Required packages

```
1 from gemdat import Trajectory, SimulationMetrics, SitesData
2 from gemdat.io import read_cif, load_known_material, get_list_of_known_materials
3 import typing
4 if typing.TYPE_CHECKING:
5     from gemdat.trajectory import Trajectory
6 from pymatgen.core import Structure
7 from pymatgen.core.structure import Lattice
8 from pymatgen.core.units import FloatWithUnit
9 import numpy as np
10 from scipy.constants import Boltzmann, angstrom, elementary_charge
11 import tqdm
12 from collections import defaultdict
13 from itertools import product
14 from MDAnalysis import Universe
15 from typing import Dict
```

Diffusion per axis

```
1
2 def distances_from_base_per_dimension(trajectory: Trajectory) -> np.ndarray:
3     """
4     Calculate the total distances from base positions for each dimension.
5
6     This function ignores periodic boundary conditions.
7
8     Parameters
9     -----
10    trajectory : Trajectory
11        The trajectory data.
12
13    Returns
14    -----
```

```

15 total_distances : np.ndarray
16     The total distances from base positions for each dimension.
17     """
18     lattice_vectors = np.array(trajectory.get_lattice().abc)
19     all_distances = [diff_vectors for diff_vectors in trajectory.
20                     cumulative_displacements]
21     total_distances = all_distances * lattice_vectors[None, None, :]
22     return total_distances
23
24 def dir_diffusivity(trajectory: Trajectory, *, dimensions: int = 3) -> F:
25     """
26     Calculate the tracer diffusivity.
27
28     The tracer diffusivity is defined as the mean square displacement (MSD) divided by
29     twice the product of the number of diffusion dimensions and the total time.
30
31     Parameters
32     -----
33     trajectory : Trajectory
34         The trajectory data.
35     dimensions : int, optional
36         The number of diffusion dimensions. Default is 3.
37
38     Returns
39     -----
40     dir_tracer_diff : FloatWithUnit
41         The tracer diffusivity in m2/s.
42     """
43     distances_dir = distances_from_base_per_dimension(trajectory)
44     distances_tot = trajectory.distances_from_base_position()
45     msd_dim = np.mean(distances_dir[-1]**2, axis=0) # Angstrom2
46     msd_tot = np.mean(distances_tot[:, -1]**2)
47
48     msd = np.concatenate([[msd_tot], msd_dim])
49     dir_tracer_diff = (msd * angstrom**2) / (2 * dimensions * trajectory.total_time)
50     return dir_tracer_diff

```

Diffusion per layer

```

1
2 def get_indices_jump_type(sites: SitesData, selected_type: str) -> list:
3     """
4     Get the indices of the jumps corresponding to the selected jump type.
5
6     Parameters
7     -----
8     sites : SitesData
9         The sites data.
10    selected_type : str
11        The relevant direction.
12
13    Returns
14    -----
15    jump_combinations : list
16        The combinations of indices for the jump type.
17    """
18    relevant_jumps = direction_dict[selected_type]
19    indices_map = defaultdict(list)

```

```

20
21     for index, label in enumerate(sites.site_labels):
22         indices_map[label].append(index)
23
24     jump_combinations = []
25     for jump in relevant_jumps:
26         start, stop = jump[0], jump[1]
27         if start in indices_map and stop in indices_map:
28             start_indices, stop_indices = indices_map[start], indices_map[stop]
29             jump_combination = list(product(start_indices, stop_indices))
30             jump_combinations.extend(jump_combination)
31
32     return jump_combinations
33
34
35 def select_transitions(transitions_matrix: np.ndarray, selected_indices: list) -> np.
36     ndarray:
37     """
38     Select transitions from the transitions matrix based on the selected indices.
39
40     Parameters
41     -----
42     transitions_matrix : np.ndarray
43         The transitions matrix.
44     selected_indices : list
45         The selected indices.
46
47     Returns
48     -----
49     selected_transitions : np.ndarray
50         The selected transitions.
51     """
52     mask = np.zeros_like(transitions_matrix, dtype=bool)
53     for indices in selected_indices:
54         mask[indices[0], indices[1]] = True
55
56     selected_transitions = transitions_matrix.copy()
57     selected_transitions[~mask] = 0
58     return selected_transitions
59
60 def jump_diffusivity_per_type(sites: SitesData, selected_jump_type: str, dimensions: int
61     ) -> tuple:
62     """
63     Calculate the jump diffusivity per type of jump.
64
65     Parameters
66     -----
67     sites : SitesData
68         The sites data.
69     selected_jump_type : str
70         The selected jump type.
71     dimensions : int
72         The number of diffusion dimensions.
73
74     Returns
75     -----
76     mean_jump_diffusivities : float
77         The mean jump diffusivities.
78     std_jump_diffusivities : float
79         The standard deviation of the jump diffusivities.

```

```

79     """
80     lattice = sites.trajectory.get_lattice()
81     structure = sites.structure
82     total_time = sites.trajectory.total_time
83
84     pdist = lattice.get_all_distances(structure.frac_coords, structure.frac_coords)
85     transitions_parts = sites.transitions.split(n_steps=len(sites.trajectory))
86     selected_indices = get_indices_jump_type(sites, selected_jump_type)
87
88     jump_diffusivities = np.zeros(len(transitions_parts))
89
90     for i, part in enumerate(transitions_parts):
91         transitions_matrix = part.matrix()
92         selected_transitions_matrix = select_transitions(transitions_matrix,
93                 selected_indices)
94
95         jump_diff = np.sum(pdist**2 * selected_transitions_matrix)
96         jump_diff *= angstrom**2 / (2 * dimensions * sites.n_floating * total_time)
97         jump_diff = FloatWithUnit(jump_diff, 'm^2_s^-1')
98
99         jump_diffusivities[i] = jump_diff
100
101     return np.mean(jump_diffusivities), np.std(jump_diffusivities)
102
103 def get_activation_per_jump_type(sites: SitesData, selected_temperatures: Optional[list]
104     = None) -> tuple:
105     """
106     Get the activation per jump_type.
107
108     Parameters
109     -----
110     sites : SitesData
111         The sites data.
112     selected_temperatures : list, optional
113         The selected temperatures. If None, all temperatures are used.
114
115     Returns
116     -----
117     plot_data : list
118         The plot data.
119     E : np.ndarray
120         The activation energy.
121     """
122     diff_per_direction = np.zeros((len(direction_dict), len(sites), 2))
123     jump_types = list(direction_dict.keys())
124
125     if selected_temperatures is None:
126         selected_temperatures = temperatures
127
128     missing_temperatures = np.setdiff1d(np.array(selected_temperatures), np.array(
129         temperatures))
130     if len(missing_temperatures) > 0:
131         warnings.warn(f"The following temperatures are not present: {
132             missing_temperatures}")
133
134     indices = np.where(np.isin(temperatures, selected_temperatures))[0]
135     x = 1000/np.array(temperatures)
136     selected_x = x[indices]
137
138     y = np.zeros((len(direction_dict), len(sites)))

```

```

136 sy = np.zeros((len(direction_dict), len(sites)))
137
138 selected_y = np.zeros((len(direction_dict), len(selected_temperatures)))
139 selected_sy = np.zeros((len(direction_dict), len(selected_temperatures)))
140
141 b = np.zeros((len(direction_dict), 2))
142 yr = np.zeros((len(direction_dict), len(temperatures)))
143
144 for j in range(len(direction_dict)):
145     for i, traj in enumerate(sites.keys()):
146         diff_per_direction[j][i] = jump_diffusivity_per_type(sites[traj],
147             selected_jump_type=jump_types[j], dimensions=3)
148         y[j,i] = np.log(diff_per_direction[j, i, 0])
149         sy[j,i] = 1/diff_per_direction[j, i, 0]*diff_per_direction[j, i, 1]
150
151         selected_y[j] = y[j][indices]
152         selected_sy[j] = sy[j][indices]
153         a, b[j,0], _, b[j,1], _, _ = weighted_fitting(selected_x, selected_y[j],
154             selected_sy[j])
155         yr[j] = a + b[j,0]*x
156
157 E = -b*1000*Boltzmann/elementary_charge
158 E[:,1] = np.abs(E[:,1])
159 plot_data = [x, y, sy, selected_x, selected_y, selected_sy, yr]
160 return plot_data, *E.flatten()

```

LAMMPS xyz trajectory to GEMDAT Trajectory object

```

1 from typing import Dict
2
3 def make_trajectory(coords_file: str, box_file: str, species_dict: Dict[str, int],
4     temperature: float, time_step: int = 2, constant_lattice: bool = True, format: str =
5     'xyz', atom_style: str = 'atomic') -> Trajectory:
6     """
7     Generates a trajectory from given coordinates and box files.
8
9     Parameters:
10    coords_file (str): Path to the coordinates file.
11    box_file (str): Path to the box file.
12    species_dict (Dict[str, int]): Dictionary mapping species names to their counts.
13    temperature (float): Temperature for the simulation.
14    time_step (int, optional): Time step for the simulation. Defaults to 2.
15    constant_lattice (bool, optional): Whether the lattice is constant. Defaults to True
16    .
17    format (str, optional): Format of the coordinates file. Defaults to 'xyz'.
18    atom_style (str, optional): Atom style for the simulation. Defaults to 'atomic'.
19
20    Returns:
21    Trajectory: The generated trajectory.
22    """
23
24    metadata = {'temperature': temperature}
25
26    # Extract species names and numbers
27    species_names = species_dict.keys()
28    species_number = species_dict.values()
29
30    # Create universe from coordinates file
31    u = Universe(coords_file, format=format)

```

```
29
30 # Get lattice from box file
31 l = LAMMPSData.from_file(filename=box_file, atom_style=atom_style).structure.lattice
32
33 # Generate species list
34 a = [name for name, count in zip(species_names, species_number) for _ in range(count
    )]
35
36 structures = [Structure(lattice=l, species=a, coords=ts.positions,
    coords_are_cartesian=True) for ts in u.trajectory]
37
38 traj = Trajectory.from_structures(structures, time_step=time_step, constant_lattice=
    constant_lattice)
39 traj.metadata = metadata
40
41 return traj
```